1-1-2018

Computational Study Of Transition Metal Complexes For Solar Energy Conversion And Molecular Interaction With Strong Laser Fields

Xuetao Shi
Wayne State University,

COMPUTATIONAL STUDY OF TRANSITION METAL COMPLEXES FOR SOLAR ENERGY CONVERSION AND MOLECULAR INTERACTION WITH STRONG LASER FIELDS

by

XUETAO SHI

DISSERTATION

Submitted to the Graduate School

of Wayne State University,

Detroit, Michigan

in partial fulfillment of the requirements

for the degree of

DOCTOR OF PHILOSOPHY

2018

MAJOR: CHEMISTRY (Physical)

Approved By:

____

Advisor Date

____

____

____

DEDICATION

To my parents and my wife, without whose unconditional support, this long journey would have been so much less enjoyable.

ACKNOWLEDGEMENTS

My Ph.D. work has been a life changing experience that was only made possible with the help of quite a few important people along this journey.

First, I would like to thank my advisor, Prof. H. Bernhard Schlegel, who has been an inspirational role model for me to become a scientist myself, and whose exceptional kind-hearted personality has made him a role model for me to become a better person. It is through his guidance over the years I could have come this far and have grown this much.

I would also like to thank my committee members, Prof. Vladimir Chernyak, Prof. Claudio N. Verani, and Prof. Jeffrey Potoff for taking their valuable time to provide suggestions and feedbacks on my studies, dissertation, defense and beyond.

I am very grateful to my collaborators and co-authors for their discussions, advices, and educating me in their respective expertise, including Dr. Richard Lord, Prof. Yuan-Jang Chen in Taiwan, Prof. John F. Endicott, Dr. Debashis Basu, Prof. Claudio N. Verani, Prof. Shivnath Mazumder, and Prof. Wen Li.

Special thanks are due to my best friends here, Dr. Tian Shi, Dr. Bishnu Thapa, Yi-Jung Tu and Sebastien Hebert for their support, suggestions and discussions about research, cultures, and the world at large. It is also my pleasure to have worked with all other members of the Schlegel group, including Dr. Brian Psciuk, Dr. Jason Sonk, Dr. Qing Liao, and Paul Hoerner.

I would also like to thank the Wayne State University Grid computing center for providing the computational power that made the entirety of my computational works possible.

Financial support from Natural Science Foundation, Department of Energy, and Wayne State University is also greatly appreciated.

TABLE OF CONTENTS

DEDICATION ii

ACKNOWLEDGEMENTS iii

LIST OF TABLES vii

LIST OF FIGURES ix

LIST OF SCHEMES xiii

CHAPTER 1 DISSERTATION OVERVIEW AND INTRODUCTION 1

CHAPTER 2 DFT CHARACTERIZATION OF METAL-TO-LIGAND CHARGE-TRANSFER EXCITED STATES OF (RUTHENIUMAMMINE)(MONODENTATE AROMATIC LIGAND) CHROMOPHORES ... 7

2.1 Introduction 7

2.2 Computational Details. 8

2.3 Observed and Calculated Absorption Spectra. 9

2.4 Observed Emission Spectra and Computational Modeling of Triplet States. 14

2.5 Conclusions 18

CHAPTER 3 WATER REDUCTION WITH A COBALT(III) ELECTROCATALYST COORDINATED TO TETRADENTATE AND PENTADENTATE OXIMES AND POLYPYRIDINE-RICH LIGAND 20

3.1 Introduction 20

3.2 Computational methods 20

3.3 Evaluation of the coordination preferences and catalytic pathways of tetradentate heteroaxial cobalt oximes towards hydrogen generation 22

3.4 Distinct Proton and Water Reduction Behavior with a Cobalt(III) Electrocatalyst Based on Pentadentate Oximes 27

3.5 Ligand Transformations and Efficient Proton/Water Reduction with Cobalt Catalysts Based on Pentadentate Pyridine-Rich Environments 30

3.6 Summary 34

CHAPTER 4 CONTROLLING CHEMICAL REACTIONS BY SHORT, INTENSE MID-INFRARED LASER PULSES: COMPARISON OF LINEAR AND CIRCULARLY POLARIZED LIGHT IN SIMULATIONS OF $CLCHO^+$ FRAGMENTATION 36

4.1 Introduction 36

4.2 Method 38

4.3 Results and Discussion 40

4.4 Summary 49

CHAPTER 5 CONTROLLING CHEMICAL REACTIONS BY SHORT, INTENSE MID-INFRARED LASER PULSES: TWO INDEPENDENTLY OSCILLATING LINEARLY POLARIZED PULSES IN SIMULATIONS OF $CLCHO^+$ FRAGMENTATION 50

5.1 Introduction 50

5.2 Method 50

5.3 Branching ratio and energy absorption comparison 52

5.4 Continuous wavelet transformation analysis 53

5.5 Summary 57

CHAPTER 6 COMPUTATIONAL SIMULATIONS OF A "MOLECULAR PROPELLER": HYDROGEN CIRCULAR MIGRATION IN PROTONATED ACETYLENE INDUCED BY CIRCULARLY POLARIZED LIGHT 58

6.1 Introduction 58

6.2 Method 61

6.3 Results and Discussion 62

6.4 Summary 70

6.5 Appendix 71

CHAPTER 7 UNPHYSICAL CHARGE OSCILLATION PROBLEM WITH BORN-OPPENHEIMER MOLECULAR DYNAMICS IN HIGH INTENSITY LASER FIELD AND A VIABLE WORKAROUND BY USING ATOM-CENTERED DENSITY MATRIX PROPAGATION METHOD 74

7.1 Introduction 74

7.2 Method 74

7.3 Charge oscillation problem 75

7.4 Comparison of ADMP with BOMD 76

7.5 Conclusion 79

CHAPTER 8 INTERPRETATION OF TWO-ELECTRON ANGULAR STREAKING EXPERIMENTS FOR METHANE MOLECULE BY TIME-DEPENDENT CONFIGURATION INTERACTION AND BORN-OPPENHEIMER MOLECULAR DYNAMICS SIMULATIONS 80

8.1 Introduction 80

8.2 Method 80

8.3 First and second ionization of methane molecule 83

8.4 Structural relaxation classification 87

8.5 Summary 89

REFERENCES 90

ABSTRACT 100

AUTOBIOGRAPHICAL STATEMENT 104

LIST OF TABLES

Table 2.1. Summary of the Observed and Calculated Lowest-Energy MLCT Absorption Maxima for Some Mono- and Diruthenium Complexes 9

Table 2.2. Comparison of the Calculated Excited-State Transition Energies for Singlet and Triplet MLCT Excited States Evaluated in the Nuclear Coordinates of the Ground State (S_0) and Lowest-Energy MLCT Excited State (T_0) 13

Table 2.3. Comparison of the orbital occupations of T_0 and the nearest in energy ^{3}MC excited states of trans- $[Ru(NH_3)_4(pz)_2]^{2+}$. 15

Table 3.1. Energetics of pyridine substitution by DFT calculations 23

Table 3.2. Co–ligand bond lengths[a] of 1 from X-ray crystal and DFT-optimized structures. Metal–ligand bond distances[a] of the one-electron reduced (Co^{II}) analog of 1 are also reported 24

Table 4.1. Branching ratios for the dissociation of $ClCHO^+$ interacting with circular and linear polarized laser pulses. 42

Table 4.2. Average total energy absorbed by $ClCHO^+$ interacting with circular and linear polarized laser pulses. 43

Table 5.1. Vibrational modes calculated at the B3LYP/6-311G(d,p) level for ClCHO+ and all possible fragments resulted from the dissociation channels considered. 52

Table 5.2. Branching ratio and total energy absorption as the result of different laser fields . 53

Table 6.1. Total energy and total angular momentum absorbed as a function of wavelength for circularly polarized light.[a] 64

Table 6.2. Total energy and total angular momentum absorbed for 7µm linear and circularly polarized light.[a] 65

Table 6.3. Atomic kinetic energy decomposition (kcal/mol). 67

Table 6.4. Average cumulative angular displacement in the xy plane after 800 fs (in degrees) 68

Table A1. Density functional benchmark on the energy difference between classical and non-classical $C_2H_3^+$ structures 72

Table 7.1. Energy gain for ADMP trajectories with different fictitious electron masses compared with a BOMD example set that did not have charge oscillation problem. 77

Table 7.2. energy gain for trajectories of ADMP method with different fictitious electron masses compared with a BOMD example set that had charge oscillation problem. 78

LIST OF FIGURES

Figure 2.1. Qualitative potential energy curves for a $[(L)_4Ru(A)_2]^{m+}$ complex based on a single Ru^{II} and a single acceptor (A) orbital, which lead to a MLCT excited state with singlet or triplet spin multiplicity....7

Figure 2.2. Comparison of the observed (black curves) and calculated (B3PW91; red curves) absorption envelopes for *trans,trans*-$[\{Ru(NH_3)_4(py)\}_2(pz)]^{4+}$, left panel, and *cis*-$[Ru(NH_3)_4(phpy)_2]^{2+}$, right panel....10

Figure 2.4. Comparison of the ambient and low-temperature absorption spectra of a trans-$[Ru(NH_3)_4(pz)_2]^{2+}$ complex in an ethanol/methanol solvent 11

Figure 2.3. Correlation of the calculated (B3PW91) and observed MLCT absorption maxima of several complexes with Ru-A chromophores. 11

Figure 2.6. Comparison of observed (black) and calculated (red; B3PW91) absorption spectra (upper panel) with computing oscillator strength (lower panel in logarithmic scale) of *mer*-$[Ru(NH_3)_3(bpy)(pz)]^{2+}$. 12

Figure 2.5. Natural transition orbitals (NTOs) for *trans*-$[Ru(NH_3)_4(py)(pz)]^{2+}$ (8), $[Ru(NH_3)_4(bpy)]^{2+}$ (b), and *mer*- $[Ru(NH_3)_3(bpy)(pz)]^{2+}$ (11); and *trans,trans*-$[\{Ru(NH_3)_4(py)\}_2(pz)]^{4+}$ (13); NTOs the lowest energy (state 1) and the lowest energy MLCT excited state with a large oscillator strength. 12

Figure 2.7. Comparison of the spin densities of several Ru-MDA complexes in their T_0 excited states. 15

Figure 2.8. Comparison of the spin densities of *trans*-$[Ru(NH_3)_4(py)(pz)]^{3+}$ and *trans,trans*-$[\{Ru(NH_3)_4(py)\}_2pz]^{5+}$ in their one-electron-oxidized states. 15

Figure 2.9. NTOs for the singlet and triplet excited states (TD-DFT calcualtions) with ground-state nuclear coordinates of *trans*-$[Ru(NH_3)_4(py)(pz)]^{2+}$. 16

Figure 2.10. NTOs for lowest-energy ^{1}MLCT excited states and for the T_0 excited state of 13. The lowest-energy ^{1}MLCT excited state with significant oscillator strength is S_5. 16

Figure 2.11. Qualitative representation of the contrast in the lowest energy excited states of the Ru-MDA and Ru-bpy chromophores. 17

Figure 3.1. The mononuclear complexes $[Co^{III}(prdioxH)(^{4tBu}py)(Cl)]PF_6$ (1), $[Co^{III}(prdioxH)(^{4Pyr}py)(Cl)]PF_6$ (2), and $[Co^{III}(prdioxH)(^{4Bz}py)(Cl)]PF_6$ (3). 22

Figure 3.2. DFT-optimized geometries of $[Co^{III}(prdioxH)(^{4tBu}py)(Cl)]^+$, $[Co^{II}(prdioxH)(^{4tBu}py)(Cl)]$, and $[Co^{II}(prdioxH)(^{4tBu}py)]^+$. The metal center is displaced by 0.15 Å off of the plane of the macrocyclic oxime ligand in $[Co^{II}(prdioxH)(^{4tBu}py)]^+$. 24

Figure 3.3. The catalytic pathways calculated for H_2 evolution by 1 in the presence of HTFA in CH_3CN (ACN). The formation of a Co^{III}–H species is invoked. 26

Figure 3.4. Synthetic scheme of the Co^{III} complex (1). 27

Figure 3.5. Calculated structures of species electrochemically generated in MeCN: a) Co^{III}/Co^{II} reduction, b) Co^{II}/Co^{I} reduction, and c) loss of chloride from the Co^{II} species in the presence of H^+. 28

Figure 3.6. Catalytic mechanism of H_2 generation by 1 in MeCN. Free energy changes in kcal mol^{-1}. 29

Figure 3.7. Possible pathways for the decomposition of the catalyst in water. Free-energy changes in kcal mol^{-1}. 30

Figure 3.9. Catalytic mechanism of H_2 generation by 4 in MeCN. It involves a Co^{II}–H species that undergoes protonation to generate H_2. 32

Figure 3.8. Reaction energy profile for the hydroxy to amide conversion in MeCN. The transition state * is not explicitly located. 32

Figure 4.1. Angular dependence of (a) the total yield for the ionization of ClCHO as a function of the polarization direction and (b) the contributions of the HOMO (yellow), HOMO-1 (blue) and HOMO-2 (green) to the total ionization yield. 41

Figure 4.2. Energy deposited as a function of the in-plane angle ϕ of the direction of linearly polarized light with a field strength of 0.06 au for (a) Cl + CHO^+, (b) H + $ClCO^+$, and (c) HCl^+ + CO; (d) branching ratio as a function of the in-plane angle ϕ of the direction of linearly polarized light with a field strength of 0.06 au. 45

Figure 4.3. Magnitude and direction of the total angular momentum for the Cl + HCO^+, H + $ClCO^+$ and HCl^+ + CO channels with 0.06 field strength for left circularly polarized light (top row, green), right circularly polarized light (top row, red) and linearly polarized light averaged over ϕ = 0 - 360°(bottom row, blue). 46

Figure 4.4. Total angular momentum of the products as a function of the in-plane angle ϕ of the direction of linearly polarized light with a field strength of 0.06 au for (a) Cl + CHO^+, (b) H + $ClCO^+$, and (c) HCl^+ + CO; (d) polar angle θ for the total angular momentum as a function of the in-plane angle ϕ of the direction of linearly polarized light with a field strength of 0.06 au....47

Figure 4.5. Mulliken charges as a function of time during the pulse for (a) left circularly polarized light, (b) right circularly polarized light, (c) linearly polarized light with ϕ = 90 (aligned with the CH bond), and (d) linearly polarized light with ϕ = 0 (aligned perpendicular to the CH bond) .48

Figure 5.1. CWT analysis scalograms with proposed peak identifications. Darker color indicates stronger signal. Vertical axis is in logarithm scale. Red vertical lines indicate average dissociation time. 56

Figure 6.1. Potential energy curve for protonated acetylene computed at the M062X, MP2, MP4, CCSD(T) and BD(T) levels of theory with the 6-311+G(3df,2pd) basis set. 63

Figure 6.2. Histogram of combined (H1+H2+H3) atomic angular momentum for left and right circularly and linearly (0 - 360° averaged) polarized at the end of simulation (top row) and over simulation time (bottom row). 66

Figure 6.3. Average combined hydrogen atomic angular momentum z component and cumulative average angular displacements as a function of time for non-dissociating trajectories......69

Figure A1. Average combined hydrogen atomic angular momentum z component and cumulative average angular displacement over time for the trajectories in Table 6.4. 71

Figure A2. Average out of plane angle for the hydrogens and standard deviations over time.71

Figure 7.2. Histogram plots of energy gain for trajectories of BOMD and ADMP with different fictitious electron masses. 78

Figure 7.3. Example trajectory comparison of Mulliken charge on H atom for BOMD with ADMP. This is the same trajectory used in Figure 7.1. All the ADMP trajectories investigated behave like the example shown here. 79

Figure 8.1. Stable/meta-stable model structures and their corresponding relative energy levels for methane cation. 81

Figure 8.2. HOMO splitting scheme for methane molecule with electric field along H–C–H angle bisector (top) and along C–H bond (bottom). The orbital levels of field-free case are on the left, and the orbital levels of static field case are on the right. 84

Figure 8.3. HOMO splitting scheme for methane cation with electric field along H–C–H angle bisector (top) and along C–H bond (bottom). 84

Figure 8.4. Ionization dependence of neutral methane molecule. 85

Figure 8.5. Ionization dependence of methane cation with neutral species geometry. 85

Figure 8.6. Ionization dependence of methane cation with C_{2v}, C_{3v} and D_{2d} geometries. 86

Figure 8.7. Histogram plot of structural classifications along an ideal trajectory without zero-point energy and thus entirely deterministic. 87

Figure 8.8. Histogram plot of structural classifications along an ideal trajectory without zero-point energy and thus entirely deterministic. 88

LIST OF SCHEMES

Scheme 3.2. Synthesis of Co^{III} complexes 2, 3, and 4. 31

Scheme 3.3. Generalized H_2 generation mechanism. 34

Scheme 4.1. Coordinate system for the simulation of circularly polarized light propagating along the z axis interacting with $ClCHO^+$ 38

Scheme 6.1. Geometries and a representation of potential energy surface for the interchange between the T-shaped and Y-shaped structures of protonated acetylene resulting in a propeller-like motion of the hydrogens around the C_2 core. 59

Scheme 6.2. Lowest energy dissociation channels for $C_2H_3^+$ 63

CHAPTER 1 DISSERTATION OVERVIEW AND INTRODUCTION

After more than half a century of electronic structure theory development, we now have the modern computational tools to study a wide array of molecular types from small molecules to large nanoscale clusters and biochemical systems. Although high level of quantum chemistry methods such as Coupled Cluster methods (CCSD) give very reliable and accurate calculations of chemical and physical properties of a given molecule, they can still only deal with very small scale molecules with up to a few tens of atoms. Density Functional Theory (DFT) methods on the other hand, specifically the hybrid functionals and long-range corrected functionals, strike a mostly acceptable balance between accuracy and computational cost. This is especially true when studying molecular systems with one or more transition metal atoms since other methods are either too cost-prohibitive or inaccurate. Due to the importance of transition metal complexes in photo-catalysis reactions, DFT methods play a very important role in catalyst design for chemical processes that are involved in renewable energy efforts such as water splitting.

While electronic structure calculations give a full description (when the potential energy surface is explored completely) of a single molecule, the bulk behavior of a large collection of molecules cannot be obtained directly from such calculations. Although the bulk properties can be easily computed using statistical mechanics if the system is at or near equilibrium, many of the interesting phenomena happen far away from the equilibrium. This kind of dynamics requires a more direct approach to study—molecular simulation. Born-Oppenheimer Molecular Dynamics (BOMD) is one of many computational tools that are often used to conduct molecular simulations. Although BOMD and its similar alternatives have been used for decades to study chemical processes under conventional conditions, recent enhancements enable us to use BOMD to study molecular systems interacting with strong electric field such as that of intense mid-infrared laser light. This particular type of laser has the ability to deposit directly energy into molecular vibrational modes and therefore has the potential of achieving the long-elusive chemical selectivity.

In this dissertation the research is presented in the following seven chapters:

Chapter 2 describes the metal-to-ligand charge-transfer (MLCT) excited states of several complexes with (ruthenium) (monodentate aromatic ligand, MDA) chromophores synthesized and studied experimentally in the Endicott and Chen groups, and investigated computationally by using time-dependent density function theory (TD-DFT). The calculated MLCT states correlate closely with the heretofore unknown emission properties that were observed experimentally. The TD-DFT modeling of singlet and triplet MLCT excited states helps to explain the experimental observation that the emission maxima occur in the visible and near-IR spectral regions and have much more poorly resolved vibronic sidebands than related complexes with Ru-bpy chromophores, and that the excited-state lifetimes are comparable to Ru-bpy MLCT excited states in this energy range.

Chapter 3 focuses on the computational modeling of the thermodynamical and electrochemical properties of three new series of cobalt based water splitting catalysts that were synthesized and studied experimentally in the Verani group. The calculations provide a reasonable interpretation of experimental observations and yield a plausible reaction mechanism for proton reduction by these cobalt based catalysts. The first series is a family of cobalt complexes with pentadentate pyridine-rich ligands (the experimental work as well as the associated computational work has been published[1]). The mechanisms of catalysis involve the protonation of a Co^{II}-H species generated in situ. The second series is a family of three heteroaxial cobalt oxime catalysts, namely $[Co^{III}(prdioxH)(^{4tBu}py)(Cl)]PF_6$, $[Co^{III}(prdioxH)(^{4Pyr}py)(Cl)]PF_6$, and $[Co^{III}(prdioxH)(^{4Bz}py)(Cl)]PF_6$ (the experimental work as well as the associated computational work has been published[2]). The reduction of these Co^{III} complexes yields low spin Co^{II} and low spin Co^{I} species in which the pyridine acts as the dominant axial ligand. In the presence of protons, the catalytically active Co^{I} species generates a Co^{III}–H hydride species that reacts heterolytically with another proton to generate dihydrogen (the experimental work as well as the associated computational work has been published[3]). The third series is a pentadentate oxime that has ligand incorporated water upon metal coordination and is water soluble. This Co^{III} species is doubly reduced to Co^{I} and exhibits proton reduction activity in the presence of weak acids in MeCN dihydrogen (the experimental work as well as the associated computational work has been published[3]).

Chapter 4 describes the effect of circularly polarized intense mid-IR laser pulses to enhanced mode selective fragmentation of ClCHO+. The ionization rate of ClCHO in the molecular plane has been calculated by time-dependent configuration interaction with a complex absorbing potential (TDCI-CAP), and is nearly twice as large as perpendicular to the plane, suggesting a degree of planar alignment can be obtained experimentally for $ClCHO^+$, starting from neutral molecules. Classical trajectory calculations with Born-Oppenheimer molecular dynamics (BOMD) in a 4 cycle 7 µm laser pulse show that circularly polarized light with the electric field in the plane of the molecule deposits more energy and yields larger branching ratios for higher energy fragmentation channels than linearly polarized light with the same maximum field strength. These results suggest circularly polarized mid-IR pulses can not only achieve control of reactions but also provide an experimentally accessible implementation.

Chapter 5 describes a BOMD study of the fragmentation of ClCHO+ using two independently varying laser pulses simultaneously. The aim is to study the possibility of independently promoting different molecular vibrational modes by laser pulses that differ in pulse direction, wavelength, and duration. The resulting trajectories give very different branching ratios with different pairs of the dual laser pulses. The difference in branching ratios is even more pronounced when one of the two pulses started one quarter of the total duration earlier than the other vs. the other way around for the same exact pulse pair. Due to the complexity of the effects resulting from the superposition of two laser pulses, and the need to interpret the statistical significance of hundreds of trajectories, more advanced analysis techniques are needed to decipher the extent to which each of the various molecular vibrational modes are promoted. Continuous Wavelet Transformation (CWT) is found to be more suitable for this task than more commonly used Windowed Fourier Transformation (WFT) since more normal modes in reactant and dissociation products are in the mid-frequency range (ca. 500-1500 cm^{-1}) than in the high-frequency range (ca. 1500-3500 cm^{-1}). CWT has the distinct advantage of having better frequency resolution (at the expense of time-resolution) at lower-frequency region unlike WFT which has fixed time-frequency resolution in all regions. CWT analysis gives rise to some very interesting results for pre- and post-dissociation events for each dissociation channel.

Chapter 6 is also related to the study of circularly polarized intense mid-IR laser pulse in comparison with linearly polarized pulse by using BOMD trajectory calculations but with a different system, protonated acetylene. The hydrogens in this molecule are very mobile and can easily migrate around the C2 core by moving between the Y shaped classical structure and the bridged, T-shaped non-classical structure of the cation, which is 4 kcal/mol lower in energy. Trajectory calculations were carried out with the M062X/6-311+G(3df,2pd) level of theory. The functional was chosen based on a benchmark study of the energy difference between the classical and non-classical structures for more than 200 functionals. The linearly and circularly polarized pulses transfer similar amounts of energy and total angular momentum to $C_2H_3^+$. The average angular momentum vectors of the three hydrogens show opposite directions of rotation for right and left circularly polarized light, but no directional preference for linearly polarized light. This difference results in an appreciable amount of angular displacement of the three hydrogens relative to the C2 core for circularly polarized light, but only an insignificant amount for linearly polarized light. Over the course of the simulation with circularly polarized light, this corresponds to a propeller-like motion of the three hydrogens around the C2 core of protonated acetylene.

Chapter 7 attempts to tackle a problem inherent in Born-Oppenheimer Molecular Dynamics (BOMD), which has been used to study various chemical processes with intense mid-IR laser pulses in previous chapters. From past studies [4-7], as well as these chapters, it is shown that BOMD gives relatively accurate descriptions of the problems of interest. In the Born-Oppenheimer approximation, the wavefunction of the system is converged at each time step to calculate the force for integrating the classical equations of motion. However, this resulted in an artifact manifested for a few trajectories as anomalously large charge oscillations on an H atom ($H^+/H^\bullet/H^-$) when it was well-separated (beyond ca. 3 Å) from the rest of the molecule, thus absorbing similarly anomalously large amount of energy. An alternative to BOMD is the Atom-centered Density Matrix Propagation (ADMP) method, developed by H. B. Schlegel et al., where instead of using converged electronic structure to propagate the wavefunction, atom-centered density matrix coefficients are given a fictitious mass and propagated based on extended Lagrangian dynamics. It has been demonstrated that ADMP is as accurate as BOMD for field-free systems. In this chapter, our calculation comparisons with BOMD in intense laser field show that the similar accuracy can also be achieved, although to a lesser extent. And since wavefunction is not converged at each time step for ADMP, the charge oscillation problem naturally disappears.

Chapter 8 details an attempt to interpret the experimental results of two-electron angular streaking for methane molecule by TDCI calculations and BOMD trajectory calculations with the additional help from a logistic regression machine learning algorithm used to analyze geometric changes. The focus in the experiment is the relative ejection angle between the two electrons that were sequentially ionized from neutral methane molecule. Since a circularly polarized laser pulse was used in the experiment, this angle is correlated with the time delay between these two ionization events. Therefore, the peaks in two-electron ejection angle signals can be traced back to unique events in the dynamics of methane molecule after the first ionization. The ionization angular dependence of various stable and meta-stable structures of methane cation, as well as neutral methane, is calculated by our TDCI-CAP approach with necessary symmetry manipulation to avoid the problems caused by the triple degeneracy of methane cation. The relaxation time needed for neutral methane geometry (tetrahedron shape) to collapse into the various stable and meta-stable structures on cation potential energy surface is then probed by BOMD calculations, and the geometries along trajectories are classified into those stable/meta-stable geometries. A machine learning algorithm is used instead of point group symmetry classification because of the chaotic nature of trajectories relaxing from a very high energy starting geometry.

CHAPTER 2 DFT CHARACTERIZATION OF METAL-TO-LIGAND CHARGE-TRANSFER EXCITED STATES OF (RUTHENIUMAMMINE)(MONODENTATE AROMATIC LIGAND) CHROMOPHORES

Adapted with permission from *Inorg. Chem.*, **2013**, 52 (17), pp 9774–9790.

2.1 Introduction

Although the metal-to-ligand charge-transfer (MLCT) excited states of a very large number of ruthenium(II) complexes containing polydentate aromatic (bpy, tpy, etc.) ligands have well-characterized MLCT emission spectra,[8-12] the related emission properties of MLCT excited states of complexes with monodentate aromatic (MDA) ligands have not been previously

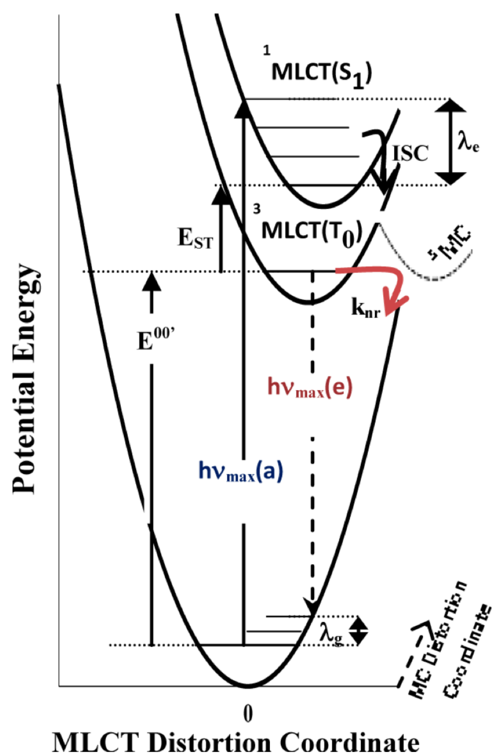

Figure 2.1. Qualitative potential energy curves for a $[(L)_4Ru(A)_2]^{m+}$ complex based on a single Ru^{II} and a single acceptor (A) orbital, which lead to a MLCT excited state with singlet or triplet spin multiplicity. A possible ^{3}MC is illustrated by the dashed curve. Note that the distortion coordinates for the ^{3}MC excited state are different from those for the MLCT excited states. The key parameters for discussing the excited-state properties are illustrated in the figure.

reported. The difficulty in detecting the emission from MLCT excited states of complexes with MDA ligands was hypothesized (at the time of conducting the research in this chapter) to be a result of their unusually short lifetimes or unusual energies. Although a much more recent study by the same experimental group supports an alternative hypothesis, the exploration in line with the aforementioned hypothesis was nonetheless very helpful. There are many molecular properties that can affect the excited state energies and lifetimes of these complexes, some of which have been well documented in the literature and others that have not.[13-21] The excited-state properties of complexes of the simple monobipyridine $[(L)_4Ru(bpy)]^{m+}$ complexes (L is a nominally "innocent" ligand) have been relatively well characterized,[22-28] and these complexes can provide a rough basis for evaluating the MLCT excited-state properties of the related $[(L)_4Ru(MDA)_2]^{m+}$ complexes. Figure 2.1 illustrates the simplest limit for which there is a single MLCT electronic configuration (and a possible MC excited state) but two MLCT states with different spin multiplicities.

2.2 Computational Details.

Electronic structure calculations were carried out using density functional theory (DFT),[29] as implemented in a development version of Gaussian.[30] In a previous report of related Ru-bpy complexes,[27] M. M. Allard et al. found that the B3PW91 functional[31-34]in combination with the SDDall basis set[34-37]correlated well with the experimental absorption spectra. In this chapter, we choose the SDD basis set, which employs the more flexible D95 V basis set for main group atoms for a better description of the molecular geometries.[38] We have used both the B3PW91[31-34] and LC-ωPBE[39-41] functionals to model the electronic structures of the complexes but find that the B3PW91 functional gives better agreement with the observed properties of the complexes.[27]

Wave functions were tested for self-consistent-field (SCF) stability,[42,43] and all optimized structures were confirmed as minima by analyzing the harmonic vibrational frequencies.[44] Solvation effects (in acetonitrile) were accounted for using the most recent implementation of the implicit IEF-PCM solvation model.[45-48] Vertical electronic excitation energies and intensities were evaluated using time-dependent DFT (TDDFT), [49-51] the orbital transitions of each excited state were characterized using the natural transition orbital (NTO) method,[30,52] and the isodensity plots of the orbitals involved in these transitions were visualized using GaussView.[53] The triplet MLCT excited states of *trans*-$[Ru(NH_3)_4(py)(pz)]^{2+}$ and *trans,trans*-$[\{Ru(NH_3)_4(py)\}_2(pz)]^{4+}$ were obtained using SCF calculations rather than TD-DFT. The calculation of the oxidation and reduction potentials of the complexes has been described previously[54] and used the B3PW91/SDD level of theory with zero-point-energy or thermal corrections; the present work did not include zero-point energies and thermal corrections. The calculated potentials were referenced to a calculated value of $E_{1/2}$ = 4.321 V for the AgCl/Ag couple under our level of theory.[55-57]

2.3 Observed and Calculated Absorption Spectra.

Table 2.1. Summary of the Observed and Calculated Lowest-Energy MLCT Absorption Maxima for Some Mono- and Diruthenium Complexes

		MLCT absorption maxima, $\times 10^3$ cm^{-1} [a]		
		obsd	calcd[c]	
compd no.	complex	$h\nu_{max}$ ($h\nu_{lo}$) [$h\nu_{hi}$] [b]	lowest-energy dominant[d]	S_0/S_1[e]
1	$[Ru(NH_3)_5(py)]^{2+}$	24.42 (21.2) [24.3]	25.7	20.8
2	$[Ru(NH_3)_5(ac\text{-}py)]^{2+}$	19.8 (15.6) [19.8]	21.3	15
3	$[Ru(NH_3)_5(pz)]^{2+}$	21.81 (18) [21.8]	25.3	17.6
4c	*cis*-$[Ru(NH_3)_4(py)_2]^{2+}$	24.38 (21.8) [24.1]	24.4	22.4
4t	*trans*-$[Ru(NH_3)_4(py)_2]^{2+}$	23.65 (21.6) [23.6]	22.9	21.1
5c	*cis*-$[Ru(NH_3)_4(ph\text{-}py)_2]^{2+h}$	22.15 (17.2) [21.9]	21.6	20.3
5t	*trans*-$[Ru(NH_3)_4(ph\text{-}py)_2]^{2+}$	21.38 (20.0) [21.4]	20.3	19.4
6c	*cis*-$[Ru(NH_3)_4(ac\text{-}py)_2]^{2+h}$	19.86 (16.5) [19.8]	19.3	17.2
6t	*trans*-$[Ru(NH_3)_4(ac\text{-}py)_2]^{2+}$	19.32 (15.6) [19.18]	17.9	15.8
7c	*cis*-$[Ru(NH_3)_4(pz)_2]^{2+}$	21.98 (18.34) [22.1]	23.1	20.2
7t	*trans*-$[Ru(NH_3)_4(pz)_2]^{2+}$	21.34 (16.7) [21.4]	21.4	17.6
8	*trans*-$[Ru(NH_3)_4(py)(pz)]^{2+}$	21.76 (17.7) [21.8]	22.6	17.9
9	*mer*-$[Ru(NH_3)_3(bpyam)(pz)]^{2+}$	21.8 (17) [21.8]	23.6	18.3
10	*mer*-$[Ru(NH_3)_3(bpy)(py)]^{2+}$	19.84 (16.3) [19.7]	20.8	16.4
11	*mer*-$[Ru(NH_3)_3(bpy)(pz)]^{2+}$	20.17 (16.6) [20.1]	21.5	17.6

12	$[\{Ru(NH_3)_5\}_2(pz)]^{4+}$	18.32 (16.1) [18.3]	21.2	16.2
13	*trans,trans*-$[\{Ru(NH_3)_4(py)\}_2(pz)]^{4+}$	17.71 (15.2) [17.4]	18.4	16.1
14	$[\{Ru(NH_3)_3(bpyam)\}_2(pz)]^{4+}$	17.3 (14.5) [17.1]	18.4	16.4
a	$[Ru(CH_3CN)_4(bpy)]^{2+}$	25.7	24.2	23.3
b	$[Ru(NH_3)_4(bpy)]^{2+}$ [e]	19	20.3	15.2
c	$[Ru(acac)_2(bpy)]$	16.1	18.2	12.9

[a]In acetonitrile. [b]$h\nu_{max}$ = lowest-energy observed MLCT band maximum; the $h\nu_{lo}$ and $h\nu_{hi}$ energy maxima are based on Gaussian deconvolutions of the absorption envelopes.45 [c]Vertical electronic energies and intensities based on the B3PW91 functional. [d]Energies based on the maxima of envelopes constructed by assigning a Gaussian of 2000−3000 cm^{-1} full-width at half-height to each calculated transition. [e]The lowest-energy calculated transition energy.

Calculations based on the B3PW91 functional[31-34] for mono and diruthenium complexes indicate that the ^{1}MLCT excited states whose transitions have the largest oscillator strengths appear to be 900−6300 and 2000−5000 cm^{-1}, respectively, higher than their lowest-energy charge-transfer excited states; see Table 2.1 and Figure 2.5 and 2.6. The lowest energy spectra based on the B3PW91 functional are generally in good agreement with the observed spectra; see Figures 2.5 and 2.6. The calculations employing the LC-ωPBE functional resulted in S_1 being a MC state for several complexes that exhibit strong MLCT-like emissions (see Figure 2.5 and 2.6). This is possibly an artifact of the LC-ωPBE functional.

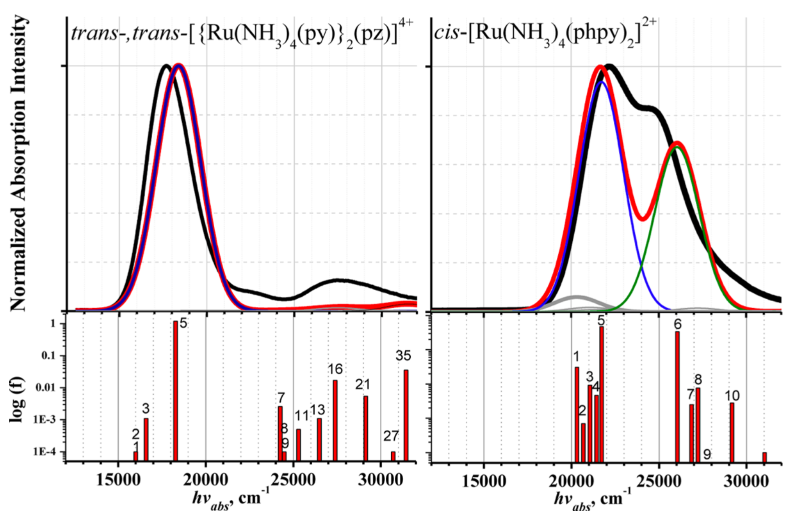

Figure 2.2. Comparison of the observed (black curves) and calculated (B3PW91; red curves) absorption envelopes for *trans,trans*-$[\{Ru(NH_3)_4(py)\}_2(pz)]^{4+}$, left panel, and *cis*-$[Ru(NH_3)_4(phpy)_2]^{2+}$, right panel. The calculated transitions and their calculated oscillator strengths (*f*) are numbered in order of increasing transition energy in the lower panels.

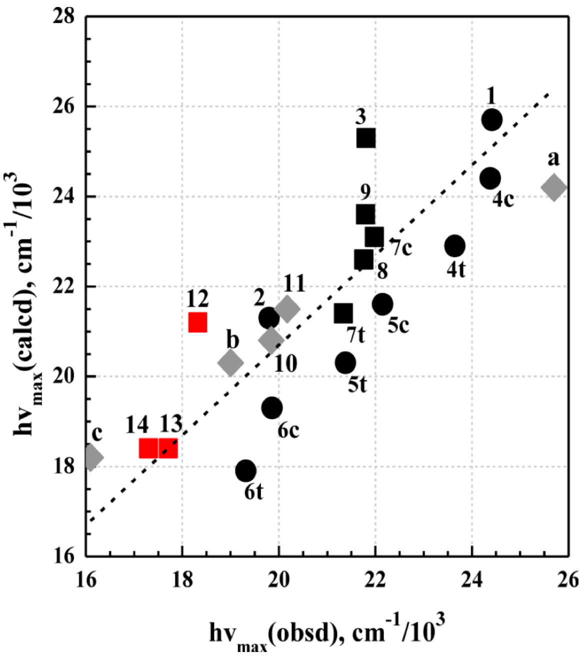

Figure 2.3. Correlation of the calculated (B3PW91) and observed MLCT absorption maxima of several complexes with Ru-A chromophores. The specific complexes related to the numbers and letters are identified in Table 2.1; squares for A = pz, black for monoruthenium complexes, and red for diruthenium complexes; circles for A = Y-py; diamonds for A = bpy. The dashed line is drawn with a slope of 1.00 and an intercept of 690 cm^{-1}.

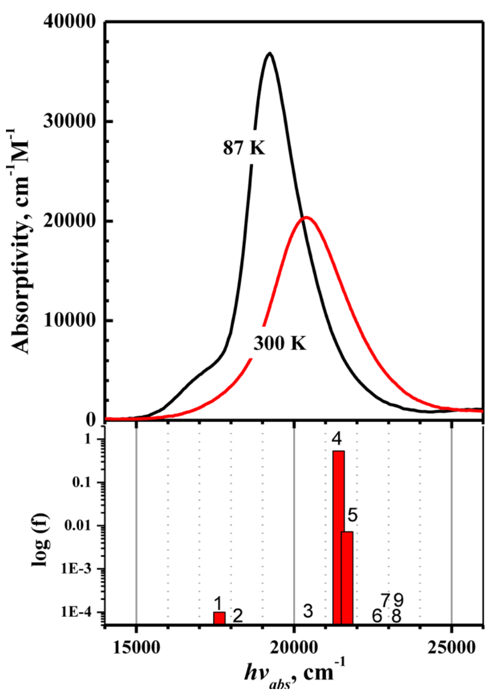

Figure 2.4. Comparison of the ambient and low-temperature absorption spectra of a trans-[Ru(NH$_3$)$_4$(pz)$_2$]$^{2+}$ complex in an ethanol/methanol solvent: solution at 300 K, red; glass at 87 K, black. The calculated transitions (numbered in the order of increasing energy) in the ground-state coordinates are shown in the bottom panel.

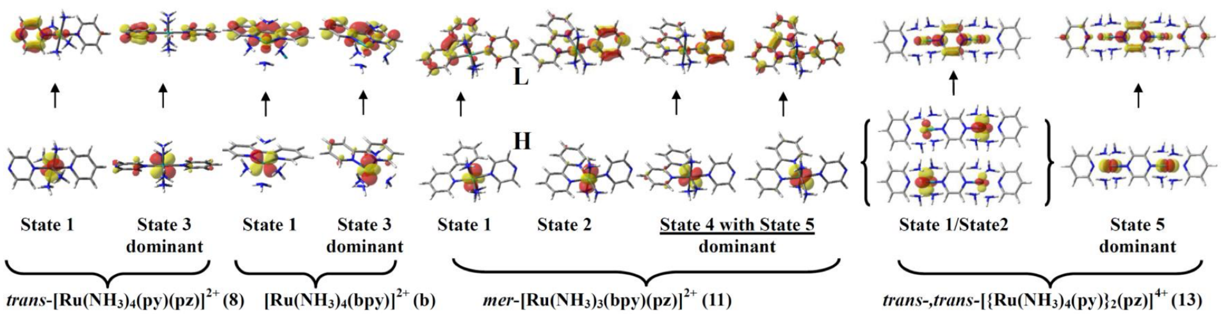

Figure 2.5. Natural transition orbitals (NTOs) for *trans*-$[Ru(NH_3)_4(py)(pz)]^{2+}$ (8), $[Ru(NH_3)_4(bpy)]^{2+}$ (b), and *mer*-$[Ru(NH_3)_3(bpy)(pz)]^{2+}$ (11); and *trans,trans*-$[\{Ru(NH_3)_4(py)\}_2(pz)]^{4+}$ (13); NTOs the lowest energy (state 1) and the lowest energy MLCT excited state with a large oscillator strength.

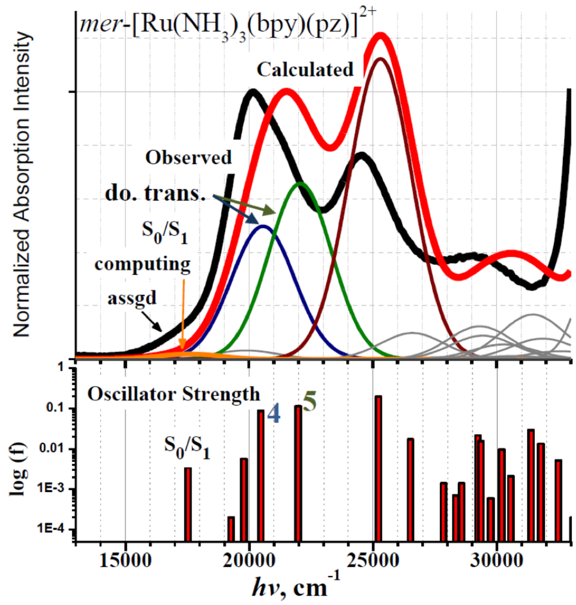

Figure 2.6. Comparison of observed (black) and calculated (red; B3PW91) absorption spectra (upper panel) with computing oscillator strength (lower panel in logarithmic scale) of *mer*- $[Ru(NH_3)_3(bpy)(pz)]^{2+}$. The calculated spectrum is a convolution of all the alculated component transitions (lighter lines) and S_0/S_1 designates the computing and assigned (assgd) Ru/bpy (S_0/S_1) transitions, respectively. The dominated transitions (do. trans.), 4th (navy curve) and 5th (green curve) transitions, are the computing dominated components in the low-energy absorption- envelope. The computed absorption envelopes were simulated using Gaussian bandshapes for the transition components with 3000 cm^{-1} band width (fwhh).

The calculated NTOs[52,58] for the lowest-energy and dominant ^{1}MLCT excited states have different d-orbital compositions for these complexes, as illustrated in Figure 2.5. Our calculations for the *mer*-$[Ru(NH_3)_3(bpy)(pz)]^{2+}$ complex indicate that its two lowest energy ^{1}MLCT excited states, S_1 with the Ru-bpy chromophore and S_2 with the Ru-pz chromophore, are similar in energy, with the former lower by less than 2000 cm^{-1}; see Figure 2.6.

Table 2.2. Comparison of the Calculated Excited-State Transition Energies for Singlet and Triplet MLCT Excited States Evaluated in the Nuclear Coordinates of the Ground State (S_0) and Lowest-Energy MLCT Excited State (T_0)

	approximate SOMO occupation of the excited state[a]	excited-state transition energies in the coordinates of the S_0 minimum, eV		excited-state transition energies in the coordinates of the T_0 minimum, eV			$h\nu_{max}$(obsd) ($h\nu_{max}$(emis)), eV
		singlet	triplet	S_0 (SCF)[b]	singlet	triplet	
$[Ru(NH_3)_5pz]^{2+}$ (3)	$d_{xy}\rightarrow pz$	2.18 (S_1)	2.02 (T_1)	0.51	1.64 (S_1)	1.41 (T_1)	
	$d_{xz}\rightarrow pz$	2.23 (S_2)	2.04 (T_2)		1.67 (S_2)	1.42 (T_2)	
	$d_{yz}\rightarrow pz$	3.13 (S_3) (dominant)	1.62 (T_0)		2.31 (S_3) (dominant)	0.84 (T_0)	
$[Ru(NH_3)_5py]^{2+}$ (1)	$d_{xy}\rightarrow py$	2.58 (S_1)	2.48 (T_1)	0.72	1.82 (S_2)	1.58 (T_2)	
	$d_{xz}\rightarrow py$	2.61(S_2)	2.49 (T_2)		1.81 (S_1)	1.56 (T_1)	
	$d_{yz}\rightarrow py$	3.19 (S_3) (dominant)	2.08 (T_0)		2.03 (S_3) (dominant)	1.05 (T_0)	
trans-$[Ru(NH_3)_4(py)(pz)]^{2+}$ (8)	$d_{xy}\rightarrow pz$	2.22 (S_1)	2.12 (T_1)	0.47	1.72 (S_1)	1.53 (T_1)	
	$d_{xz}\rightarrow pz$	2.30 (S_2)	2.19 (T_2)		1.80 (S_2)	1.59 (T_2)	
	$d_{yz}\rightarrow pz$	2.80 (S_3) (dominant)	1.80 (T_0)		2.22 (S_3) (dominant)	1.05 (T_0)	1.60 (1.52)
trans-$[Ru(NH_3)_4(pz)_2]^{2+}$ (7t)	$d_{xy}\rightarrow pz$	2.19 (S_1)	2.18 (T_2)	0.53	1.77 (S_1)	1.61 (T_1)	
		2.55 (S_3)					
	$d_{xz}\rightarrow pz$	2.28 (S_2)	2.27 (T_3)		1.87 (S_2)	1.69 (T_2)	
	$d_{yz}\rightarrow pz$	2.66 (S_4) (dominant)	2.00 (T_0) 2.12 (T_1)		2.17 (S_3) (dominant)	1.24 (T_0)	1.67 (1.77)
trans-$[Ru(NH_3)_4(py)_2]^{2+}$ (4t)	$d_{xy}\rightarrow py$	2.61 (S_1)	2.61(T_2)	0.74	1.94 (S_1)	1.72 (T_1)	
	$d_{xz}\rightarrow py$	2.67 (S_2)	2.66 (T_3)		1.98 (S_2)	1.76 (T_2)	
	$d_{yz}\rightarrow py$	2.84(S_3) (dominant)	2.27 (T_0)		2.02 (S_3) (dominant)	1.28 (T_0)	
trans-trans-$[\{Ru(NH_3)_4(py)\}_2(pz)]^{4+}$ (13)	d_{xy}-$d_{xy}\rightarrow pz$	2.00 (S_1)	1.88 (T_1)	0.12	1.87 (S_1)	1.73 (T_1)	
	d_{xy}+$d_{xy}\rightarrow pz$	2.00 (S_2)	1.88 (T_2)		1.87 (S_2)	1.73 (T_2)	
	d_{xz}-$d_{xz}\rightarrow pz$	2.07 (S_3)	1.94 (T_4)		1.96 (S_3)	1.79 (T_4)	
	d_{xz}+$d_{xz}\rightarrow pz$	2.12 (S_4)	1.98 (T_5)		1.99 (S_4)	1.83 (T_5)	
	d_{yz}-$d_{yz}\rightarrow pz$	2.28 (S_5) (dominant)	1.28 (T_0)		2.23 (S_5)	0.98 (T_0)	1.47 (1.10)
	d_{yz}+$d_{yz}\rightarrow pz$	3.00 (S_6)	1.90 (T_3)		3.03 (S_6)	1.76 (T_3)	

[a]Cartesian coordinates defined with respect to the plane of the MDA ring. [b]See Figure 2.1.

Our computational modeling of the complexes and Ru-MDA chromophores has found that most of the lowest-energy transitions within the singlet manifold, involving the highest occupied molecular orbital (HOMO) and lowest unoccupied molecular orbital (LUMO), have very small oscillator strengths. This is very similar to previous observations on the complexes with Ru-bpy chromophores.[27] In most of the Ru-MDA complexes, these transitions appear as a low-energy tail of the dominant absorption band, and the interpretation of this is equivocal. At lower temperatures, the component bandwidths are appreciably decreased so low temperature spectra should result in a better resolution of these weak transitions.

To summarize, the calculated absorption spectra for Ru-MDA complexes are generally in good agreement with the observed spectra. And these calculations helped to highlight the following difference and similarity between Ru-MDA and Ru-bpy complexes:

A. The calculated NTOs for the lowest-energy and dominant ^{1}MLCT excited states have different d-orbital compositions for Ru-MDA and Ru-bpy complexes.

B. For Ru-MDA complexes, most of the lowest-energy transitions involving HOMO and LUMO within the singlet manifold, have very small oscillator strengths, similar to previous observations on the Ru-bpy complexes.

2.4 Observed Emission Spectra and Computational Modeling of Triplet States.

We have modeled the triplet as well as singlet excited-state manifolds of several of the complexes, and the overall modeling results are summarized in Table 2.2.

We have also calculated the lowest-energy ^{3}MC excited-state energies for *trans*-$[Ru(NH_3)_4(pz)_2]^{2+}$, and the details for the former are summarized in Table 2.3. In Table 2.3, the singly occupied orbitals are expressed in terms of corresponding orbital plots; the corresponding orbital is very similar to the NTO and is a transformation such that the triplet spin contributions are almost entirely from α-HOMO and α-HOMO− 1 orbitals. Because this corresponds to a MC transition, the d orbitals are no longer aligned in the Cartesian coordinates of the two pz rings.

Table 2.3. Comparison of the orbital occupations of T_0 and the nearest in energy ^{3}MC excited states of trans-$[Ru(NH_3)_4(pz)_2]^{2+}$.

	^{3}MLCT			^{3}MC-d_{xy}			^{3}MC-d_{yz}		
Energy (kcal/mol)	0			3.53			0.26		
Spin Density	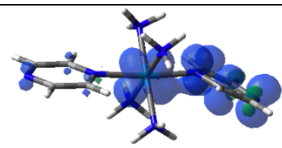 Ru: 1.04			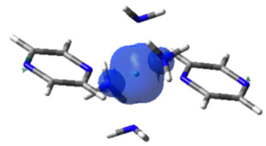 1.95			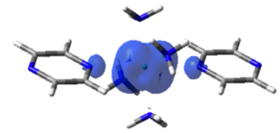 1.95		
Corresponding orbitals	α-HOMO 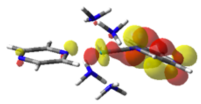 α-HOMO-1 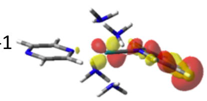			α-HOMO 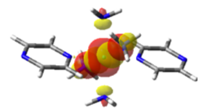 α-HOMO-1 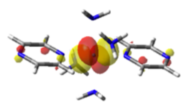			α-HOMO 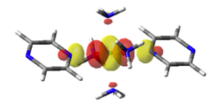 α-HOMO-1 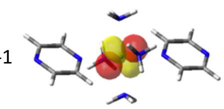		
Geometry(Å)	Ru-N (pz)	Ru-N′ (pz)	Ru-N (NH_3)	Ru-N (pz)	Ru-N′ (pz)	Ru-N (NH_3)	Ru-N (pz)	Ru-N′ (pz)	Ru-N (NH_3)
	2.154	2.047	2.139 2.147	2.080	2.080	2.557 2.188	2.640	2.640	2.160

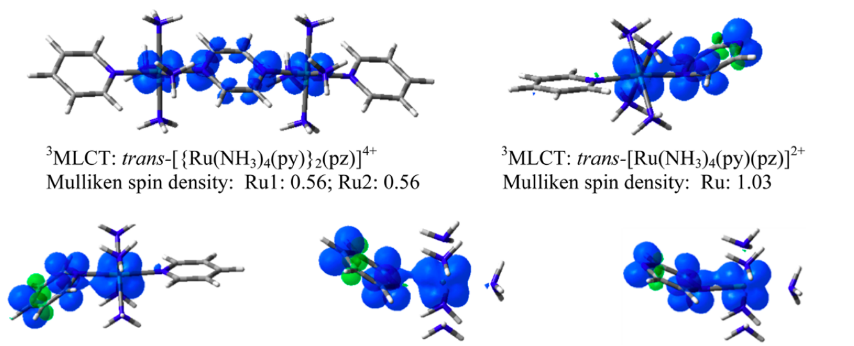

^{3}MLCT: *trans*-$[\{Ru(NH_3)_4(py)\}_2(pz)]^{4+}$
Mulliken spin density: Ru1: 0.56; Ru2: 0.56

^{3}MLCT: *trans*-$[Ru(NH_3)_4(py)(pz)]^{2+}$
Mulliken spin density: Ru: 1.03

^{3}MLCT: *trans*-$[Ru(NH_3)_4(py)_2]^{2+}$
Mulliken spin density: Ru: 1.12

^{3}MLCT: $[Ru(NH_3)_5py]^{2+}$
Mulliken spin density: Ru: 1.14

^{3}MLCT: $[Ru(NH_3)_5pz]^{2+}$
Mulliken spin density: Ru: 1.06

Figure 2.7. Comparison of the spin densities of several Ru-MDA complexes in their T_0 excited states.

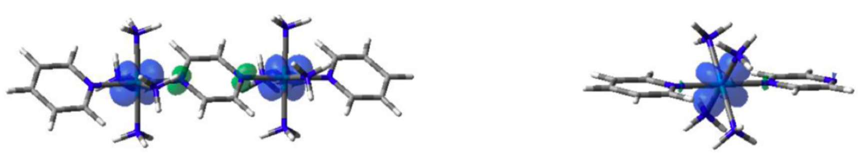

Oxidized: *trans*-$[\{Ru(NH_3)_4(py)\}_2(pz)]^{5+}$ (doublet)
Mulliken spin density: Ru1: 0.65; Ru2: 0.65

Oxidized: *trans*-$[Ru(NH_3)_4(py)(pz)]^{3+}$ (doublet)
Mulliken spin density: Ru: 1.09

Figure 2.8. Comparison of the spin densities of *trans*-$[Ru(NH_3)_4(py)(pz)]^{3+}$ and *trans,trans*-$[\{Ru(NH_3)_4(py)\}_2pz]^{5+}$ in their one-electron-oxidized states.

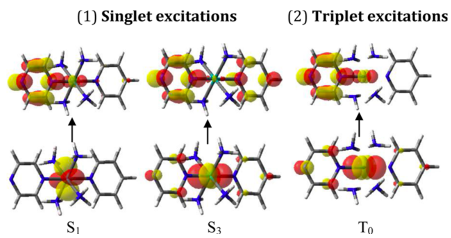

Figure 2.9. NTOs for the singlet and triplet excited states (TD-DFT calcualtions) with ground-state nuclear coordinates of *trans*-$[Ru(NH_3)_4(py)(pz)]^{2+}$.

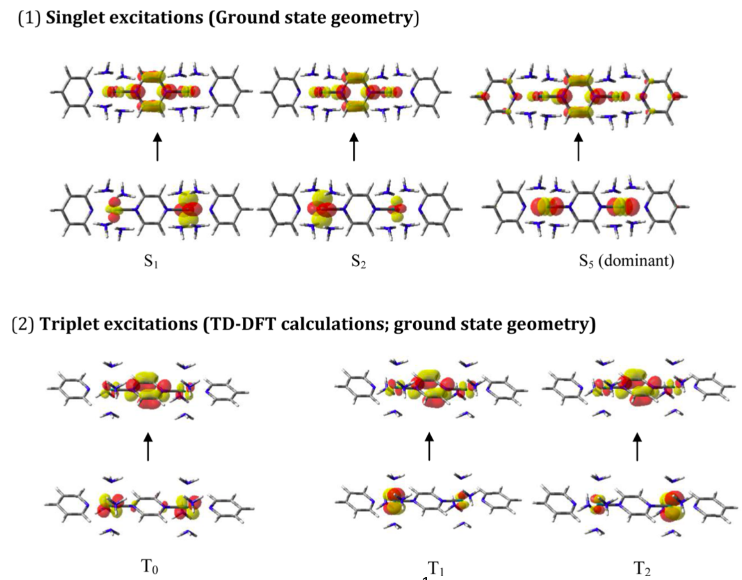

Figure 2.10. NTOs for lowest-energy ^{1}MLCT excited states and for the T_0 excited state of **13**. The lowest-energy ^{1}MLCT excited state with significant oscillator strength is S_5. Note that while S_1 and S_2 have very similar energies and correspond to a localized (Ru^{III}/Ru^{II}) Franck−Condon excited-state structure, the two Ru centers of T_0 have similar electronic populations.

The DFT calculations indicate that the two metals in the lowest-energy ^{3}MLCT excited state of *trans,trans*-$[\{Ru(NH_3)_4(py)\}_2(pz)]^{4+}$ have the same amount of charge (see Figure 2.7). Figure 2.7 also compares the calculated Mulliken spin densities of *trans*-$[Ru(NH_3)_4(py)(pz)]^{2+}$, *trans*-$[Ru(NH_3)_4(py)_2]^{2+}$, $[Ru(NH_3)_5(pz)]^{2+}$, and $[Ru(NH_3)_5(py)]^{2+}$ in their T_0 states. An unexpected feature of the modeled T_0 states of the monometallic complexes is that the reduced MDA rings are displaced from their ground-state planes by 30− 40° in the acetonitrile solvent but not in the gas phase; the potential energy barrier for interconversion of the two equivalent out-of-plane MDA-ring displacements is small (260 cm^{-1} calculated for MDA = pz).

We have also calculated the ground-state electronic structures for two of the one-electron-oxidized complexes, and the calculated Mulliken spin densities of *trans*-$[Ru(NH_3)_4(py)(pz)]^{3+}$ and *trans,trans*-$[\{Ru(NH_3)_4(py)\}_2pz]^{5+}$ are shown in Figure 2.8. These calculations show that the d-orbital populations of the Ru centers are the same in the respective T_0 states and Ru^{III} complexes.

The NTOs calculated for the lowest-energy MLCT transitions, of the *trans,trans*-$[\{Ru(NH_3)_3(py)\}_2(pz)]^{4+}$ and *trans*-$[Ru(NH_3)_4(py)(pz)]^{2+}$ complexes are characteristic of the Ru-pz chromophore (see Figures 2.9 and 2.10), and the 77 K emission does not have the vibronic sideband structure typical of the bpy-ligand distortions consistent with the Ru-pz chromophore. These observations indicate that the lowest energy ^{3}MLCT excited-state energies do not differ much for the different chromophores, but everything else being equal, the excited-state energies decrease in the order Ru-bpy < Ru-pz <Ru-py.

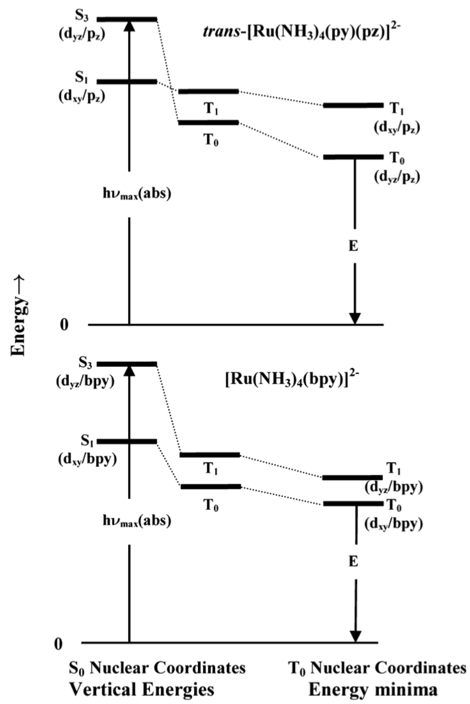

Figure 2.11. Qualitative representation of the contrast in the lowest energy excited states of the Ru-MDA and Ru-bpy chromophores. The energies of states designated in the two columns on the left were calculated using nuclear coordinates of the ground state energy minimum; those in the column on the right are for the difference in energy of the S_0 minimum and T_0 or T_1 minima.

2.5 Conclusions

DFT calculations indicate that the electronic states involved in the absorption and emission maxima of Ru-MDA chromophores have similar electronic configurations. This is in distinct contrast to the observations on complexes with Ru-bpy chromophores for which the dominant absorption and T_0 correspond to different electronic configurations.[59,60] This contrast is illustrated in Figure 2.11.

This study has found some important points about the contrasts in behavior of the Ru-MDA and Ru-bpy excited states:

1. As shown in Figure 2.11, the contrasting electronic configurations found for T_0 in the two classes of complexes appear to correlate with the variations in the singlet and triplet excited-state energy differences, E_{ST}, for the d_{yz}/acceptor and d_{xy}/acceptor electronic configurations. For the example shown in the figure, E_{ST} is larger for the states with d_{yz}/acceptor configurations than that of the d_{xy}/acceptor configurations. Between *trans*-$[Ru(NH_3)_4(py)(pz)]^{2+}$ and $Ru(NH_3)_4(bpy)]^{2+}$, E_{ST} of d_{yz}/acceptor is similar; however, E_{ST} of d_{xy}/acceptor is very different, i.e., smaller for the former than the latter. Therefore, it is mostly the smaller value of E_{ST} for the d_{xy}/pz configuration of *trans*-$[Ru(NH_3)_4(py)(pz)]^{2+}$ that results in its T_0 having the d_{yz}/acceptor configuration, while T_0 for $[Ru(NH_3)_4(bpy)]^{2+}$ has the d_{xy}/acceptor configuration. This is almost certainly a consequence of the differences in donor/acceptor orbital spatial overlap in these complexes in which the MDA acceptor ligands can only interact with one out of the two axes of the donor d orbital while the bpy acceptor ligands can interact with both of the two axes of the donor d orbital (note that the exchange integral contribution to EST is expected to increase with spatial overlap).[10]

2. The metal coordination spheres of the Ru-MDA complex excited states are highly distorted, with especially large distortions involving the Ru-MDA moiety. Even at the T_0 energy minimum, the Ru− MDA bond is appreciably lengthened [0.1 Å for Ru−N(pz) compared to 0.006 Å for Ru− N(bpy) in $[Ru(NH_3)_4bpy]^{2+}$ and the MDA ring is displaced from the position along the Ru− N bonding axis.

CHAPTER 3 WATER REDUCTION WITH A COBALT(III) ELECTROCATALYST COORDINATED TO TETRADENTATE AND PENTADENTATE OXIMES AND POLYPYRIDINE-RICH LIGAND

3.1 Introduction

Generation of H_2 from H^+ or H_2O has driven extensive research as a replacement for nonrenewable fossil fuels.[61,62] The use of H^+ involves a $2e^-$ transfer to generate a Co^I species which yields 1 equiv of H_2. Among well-known examples of H^+ reduction catalysts, Co^{III} glyoxime-based oximes[63-66] have been investigated in great detail, in which the catalytic $^{LS}3d^8$ Co^I state seems to favor a five-coordinate environment required for nucleophilic attack on the proton, [65,67,68]generating a Co^{III}–H hydride species that reacts heterolytically with another proton to generate dihydrogen. Recent results also point to the importance of pyridine-containing ligands in proton reduction, for which complexes of imino-, di-, tetra-, and pentapyridine ligands have been investigated. [69-80]

3.2 Computational methods

Calculations were performed with a development version of the Gaussian suite of programs,[30] using the B3PW91[31-34] functional with the double-zeta SDD basis set on cobalt and the D95 [36,81] basis on the other atoms. All optimized structures were confirmed as minima by analyzing the harmonic vibrational frequencies. Solvation effects in CH_3CN were estimated using the IEF polarizable continuum model (PCM)[45-48] and were included during structure optimization. Single-point energies were reevaluated with the triple-zeta TZVP basis[82] on the metal atom and the 6-311++G(d,p) basis[32] on the other atoms in presence of the continuum solvation model. The free energies were calculated using the triple-zeta SCF energy while the zero-point energy and thermal corrections were included from the double-zeta calculations. The standard states of 1 M concentration were considered for all the reactants and products for calculating the free energies of reactions. Low-spin configurations yielded lower energies for all the species. The wavefunctions of the optimized structures were tested for SCF stability.[42,83,84] Isosurface plots of orbitals and spin densities were visualized using GaussView.[53] The calculation of the reduction potentials of the complexes included zero-point energy and thermal corrections and standard thermodynamic equation $\Delta G = -nFE$ was used. The calculated potentials were referenced to a value of $E_{1/2}$ = 4.678 V for the ferrocene/ferrocenium couple calculated with the present level of theory.

3.3 Evaluation of the coordination preferences and catalytic pathways of tetradentate heteroaxial cobalt oximes towards hydrogen generation

D. Basu and et al. have reported on three new heteroaxial cobalt oxime catalysts, namely

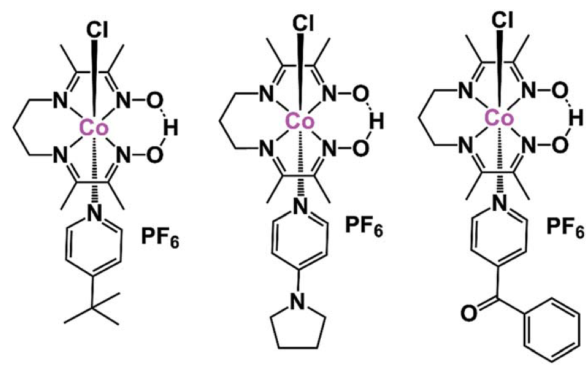

Figure 3.1. The mononuclear complexes $[Co^{III}(prdioxH)(^{4tBu}py)(Cl)]PF_6$ (**1**), $[Co^{III}(prdioxH)(^{4Pyr}py)(Cl)]PF_6$ (**2**), and $[Co^{III}(prdioxH)(^{4Bz}py)(Cl)]PF_6$ (**3**).

$[Co^{III}(prdioxH)(^{4tBu}py)(Cl)]PF_6$ (**1**), $[Co^{III}(prdioxH)(^{4Pyr}py)(Cl)]PF_6$ (**2**), and $[Co^{III}(prdioxH)(^{4Bz}py)(Cl)]PF_6$ (**3**).

The $1e^-$ and $2e^-$ reduced analogs of **1**–**3** generated in the electrochemical pathway towards catalysis determine the viability of proton reduction. Therefore, a detailed evaluation of their coordination preferences, spin states, and electronic structures is of the utmost importance in the understanding of catalytic pathways.

A. The coordination environment of the Co^{III} species

Although crystal structures combined with ^{1}H-NMR spectroscopy provided the strongest evidence to confirm the coordination environment for Co^{III} in the parent state being the expected hexacoordination for this $3d^6$ ion with the oxime as the planar ligand, and chloride and 4-substituted pyridines as axial ligands in the solid state, there was considerable mismatch between the cathodic potential for **1** at 0.49 $V_{Fc/Fc+}$ and the cathodic Co^{III}/Co^{II} potential of the bis-pyridine species at 0.37 $V_{Fc/Fc+}$, possibly due to the capability of the uncoordinated chloride ion to displace the pyridine coordinated to the Co ion in **1**.

The energetics of pyridine substitution are shown in Table 3.1 for **1**–**3** and the proposed mechanism involves an unsaturated five-coordinate intermediate. This event requires ca. 14 kcal mol^{-1}, is energetically unfavorable and the limiting step for **1** and **3**. Chloride addition to the five-coordinate intermediate is favored by 23 kcal mol^{-1} and drives the overall (A + B) substitution process forward by 9–10 kcal mol^{-1}.

Table 3.1. Energetics of pyridine substitution by DFT calculations

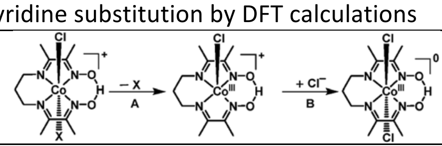

X	A[a]	B[a]	(A+B)[a]
^{4tBu}py	13.5	-23.2	-9.7
^{4Pyr}py	20.0	-23.2	-3.7
^{4Bz}py	14.1	-23.2	-9.1

[a] Values in kcal mol^{-1}.

On the other hand, complex **2** with an electron-donating pyrrolidine ligand has the most energy-demanding first step (20 kcal mol^{-1}) and shows little preference for pyridine substitution with a total energy of the substitution process at 3.2 kcal mol^{-1}.

B. The coordination environment of the Co^{II} species

DFT calculations suggest that formation of a $[Co^{II}(prdioxH)(CH_3CN)_2]^+$ from $[Co^{II}(prdioxH)(CH_3CN)]^+$ is unfavorable by about 9 kcal mol^{-1} in good agreement with results reported by Artero et al.[66] Therefore, we propose that once the chloride is lost, a five-coordinate species $[Co^{II}(prdioxH)(^{4tBu}py)]^+$ is formed as an intermediate. Loss of chloride following the

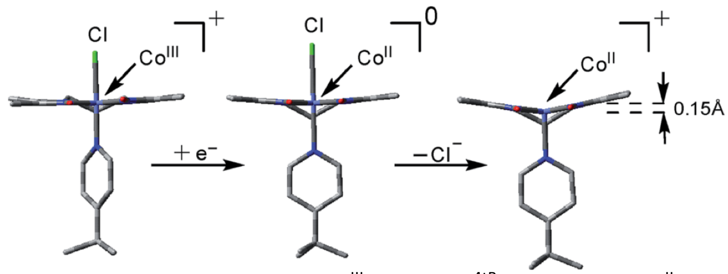

Figure 3.2. DFT-optimized geometries of $[Co^{III}(prdioxH)(^{4tBu}py)(Cl)]^+$, $[Co^{II}(prdioxH)(^{4tBu}py)(Cl)]$, and $[Co^{II}(prdioxH)(^{4tBu}py)]^+$. The metal center is displaced by 0.15 Å off of the plane of the macrocyclic oxime ligand in $[Co^{II}(prdioxH)(^{4tBu}py)]^+$.

reduction of **1** leads to minor conformational changes, where the Co^{II} ion is displaced by 0.15 Å out of the plane of the macrocyclic ligand and towards the remaining ^{4tBu}pyridine (Figure 3.2).

A comparison of X-ray crystal and DFT-calculated metal–ligand bond distances for **1** is shown in Table 3.2 along with the DFT bond distances for the 1e$^-$ reduced analog of **1**.

Table 3.2. Co–ligand bond lengths[a] of **1** from X-ray crystal and DFT-optimized structures. Metal–ligand bond distances[a] of the one-electron reduced (Co^{II}) analog of **1** are also reported

		Co–N_1	Co–N_2	Co–N_3	Co–N_4	Co–N_5	Co–Cl
Experiment	$[Co^{III}(prdioxH)(^{4tBu}py)(Cl)]^+$	1.903	1.917	1.914	1.898	1.975	2.237
Theory	$[Co^{III}(prdioxH)(^{4tBu}py)(Cl)]^+$	1.907	1.925	1.928	1.905	1.988	2.304
Theory	$[Co^{II}(prdioxH)(^{4tBu}py)(Cl)]$	1.904	1.927	1.928	1.904	2.288	2.745

[a] Values are in Å.

C. The coordination environment of the Co^{I} species

Step 1. $[Co^{III}(prdioxH)(^{4tBu}py)(Cl)]^{+} + e^{-} \rightarrow [Co^{II}(prdioxH)(^{4tBu}py)(Cl)]^{o} \rightarrow [Co^{II}(prdioxH)(^{4tBu}py)]^{+} + Cl^{-}$
Step 2. $[Co^{II}(prdioxH)(^{4tBu}py)]^{+} + CH_3CN \rightarrow [Co^{II}(prdioxH)(^{4tBu}py)(CH_3CN)]^{+}$
Step 3. $[Co^{III}(prdioxH)(^{4tBu}py)(Cl)]^{+} + Cl^{-} \rightarrow [Co^{III}(prdioxH)(Cl)_2]^{o} + {}^{4tBu}py$
Step 4. $[Co^{III}(prdioxH)(Cl)_2]^{o} + e^{-} \rightarrow [Co^{II}(prdioxH)(Cl)_2]^{-} \rightarrow [Co^{II}(prdioxH)(Cl)]^{o} + Cl^{-}$
Step 5. $[Co^{II}(prdioxH)(Cl)]^{o} + CH_3CN \rightarrow [Co^{II}(prdioxH)(CH_3CN)(Cl)]^{o}$
Step 6. $[Co^{II}(prdioxH)(CH_3CN)(Cl)]^{o} + {}^{4tBu}py \rightarrow [Co^{II}(prdioxH)(^{4tBu}py)(CH_3CN)]^{+} + Cl^{-}$
Step 7. $[Co^{II}(prdioxH)(^{4tBu}py)(CH_3CN)]^{+} + e^{-} \rightarrow [Co^{I}(prdioxH)(^{4tBu}py)]^{o} + CH_3CN$

Scheme 3.1. Proposed chemical and electrochemical pathway from 1 the catalytically active CoI species.

In light of the comprehensive UV-visible, EPR, NMR, and DFT data accumulated in this chapter, we propose a viable chemical and electrochemical pathway starting from the parent **1** and reducing to the Co^{II} counterpart and to the catalytically active monovalent species (Scheme 3.1). The first Co^{III}/Co^{II} reduction shown in step 1 is followed by loss of a chloride to yield the five-coordinate Co^{II} species $[Co^{II}(prdioxH)(^{4tBu}py)]^{+}$. The latter species incorporates a CH_3CN molecule to form the six-coordinate Co^{II} complex $[Co^{II}(prdioxH)(^{4tBu}py)(CH_3CN)]^{+}$ described in step 2. The released chloride in step 1 replaces the ^{4tBu}pyridine in the remaining $[Co^{III}(prdioxH)(^{4tBu}py)(Cl)]^{+}$ (**1**) as observed generating a second six-coordinate Co^{III} species with two chlorides occupying the axial positions, step 3, along with uncoordinated ^{4tBu}pyridine. This is a chemical, rather than electrochemical step. The second Co^{III}/Co^{II} reduction, shown in step 4, yields the six-coordinate $[Co^{II}(prdioxH)(Cl)_2]$ that is subsequently converted into the five-coordinate $[Co^{II}(prdioxH)Cl]$. Uptake of a solvent CH_3CN molecule by the latter species (step 5) may take place and is followed by replacement of the remaining chloride with one ^{4tBu}pyridine present in solution to give rise to the species $[Co^{II}(prdioxH)(^{4tBu}py)(CH_3CN)]^{+}$ in step 6. This species is then reduced and transforms into the five-coordinate and catalytically active $[Co^{I}(prdioxH)(^{4tBu}py)]$ with release of the CH_3CN molecule in step 7. It is important to mention that Marzilli7 proposed generation of a Co^{II}–Cl species already in step 1. It was further proposed that an outer sphere electron transfer mechanism involving the newly generated Co^{II}–Cl species and the parent Co^{III} complex, and chloride transfer from one metal center to another could yield a Co^{III} dichloro species. The chloride transfer event is calculated to be favorable by 6.7 kcal mol^{-1}. The present chapter offers an alternative pathway where the Co^{III} dichloro species is generated via substitution of ^{4tBu}py already on the parent Co^{III} complex by an external chloride, this process being favorable by 9.7 kcal mol^{-1}.

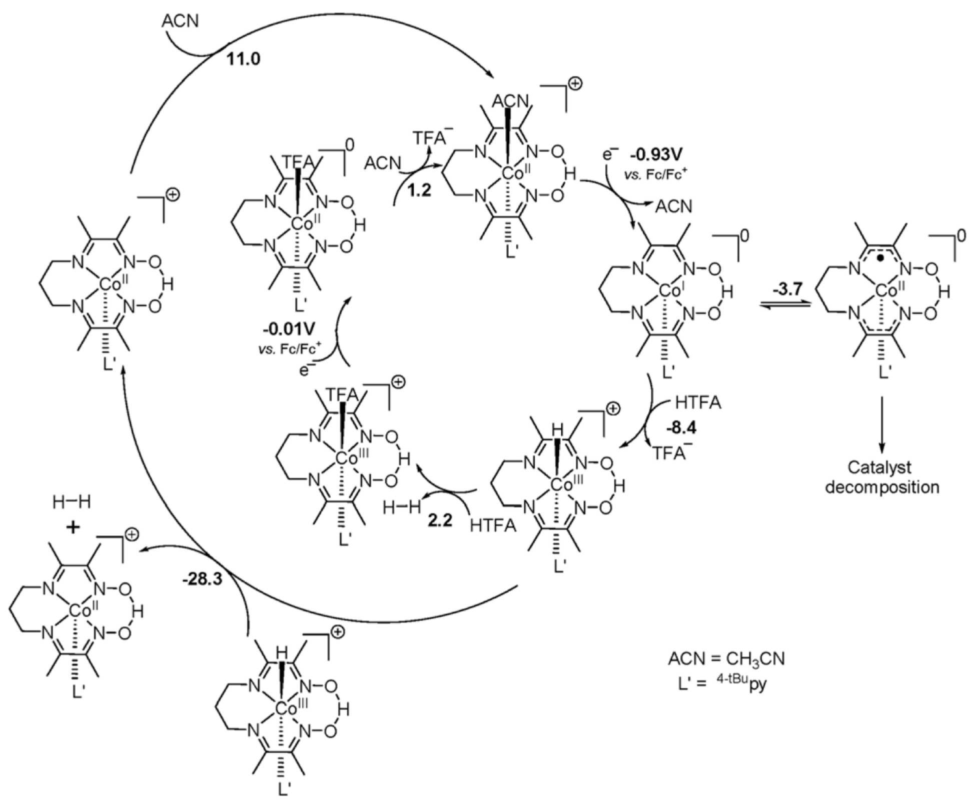

Figure 3.3. The catalytic pathways calculated for H_2 evolution by **1** in the presence of HTFA in CH_3CN (ACN). The formation of a Co^{III}–H species is invoked. This complex can react either heterolytically with a proton or homolytically with another Co^{III}–H complex to yield H_2. The heterolytic pathway involves an acetate-bound Co complex. The homolytic mechanism is more likely at low concentrations of acid. Energies given in kcal mol1 as calculated at the B3PW91//TZVP/6-311++G(d,p) level of theory.

D. Catalytic pathways for H_2 evolution

Previous studies[66,85-92] on hydrogen evolution by cobalt oximes propose the formation of a Co^{III}–H hydride intermediate, either by heterolytic $[LCo^{II}–H^{-}] + H^{+} \rightarrow [LCo^{II}] + H_2$ or by bimolecular homolytic $2[LCo^{II}–H^{-}] \rightarrow 2[LCo^{I}] + H_2$ pathways.

Complexes **1**–**3** displayed electrocatalytic waves in the presence of 10 equiv. HTFA (trifuoroacetic acid) at potentials close to the reduction of Co^{II}/Co^{I}. The respective $E_{1/2}^{H^+/H_2}$ are 1.03, 1.04 and 1.03 $V_{Fc/Fc+}$ and the Co_{II}/Co_{I} reduction potentials are 1.09, 1.07 and 1.09 $V_{Fc/Fc+}$ for **1**, **2**, and **3**, respectively. The catalytic pathway calculated for **1** is shown in Fig. 3.3.

3.4 Distinct Proton and Water Reduction Behavior with a Cobalt(III) Electrocatalyst Based on Pentadentate Oximes

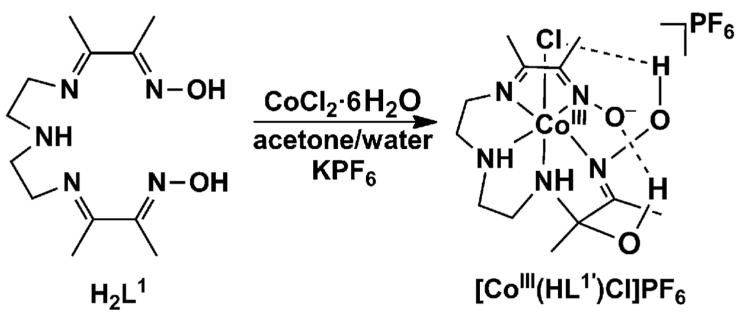

Figure 3.4. Synthetic scheme of the Co^{III} complex (**1**).

D. Basu and et al. have reported on a pentadentate N-rich oxime ligand H_2L^1, its coordination to Co^{II} and water incorporation through one of the imine double bonds to form the water-soluble catalytic species $[Co^{III}(HL^{1'})Cl]PF_6$ (**1**), shown in Figure 3.4. Catalyst **1** presents distinct mechanisms of H_2 generation in acidic organic media and in water.

A. The DFT-optimized geometries

The DFT-optimized geometries for **1** and its relevant reduced species are summarized in Figure 3.5. The parent Co^{III} complex displays a pseudo-octahedral geometry with two H-bonds, OH···O and OH···Cl.

A $1e^-$ reduction yields a $^{LS}3d^7$ Co^{II} complex, in which occupation of an antibonding e_g^*-like, Co-based $3d_{z^2}$ orbital weakens the metal–ligand interactions along the z-axis fostering an

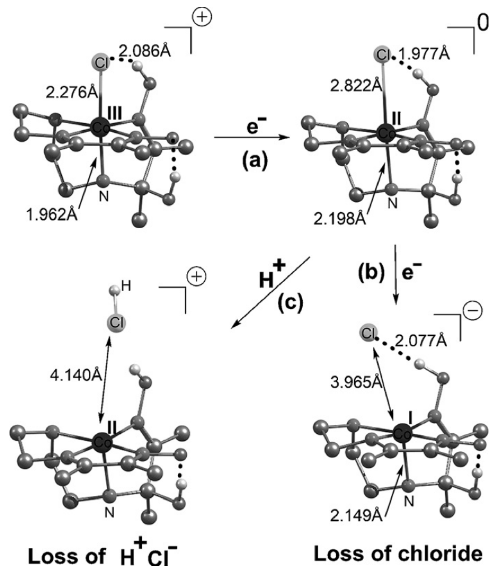

Figure 3.5. Calculated structures of species electrochemically generated in MeCN: a) Co^{III}/Co^{II} reduction, b) Co^{II}/Co^{I} reduction, and c) loss of chloride from the Co^{II} species in the presence of H^+.

increase in the Co–Cl and Co–N bond distances to 2.82 and 2.20 Å, respectively. The OH···Cl interaction becomes stronger as the H-bond distance decreases from 2.09 in **1** to 1.98 Å in the Co^{II} species. Dissociation of chloride from the later complex requires 6 kcal mol^{-1}. Reduction of the Co^{II} complex affords the five-coordinate and distorted square pyramidal Co^{I} species. At ca. 4 Å from the metal center, the Cl^- is no longer part of the coordination sphere. DFT calculations find that in presence of acid the addition of a proton on the Co^{II} species results in the loss of Cl^- as H^+Cl^- giving rise to the five-coordinate cationic Co^{II} complex (Figure 3.5). The later species can be further reduced to the corresponding Co^{I} complex. The reduction potentials of the $[Co^{II}(HL^{1'})]^+/[Co^{I}\text{-}(HL^{1'})]$ and $[Co^{II}(HL^{1'})Cl]/[Co^{I}(HL^{1'})Cl]^-$ couples are calculated as –1.65 and –1.89 $V_{Fc/Fc+}$, respectively. In addition to these two reduction mechanisms, reduction from $[Co^{II}(HL^{1'})Cl]$ directly to Co^{III} hydride $[Co^{III}(H)(HL^{1'})]$ without chloride loss from the Co^{II} complex (a proton-coupled electron transfer (PCET) mechanism) was also considered. The redox potential for the PCET Co^{II}/Co^{III}–H couple is calculated[89] as –1.55 $V_{Fc/Fc+}$. The anodic shift resulted from Cl^- loss from the Co^{II} complex is therefore 0.24 V for the non-PCET reduction mechanicsm and is in better agreement with the experimental value 0.18 V, whereas the shift in the potential from the PCET mechanism is 0.34 V and differs by 0.16 V from the experiment.

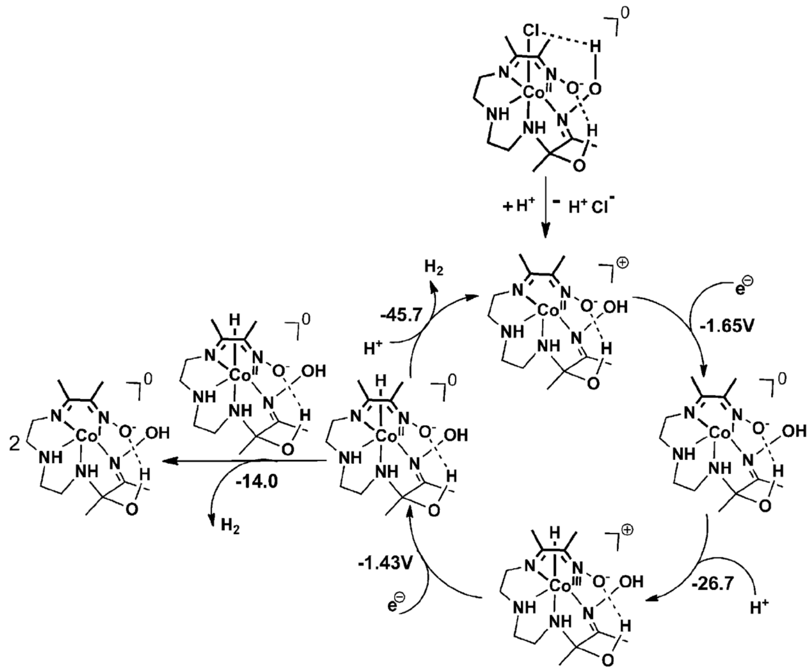

Figure 3.6. Catalytic mechanism of H_2 generation by **1** in MeCN. Free energy changes in kcal mol^{-1}.

B. DFT calculated mechanism of H_2 generation

The DFT-calculated mechanism of H_2 generation by **1** in acidic MeCN is shown in Figure 3.6. Binding of a proton to the Co^{I} complex results in the $2e^{-}$ oxidation of the latter giving rise to a Co^{III}–H (Co^{III} hydride) species. The Co^{III}–H complex can be reduced to a more reactive Co^{II}–H species at a potential of –1.43 $V_{Fc/Fc+}$. Uptake of another H^+ and generation of H_2 by this Co^{II}–H complex is favorable by 46 kcal mol^{-1} regenerating the five-coordinate Co^{II} complex to restart the cycle. The reaction of H^+ with the Co^{II}–H species is activationless.[89] Compared to the heterolytic mechanism, homolytic coupling of two Co^{II}–H units is unfavorable by ca. 32 kcal mol^{-1}.

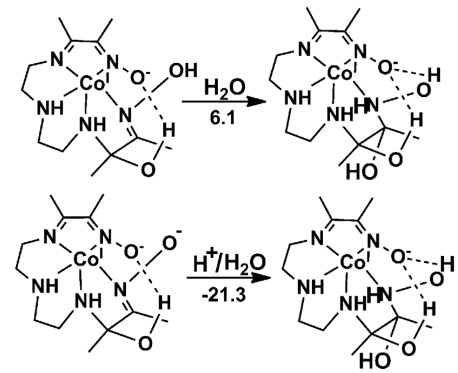

Figure 3.7. Possible pathways for the decomposition of the catalyst in water. Free-energy changes in kcal mol^{-1}.

C. Water incorportation

As calculated by DFT methods, addition of a water molecule to an isolated imine bond of the Co^{I} complex is energetically uphill by only 6 kcal mol^{-1} (Figure 3.7) and is feasible in the presence of a large excess of water. Incorporation of a water molecule into the imine bond of this deprotonated ligand backbone is significantly favorable by ca. 21 kcal mol^{-1} (Figure 3.7). These results indicate a possible pathways via water incorporation that can lead to catalyst decomposition and subsequent nanoparticle formation in water.

3.5 Ligand Transformations and Efficient Proton/Water Reduction with Cobalt Catalysts Based on Pentadentate Pyridine-Rich Environments

The $[N_2N^{py}{}_3]$ ligand L^{1H} ligand was treated with $CoCl_2{\cdot}6H_2O$, the initial $[Co^{II}(L^{1H})Cl]^{2+}$ (**1**) solution yielded a crystalline mixture of $[Co^{III}(L^{1C=N})Cl](ClO_4)^{2+}$ (**2**) and $[Co^{III}\text{-}(L^{1OMe})Cl]ClO_4$ (**3**) species(Scheme 3.2). $[Co^{III}(L^{1C=O})Cl]ClO_4$ (**4**) were obtained by recrystallizing the mixture of **2** and

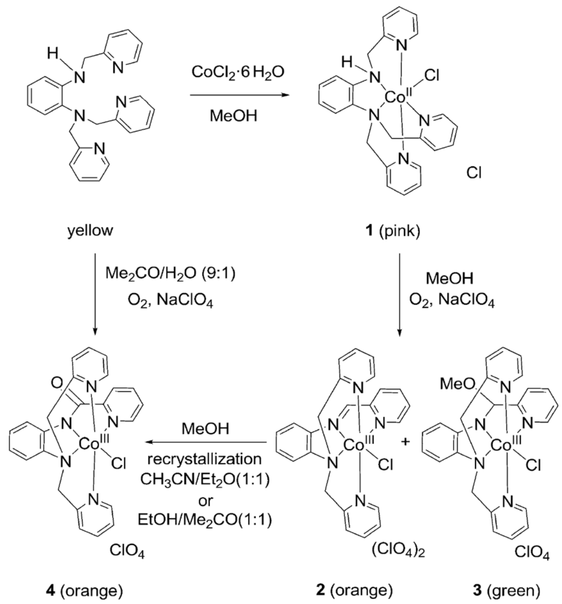

Scheme 3.2. Synthesis of Co^{III} complexes **2**, **3**, and **4**.

3. Furthermore, species **4** can be generated directly upon complexation of L^{1H} and $CoCl_2·6H_2O$ in acetone/water. $[Co^{II}(L^2)Cl]ClO_4$ (**5**) was isolated by counterion exchange with $NaClO_4$.

A. DFT Calculated hydroxy to amide conversion mechanism

A detailed density functional theory (DFT)[29] study was performed to evaluate details of the hydroxy to amide conversion mechanism (Figure 3.8). Calculations indicate that the transformation requires atmospheric $^3O_2$ to react with the C–H function of the intermediate hydroxy complex. The C–H hydrogen abstraction event is rate-limiting and nearly isoenergetic as the resulting intermediate **I** is about 2 kcal mol^{-1} higher than the starting hydroxy complex. In

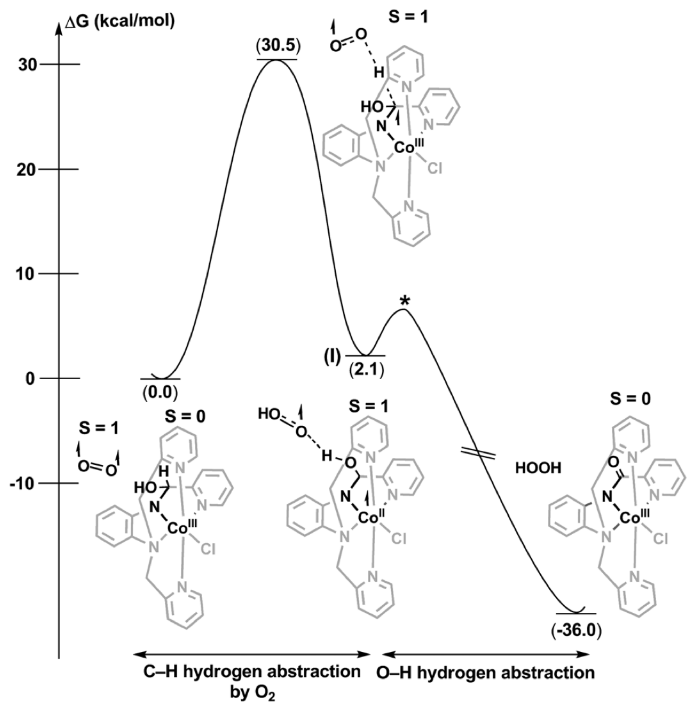

Figure 3.8. Reaction energy profile for the hydroxy to amide conversion in MeCN. The transition state * is not explicitly located.

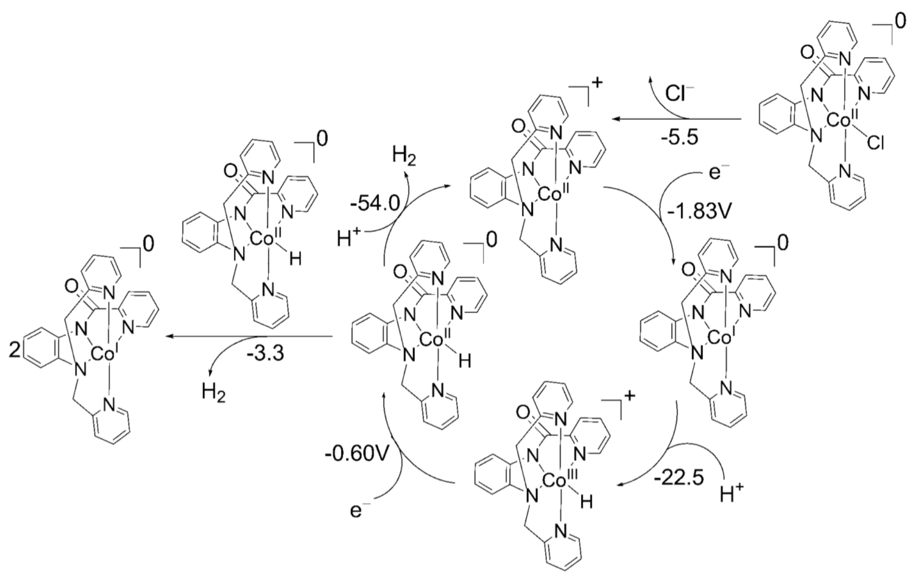

Figure 3.9. Catalytic mechanism of H_2 generation by **4** in MeCN. It involves a Co^{II}–H species that undergoes protonation to generate H_2. The calculated energetics for all events is reported as free energy changes in kcal mol^{-1}.

species **I** the hydroperoxo radical (·OOH) is weakly bonded to the hydroxy and the unpaired electron generated on the ligand is transferred to the metal center reducing it to Co^{II}. Thus, the metal center helps stabilize the radical intermediate **I** and makes the C–H hydrogen removal event nearly isoenergetic.[93] An intersystem crossing (triplet to singlet surface) from species **I** followed by the removal of the hydroxy hydrogen by the hydroperoxo radical gives rise to the amide complex **4** and the overall process is favored by about 38 kcal mol^{-1}. Geometry optimization of intermediate **I** on the singlet surface results in the transfer of the hydroxy hydrogen from the metal complex to the hydroperoxo radical, giving rise to **4**.

B. DFT calculated mechanism of H_2 generation for species 4 and 5

Mechanisms of electrocatalytic H_2 evolution by **4** and **5** have been evaluated by DFT calculations. Figure 3.9 describes the catalytic pathway for complex **4** in MeCN. The five-coordinate Co^{II} species, generated after dissociation of the chloro ligand, undergoes reduction to the corresponding Co^{I} complex. The reduction potential is calculated as 1.83 $V_{Fc/Fc+}$. Uptake of a proton by the Co^{I} complex is favorable by 22.5 kcal mol^{-1} and results in the six-coordinate Co^{III}–H^{-} complex, which gets reduced to the more reactive $^{HS}Co^{II}$–H^{-} species. The latter is high-spin in nature and occupation of the idealized e_g* MOs weakens the metal–ligand interactions. The Co–H bond elongates from 1.49 Å in the $^{LS}Co^{III}$ complex to 1.73 Å in the $^{HS}Co^{II}$ species. As a result, the hydride in the Co^{II}–H^{-} moiety is susceptible to heterolytic attack by an external proton. Uptake of a proton and generation of H_2 by this complex is favored by 54.0 kcal mol^{-1} (Figure 3.9), regenerating the five-coordinate Co^{II} complex to restart the catalytic cycle. The reaction of a proton with Co^{II}–H is expected to be activationless.[89] The homolytic pathway by the combination of two Co^{II}–H complexes is significantly less exothermic compared to the heterolytic mechanism. A proton-coupled electron transfer (PCET) event is not invoked for the Co^{II}/Co^{III}–H^{-} transformation, because no anodic shift was found in the experimental electrocatalytic measurement of **4** upon decrease of pH. Complex **5** follows a similar catalytic mechanism; however, the involvement of a

Co^{I}/Co^{II}–H PCET mechanism may be relevant. The generation of H_2 in both mechanisms favors a heterolytic pathway with another proton, rather than a bimolecular mechanism through the combination of two Co^{II}–H^{-} complexes.

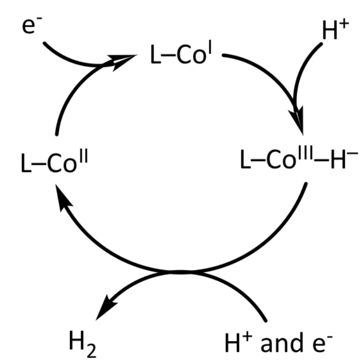

Scheme 3.3. Generalized H_2 generation mechanism.

3.6 Summary

In this chapter, density functional theory calculations were carried out to provide valuable information for the understanding of H_2 generation mechanism and its associated processes for the various cobalt based water splitting catalysts studied in this chapter.

In general, the proposed H_2 generation mechanisms based on our thermodynamical calculations are initiated by an active species, L–Co^{I}, which is in turn obtained by a one-electron or two-electron reduction of the parent species L–Co^{II} or L–Co^{III}, repectively. The active species Co^{I}–L then reacts with a proton to form cobalt hydride intermediate, L–Co^{III}–H^{-}, which can either be reduced further to form L–Co^{II}–H^{-} (easily react with another proton), or directly react with another proton to generate H_2 and recover L–Co^{II}, from which the active species L–Co^{I} can then be recovered. The cycle thus repeats. Although all of these steps were studied extensively by experiments conducted both in our collaborators' group, difficulties arise due to the unstable nature of cobalt hydride intermediate. By corroborating free energy change calculations of various chemical or electrochemical reacitons with experimentally available results, we can establish relatively good confidence in the DFT model chemistry; and the calculations of key reactions with highly unstable intermediate then in turn fill in the blanks left by experimental methods, resulting in deeper understing of H_2 generation mechnism generalized in Scheme 3.3.

CHAPTER 4 CONTROLLING CHEMICAL REACTIONS BY SHORT, INTENSE MID-INFRARED LASER PULSES: COMPARISON OF LINEAR AND CIRCULARLY POLARIZED LIGHT IN SIMULATIONS OF $CLCHO^+$ FRAGMENTATION

4.1 Introduction

Tunable mid-IR light can deposit energy efficiently into selected vibrational modes, with the potential of achieving mode-selective reactions that are otherwise energetically disfavored. However, this resonant excitation and consequent reactivity is easily defeated by intramolecular vibrational redistribution (IVR), unless sufficient energy can be absorbed quickly and reaction occurs more rapidly than IVR[94,95]. This requires very short, intense IR pulses. In previous studies[4,5], S. K. Lee et al. used Born-Oppenheimer molecular dynamics (BOMD) to simulate selective reaction acceleration for orientated molecules by linearly polarized mid-IR pulse for $ClCHO^+$, CF_3Br^+ and $C_6H_5I^{2+}$. While technically possible, the prerequisite of three-dimensional (3D) molecular orientation is still very challenging. Therefore, a more experimentally accessible approach is needed. Recently, electron dynamics driven by intense elliptically polarized laser field has attracted considerable attention because such dynamics revealed intimate correlation among electron, laser electric field and ionic cores[96,97]. However, whether elliptically polarized light could afford similar degrees of control over chemical reactions remains unexplored. In the present chapter we examine the fragmentation of $ClCHO^+$ by circularly polarized light and compare the results to our previous study with linearly polarized light. We show the answer to the aforementioned question is positive and also chemical control driven by circularly polarized light provides a real opportunity for experimental implementation.

There are three low energy channels for the dissociation of $ClCHO^+$. At the B3LYP/6-311G(d,p) level of theory the dissociation energies are:

$$\begin{aligned} ClCHO^+ + h\nu \;&\rightarrow\; Cl + HCO^+ \quad && 6.6\ \text{kcal/mol} \\ &\rightarrow\; H + ClCO^+ && 25.0\ \text{kcal/mol} \\ &\rightarrow\; HCl^+ + CO && 27.1\ \text{kcal/mol} \end{aligned}$$

Classical trajectory calculations on the ground state Born-Oppenheimer potential energy surface showed that when the initial kinetic energy is distributed statistically, or when the molecule is oriented randomly in a laser field, the Cl dissociation is dominant.[5] However, when a linearly polarized 7 μm laser pulse with a peak intensity of 2.9×10^{14} W/cm^2 is aligned in the plane of the molecule, the high energy channels can be greatly enhanced. In particular, when the polarization direction is approximately parallel or antiparallel to the C-H bond, H dissociation increases by a factor of 3 over random orientation, and when the direction is perpendicular to the C-H bond and in the plane of the molecule, the yield of HCl^+ is increased by a factor of 10. In the present study, we examine whether linearly polarized light can be used to generate the cation with a degree of alignment and explore dissociation by circularly polarized light aligned so that the electric field vector rotates in the plane of the molecule. The coordinate system for the simulation is shown in Scheme 4.1. We start by using time-dependent configuration interaction calculations of the angular dependence of ionization to see if the cation can be prepared with some degree of alignment with linearly polarized light. Molecular dynamics simulations for the fragmentation of aligned $ClCHO^+$ are then carried out with circularly polarized light using a 4 cycle 7 μm pulse with a peak intensity of 1.26×10^{14} W/cm^2 (this deposits an amount of energy similar to linearly polarized light with an intensity of 2.9×10^{14} W/cm^2). The branching ratios and the distributions of the energies and angular momenta are compared for linearly and circularly polarized light.

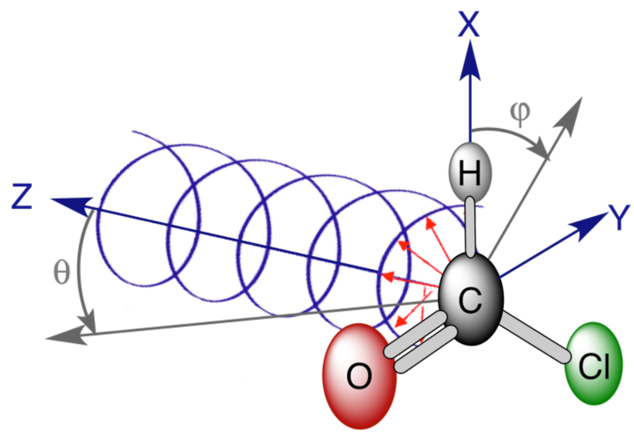

Scheme 4.1. Coordinate system for the simulation of circularly polarized light propagating along the z axis interacting with $ClCHO^+$ in the xy plane oriented so that the C-H bond is along the x axis; θ is the polar angle with the z axis and ϕ is the in-plane angle with the C-H bond.

4.2 Method

The angular dependence of ionization of neutral ClCHO was simulated by time dependent configuration interaction calculations with a complex absorbing potential.[98-101]

$$i\frac{\partial}{\partial t}\Psi_{el}(t) = [\hat{\mathbf{H}}_{el} - \hat{\vec{\mu}}\cdot\vec{E}(t) - i\hat{\mathbf{V}}^{absorb}]\Psi_{el}(t) \qquad \Psi_{el}(t) = \sum_{i=0} C_i(t)\left|\Psi_i\right\rangle \qquad (1)$$

where $\hat{\mathbf{H}}_{el}$ is the field-free electronic Hamiltonian. The electron-light interaction is treated in the semi-classical dipole approximation, where $\hat{\vec{\mu}}$ is the dipole operator and $\vec{E}$ is electric field component of the laser pulse. The absorbing potential used to model ionization, $-i\hat{\mathbf{V}}^{absorb}$ is constructed from a set of overlapping spherical potentials around each atom. Each spherical potential has a quadratic rise starting at 3.5 times the van der Waals radius R_{vdw} and a quadratic turn-over to constant value of 10 hartree at approximately R_{vdw} + 7 Å. The time-dependent wavefunction is constructed from the field-free Hartree-Fock ground state and all singly excited configurations. The computations employed the aug-cc-pVTZ basis set[102,103] plus a large set of diffuse functions, for a total of 289 basis functions and 2278 singly excited states. The time-dependent coefficients were propagated using a Trotter factorization of the exponential of the Hamiltonian. A 4-cycle linear polarized 7 μm sine squared pulse with a maximum field strength of 0.06 au (corresponding to a peak intensity of 1.26×10^{14} W/cm^2) was used for the simulation of the ionization. The ionization yield was taken as the loss of norm of the wavefunction and was plotted as a function of the polarization direction of the pulse. Details of the procedure and validation of the methodology are described in a series of earlier papers[98-101].

Dissociation was simulated by classical trajectory calculations on the ground state Born-Oppenheimer surface for aligned formyl chloride cations in the time varying electric field of laser pulse. The laser field was a 4 cycle 7 μm trapezoidal pulse (95 fs full width). This corresponds to 1430 cm^{-1} and a width of ca 300 cm^{-1}, and should interact strongly with a range of molecular vibrations. For circularly polarized light, the propagation direction was perpendicular to the plane of the molecule with the electric field rotating in the plane of the molecule with a maximum field strength of 0.06 au. For linearly polarized light, the polarization direction was in the plane of the molecule and the direction was varied from ϕ = 0° to 360° in steps of 30° with a maximum field strength of 0.06 au and steps of 90° with a maximum field strength of 0.09 au. Trajectories were integrated for a total of 400 fs. The B3LYP/6-311G(d,p) level of theory is a suitable compromise between accuracy of the potential energy surface and efficiency in the trajectory calculations.

Molecular dynamics calculations were carried out with the development version of the Gaussian series of programs[30] and the PCvelV integrator[104] with a step size of 0.25 fs and Hessian updating[105,106] for 20 steps before recalculation. The starting structures had no rotational energy; zero-point vibrational energy was added to the initial structures using orthant sampling of the momentum[107]. Trajectories that gained large amounts of energy due to unphysically large charge oscillations within a single laser cycle were discarded as artifacts of the Born-Oppenheimer approximation. Trajectories were classified into specific channels (Cl + HCO^+, H + $ClCO^+$, HCl^+ + CO, no reaction) based on bond lengths.

4.3 Results and Discussion

The angular dependence of the ionization yield for ClCHO is shown in Figure 4.1(a) for a 7 μm linearly polarized laser pulse with a maximum field strength of 0.06 au (1.26×10^{14} W/cm^2). The ionization yield is about 80% larger for polarization directions in the plane of the molecule than for perpendicular to the plane. Interestingly, for in-plane directions, the yield is about 65% greater when the polarization is aligned with the C-Cl bond compare to perpendicular to the bond. Therefore ionization with linearly polarized light should result in appreciable alignment of the cation. This also suggests a certain degree of planar alignment of the ions might be achieved via ionization using circularly polarized light with the electric field rotating in the plane of the molecule. Population analysis of the wavefunction shows that the cation is formed primarily by removal of an electron from the highest occupied orbital (an in-plane Cl lone pair orbital) as shown in Figure 4.1(b). Some ionization from HOMO-1 (π-type Cl lone pair orbital) and HOMO-2 (the other in-plane Cl lone pair orbital) can also be seen.

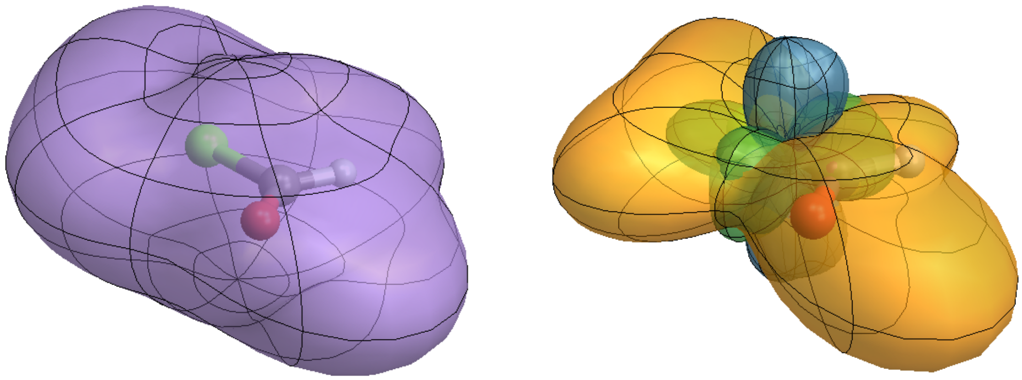

(a) (b)

Figure 4.1. Angular dependence of (a) the total yield for the ionization of ClCHO as a function of the polarization direction and (b) the contributions of the HOMO (yellow), HOMO-1 (blue) and HOMO-2 (green) to the total ionization yield. The radial distance of the surface is proportional to the ionization yield for the corresponding polarization direction of a 4 cycle 7 μm linearly polarized sine squared laser pulse with a maximum field strength of 0.06 au.

The dissociation of $ClCHO^+$ was simulated by Born-Oppenheimer molecular dynamics. Approximately 65% of the ionization in the molecular plane comes from the HOMO and yields the cation in its ground state. Depending on their lifetimes, excited states of the cation could also contribute to the dissociation, but this is beyond the scope of the present study. Dissociation on the ground state potential energy surface induced by linear and circularly polarized, intense mid-IR laser pulses can be compared with simulations of field-free fragmentation of activated $ClCHO^+$ that has enough initial vibrational energy to easily overcome the dissociation barriers for the 3 channels of interest.[5] Our previous study showed that in the field-free case the Cl channel was favored at lower initial energies and, as expected, the fraction of the higher energy H and HCl^+ channels increased for greater initial energies (see Table 4.1). Dissociation of unactivated $ClCHO^+$ by circular polarized pulses with a maximum field strength of 0.06 au yields more H + $ClCO^+$ and less Cl + HCO^+ than the activated field-free cases. The branching ratios for right and left circularly polarized light are similar but not identical. Standard deviation for the branching ratios is 2-3% as estimating from the statistical uncertainty of √N. Thus the difference in the branching ratios between right and left circularly polarized light may not be statistically significant. The results for circularly polarized pulses with a maximum field strength of 0.06 au can be compared to linearly polarized pulses averaged over ϕ = 0 - 360°. The yield of H and HCl^+ is much less for linear polarized light than for circularly polarized light with the same maximum field strength. The field strength for the linear polarized pulses must be raised from 0.06 au to 0.09 au to obtain a comparable fraction of higher energy products. Thus, for a given maximum field strength, circularly polarized light is more effective than linearly polarized light in producing higher energy fragmentation products.

Table 4.1. Branching ratios for the dissociation of $ClCHO^+$ interacting with circular and linear polarized laser pulses.

Polarization	Field strength (au)	Branching ratio		
		$Cl + HCO^+$	$H + ClCO^+$	$HCl^+ + CO$
Field-free [a]	0	71%	18%	8%
Field-free [b]	0	55%	24%	21%
Left circular [c]	0.06	30%	47%	23%
Right circular [d]	0.06	29%	52%	19%
Linear (0 - 360° averaged) [e]	0.06	81%	15%	4%
Linear (0 - 360° averaged) [f]	0.09	57%	22%	21%

[a] 100 trajectories with 37.8 kcal/mol initial vibrational energy[5]; ca. 3% did not dissociate. [b] 300 trajectories with 54.0 kcal/mol initial vibrational energy[5]; ca. 2% did not dissociate. [c] 800 trajectories; ca. 5% did not dissociate. [d] 800 trajectories; ca. 4% did not dissociate. [e] 4800 trajectories; ca. 41% did not dissociate. [f] 1600 trajectories; ca. 12% did not dissociate.

As indicated by the simulations of activated $ClCHO^+$ in the field free case, the branching ratios for the products should depend on the amount of internal energy. Table 4.2 lists the average total energy absorbed by $ClCHO^+$ interacting with circularly and linearly polarized laser pulses. Circularly polarized light deposits approximately twice as much energy as linearly polarized light with the same maximum field strength. This is because a circularly polarized light pulse can be decomposed into two perpendicular linearly polarized pulses with the same intensity and a phase difference of ±90°. Since the energy of a classical wave is proportional to the amplitude squared, linearly polarized light with a field strength of 0.09 au deposits approximately twice as much energy as with a field strength of 0.06 au. The increased energy deposited by linearly polarized light with a field strength of 0.09 au brings the branching ratio closer to that of circularly polarized light with a field strength of 0.06 au (see Table 4.1).

Table 4.2. Average total energy absorbed by $ClCHO^+$ interacting with circular and linear polarized laser pulses.

Polarization[a]	Field Strength (au)	Total energy(kcal/mol)			
		All Channels	Cl + HCO^+	H + $ClCO^+$	HCl^+ + CO
Left circular	0.06	89.3±40.7	59.1±25.1	94.4±35.3	119.2±41.0
Right circular	0.06	99.7±54.9	59.4±28.5	123.7±59.9	95.1±26.1
Linear (0 - 360° averaged)	0.06	38.4±17.2	33.8±12.2	57.5±20.2	59.1±24.9
Linear (0 - 360° averaged)	0.09	86.1±44.7	65.8±28.2	112.6±62.9	106.9±35.1

[a] see footnotes of Table 1 for trajectory details

The amount of energy deposited by linearly polarized light depends on the reaction channel (Table 4.2) and the orientation of the field (Figure 4.2). For both linear and circularly polarized light, the products of the lower energy Cl + HCO^+ channel gain only about 1/2 to 2/3 as much energy as the products of the higher energy H + $ClCO^+$ and HCl^+ + CO channels. For the H + $ClCO^+$ channel, the most energy is absorbed when the polarization is nearly parallel with the C-H bond (Fig. 4.2b). Similarly for the HCl^+ + CO channel, the highest amount of energy is absorbed for polarization directions between the C-H and C-Cl bonds (Fig. 4.2c). The branching ratios shown in Figure 4.2d are in qualitative agreement with the angular dependence of the energy absorbed.

The yield is greatest for the low energy Cl + HCO^+ channel, which has a broad maximum when the polarization is roughly parallel to the C-Cl bond. There is a decrease in the Cl yield (and a corresponding sharp rise in the number of unreactive trajectories) when the field is perpendicular to the C-Cl bond. This indicates that the coupling of between the laser field and the molecule is strong when the polarization direction is aligned with the C-Cl bond, but weaker when the direction is perpendicular to the C-Cl bond. The H + $ClCO^+$ channel has a broad maximum when the field is roughly parallel or antiparallel to the C-H bond, leading to an enhancement of about 2 compared to the average over ϕ = 0 - 360°. Similarly, the HCl^+ + CO channel has a broad maximum when the field is approximately perpendicular to the C-H bond, yielding an enhancement of 2 - 3. This angular dependence of the branching ratios for linearly polarized light is more pronounced at higher field strengths. In a previous paper, we found an order of magnitude increase in the HCl^+ branching ratio when a field 0.09 au was oriented perpendicular to the C-H bond.

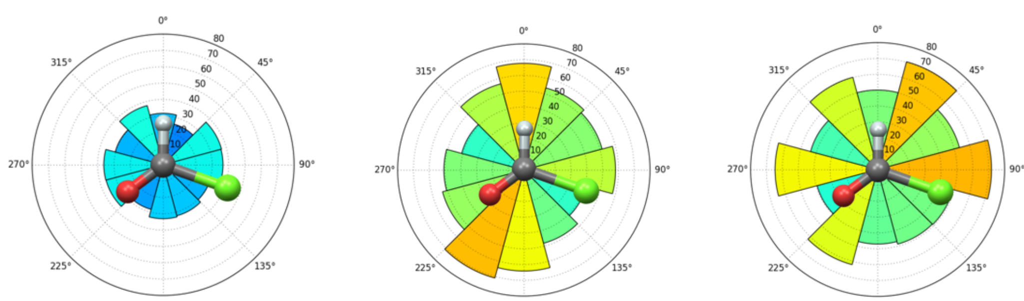

(a) (b) (c)

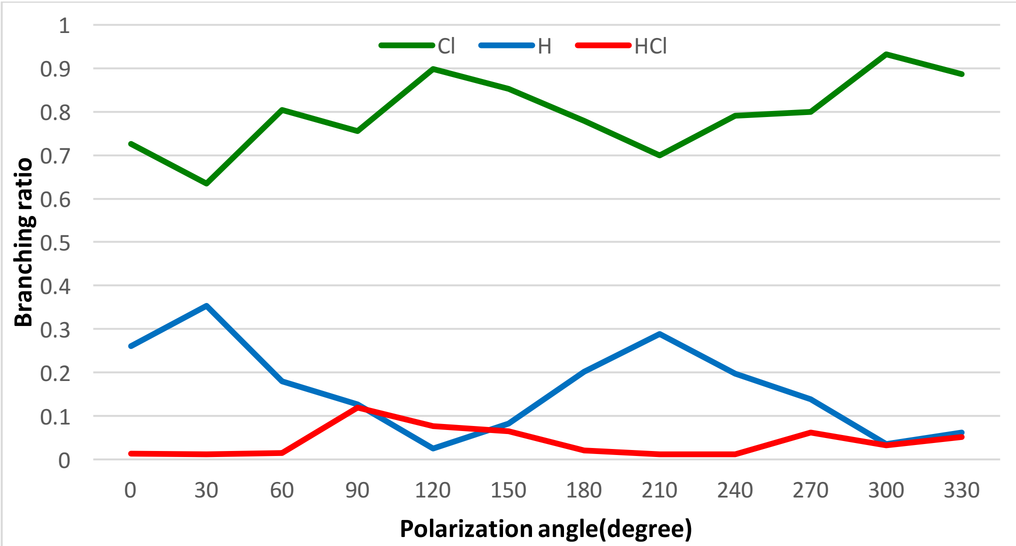

(d)

Figure 4.2. Energy deposited as a function of the in-plane angle ϕ of the direction of linearly polarized light with a field strength of 0.06 au for (a) Cl + CHO^+, (b) H + $ClCO^+$, and (c) HCl^+ + CO; (d) branching ratio as a function of the in-plane angle ϕ of the direction of linearly polarized light with a field strength of 0.06 au.

The distributions of product total angular momenta are shown in Figure 4.3. In the simulations, the electric field vectors for both linearly and circularly polarized laser pulses are in the plane of the molecule. Consequently, the dissociating fragments remain close to the molecular plane and the angular momentum vectors are mainly perpendicular to the plane ($\theta \approx 0°$ and 180°). Similar to the distribution of the energy absorbed, the magnitudes of the angular momenta cover a broad range. Except for very small magnitudes of the angular momentum, all of the dissociating trajectories for right circularly polarized light are close to $\theta = 0°$ and those for left circularly polarized light are close to $\theta = 180°$. For linearly polarized light, the magnitudes of the angular momenta are larger and both directions $\theta \approx 0°$ and $\theta \approx 180°$ are found, depending on the direction of the polarization.

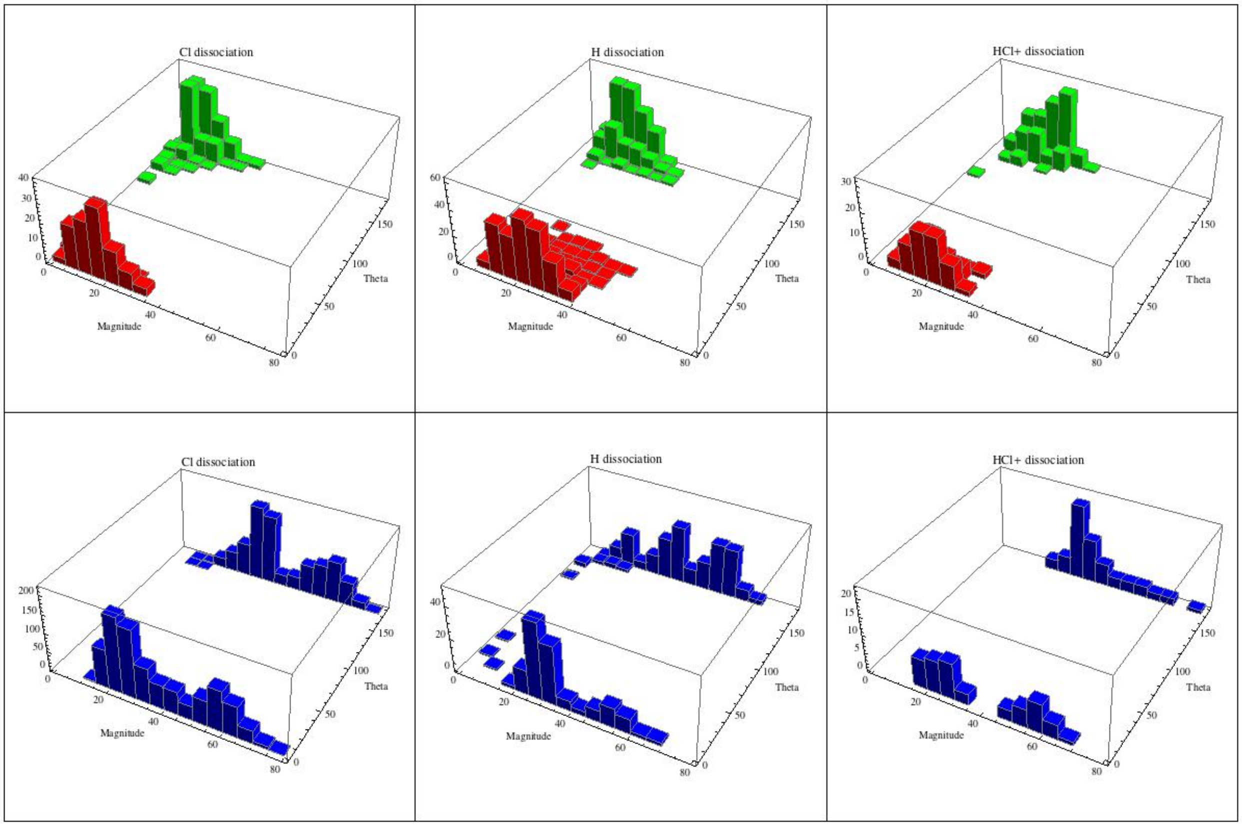

Figure 4.3. Magnitude and direction of the total angular momentum for the Cl + HCO^+, H + $ClCO^+$ and HCl^+ + CO channels with 0.06 field strength for left circularly polarized light (top row, green), right circularly polarized light (top row, red) and linearly polarized light averaged over ϕ = 0 - 360°(bottom row, blue).

The angular momentum of the products results from the interaction of the electric field of the light with the permanent dipole and polarizability of the molecule. For $ClCHO^+$ in a field of 0.06 au, these term account for ca 90% of the interaction energy. The potential energy of a polarizable homonuclear diatomic in an electric field is $V(\phi) = -\frac{1}{2}\varepsilon^2(\alpha_{\parallel}\cos^2\phi + \alpha_{\perp}\sin^2\phi)$ and the torque is $\tau = -dV/d\phi$, where $\alpha_{\parallel}$ > $\alpha_{\perp}$ are the polarizabilities parallel and perpendicular to the bond. The diatomic system experiences a maximum positive torque for ϕ = -45°, +135° and a maximum negative torque for ϕ = +45°, -135°. Figure 4.4 shows total angular momentum of the products as a function of the direction of linearly polarized light. The major axis of the polarizability tensor for $ClCHO^+$ is along the C-Cl bond. The magnitudes of the total angular momenta have maxima at approximately ±45° and ±135° to the C-Cl bond (Fig. 4.4a-c), and the polar angle θ of the angular momentum alternates between 0° and 180° as the field is rotated (Fig. 4.4d), analogous to the behavior of a simple polarizable diatomic molecule in a strong field.

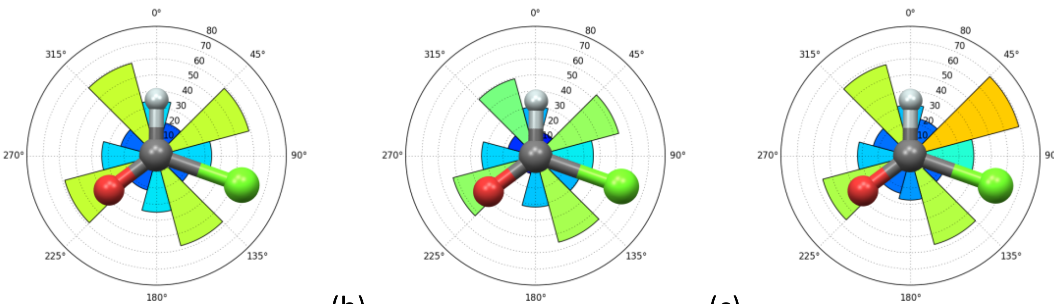

(a) (b) (c)

(d)

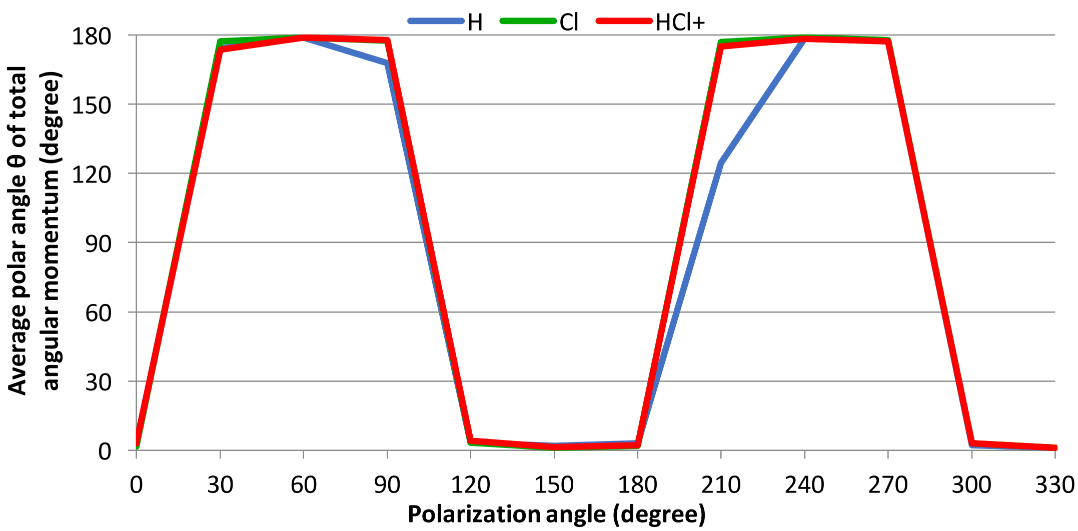

Figure 4.4. Total angular momentum of the products as a function of the in-plane angle φ of the direction of linearly polarized light with a field strength of 0.06 au for (a) Cl + CHO^+, (b) H + $ClCO^+$, and (c) HCl^+ + CO; (d) polar angle θ for the total angular momentum as a function of the in-plane angle φ of the direction of linearly polarized light with a field strength of 0.06 au.

For low field strengths, the coupling between light and molecular vibrations depends on the change in the dipole moment with respect to the geometric parameters, or equivalently, the change in the forces on the atoms with the applied electric field ($-d\mu/dR = dg/d\varepsilon = d^2E/dRd\varepsilon$). For higher field strengths, the response of the molecule to the external field can dominate the interaction. Figure 4.5 shows the Mulliken charge distribution as a function of time for $ClCHO^+$ in right and left circular polarized pulse and for two orientations of a linearly polarized pulse. The largest oscillations in charge are for the chlorine and for the oxygen. For linearly polarized light at ϕ = 0° and 90°, oscillations in chlorine and oxygen are nearly equal and opposite. For circularly polarized light, the charges change most when the rotating field is aligned with the bond. As a result the oscillation of the charge on the chlorine either leads or lags behind the oscillation of the charge on the oxygen, depending on direction of rotation of the electric field of the circularly polarized light. This phase difference may lead to the difference in the total angular momentum seen in the dissociation of $ClCHO^+$ induced by right and left circularly polarized light.

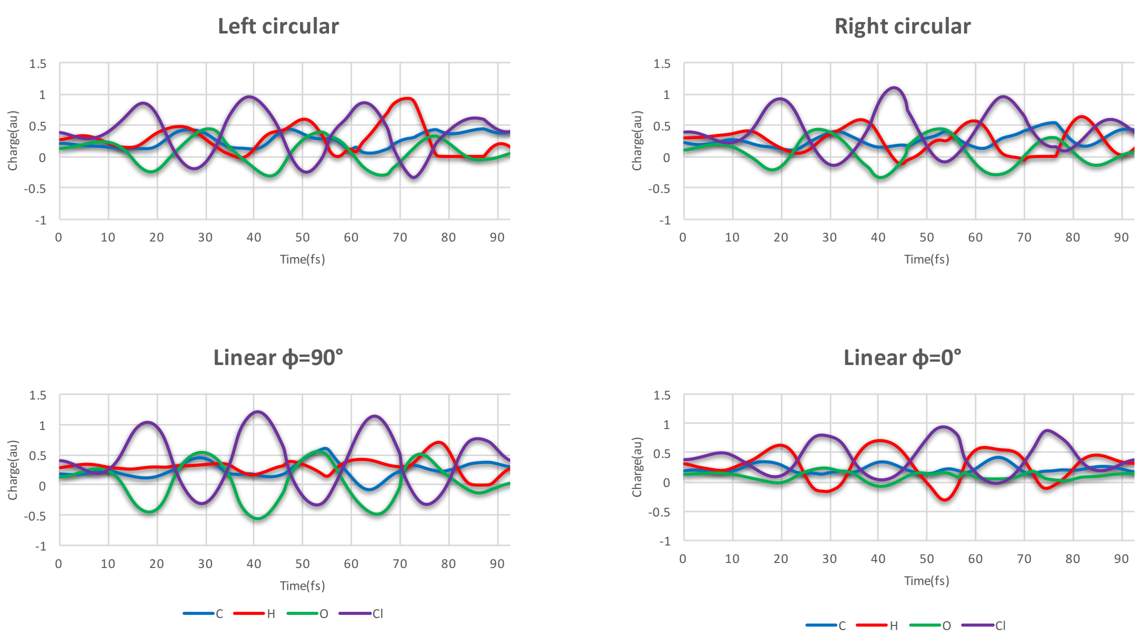

Figure 4.5. Mulliken charges as a function of time during the pulse for (a) left circularly polarized light, (b) right circularly polarized light, (c) linearly polarized light with ϕ = 90 (aligned with the CH bond), and (d) linearly polarized light with ϕ = 0 (aligned perpendicular to the CH bond) (0.06 au field strength for circular polarized light and 0.09 au field strength for linear polarized light).

4.4 Summary

The present simulations for $ClCHO^+$ show that circularly polarized light is more effective than linearly polarized light of the same peak intensity in depositing energy and causing fragmentation. This results in a higher yield of high energy products for circularly polarized light. The branching ratios and energy absorbed are similar for right and left circularly polarized light, but the total angular momentum vectors have opposite directions. Even though linearly polarized light deposits less total energy, it yields higher values of the total angular momentum than circularly polarized light. At these high field strengths, the coupling with the light is dominated by the polarizability of the molecule. For linearly polarized light, this can be seen from the angular dependence of the increase in energy and angular momentum, and from the charge fluctuations. Our calculation also suggests the possibility of implementing such an experiment with a single laser achieving ionization of neutral and control of ion fragmentation at the same time.

CHAPTER 5 CONTROLLING CHEMICAL REACTIONS BY SHORT, INTENSE MID-INFRARED LASER PULSES: TWO INDEPENDENTLY OSCILLATING LINEARLY POLARIZED PULSES IN SIMULATIONS OF CLCHO$^+$ FRAGMENTATION

5.1 Introduction

The goal of the present chapter is to see if better reaction selectivity can be achieved with two independent laser pulses. Similar to the previous chapter, we use Born-Oppenheimer molecular dynamics (BOMD) to simulate selective reaction acceleration for orientated molecules by linearly polarized mid-IR pulses. In a previous study of $ClCHO^+$,[5] a 7 μm pulse perpendicular to the C–H bond direction was shown to enhance the higher energy HCl^+ dissociation channel. In the present chapter, we use two pulses of equal length but different frequencies, and explore the effect of changing the frequencies, polarization orientations and relative timing of the pulses. Due to the complexity of the effects resulting from the superposition of two laser pulses, and the need to interpret the statistical significance of hundreds of trajectories, we need to consider more advanced techniques for analyzing the results.

5.2 Method

The simulations of dissociation were carried out by classical trajectory calculations on the ground state Born-Oppenheimer surface for aligned formyl chloride cations in the time varying electric field of the laser pulses. The laser field consists of two independently oscillating linear polarized sine squared pulses with a maximum field strength of 0.03 au (corresponding to a peak intensity of 3.15×10^{13} W/cm^2) with 3.5, 7, 10.5 μm wavelengths (to promote different vibrational modes, i.e. C–H stretching, C–O stretching, and C–H rocking; see Table 5.1). These wavelengths correspond to 2857, 1428 and 952 cm^{-1} respectively, and should interact strongly with a range of molecular vibrations. The number of cycles for each wavelength was chosen to keep the total pulse duration the same, 560 fs. The polarization direction was in the plane of the molecule and was aligned with the vibrational mode that each of the laser frequency was chosen to promote. Trajectories were integrated for a total of 1200 fs; 200 trajectories were calculated for each pulse sequence. The B3LYP/6-311G(d,p) level of theory is a suitable compromise between accuracy of the potential energy surface and efficiency in the trajectory calculations. Molecular dynamics calculations were carried out with the development version of the Gaussian series of programs[30] and the PCvelV integrator[104] with a step size of 0.25 fs and Hessian updating[105,106] for 20 steps before recalculation. The starting structures had no rotational energy; zero-point vibrational energy was added to the initial structures using orthant sampling of the momentum[107]. Trajectories that gained large amounts of energy due to unphysically large charge oscillations within a single laser cycle were discarded as artifacts of the Born-Oppenheimer approximation. Based on previous experience with BOMD trajectories, most of such artifacts occur when hydrogen atom moves very far away (>10 Å) from the rest of the molecule while still in the oscillating laser field. Therefore, trajectories having such problems are predominantly undergoing H dissociation for the molecule of interest. Trajectories were classified into specific channels (Cl + HCO^+, H + $ClCO^+$, HCl^+ + CO, no reaction) based on bond lengths. Energy transfer from the laser field was analyzed by performing Continuous Wavelet Transformation (CWT) on the vector components of the square-root-mass-weighted velocities of the individual atoms.

Table 5.1. Vibrational modes calculated at the B3LYP/6-311G(d,p) level for ClCHO+ and all possible fragments resulted from the dissociation channels considered.

species	mode	frequency (cm^{-1})
$ClCHO^+$	O–C–Cl bend	232.62
	C–Cl stretching	731.75
	O,Cl,H wagging	907.82
	C–H rocking	1173.65
	C–O stretching	1506.83
	C–H stretching	2983.30
H + $ClCO^+$	O–C–Cl bend	450.50
	C–Cl stretching	863.01
	C–O stretching	2376.15
Cl + HCO^+	C–H rocking	865.00
	C–H and C–O symmetric stretching	2270.09
	C–H and C–O anti-symmetric stretching	3229.25
CO + HCl^+	C–O stretching	2219.82
	H–Cl stretching	2635.08

5.3 Branching ratio and energy absorption comparison

S. K. Lee et al.[5] showed that a 7 μm laser pulse perpendicular to C–H bond for $ClCHO^+$ promotes the high energy HCl^+ dissociation channel most successfully. Hence this arrangement serves as a good point of reference for comparison with the various dual laser pulse sequences proposed here. Due to the low field strength used, 0.06 au (combining two identical 0.03 au pulses), the 7 μm pulse perpendicular to C–H bond did not produce very many high energy HCl^+ dissociations (Table 5.2). However, a 3.5 μm pulse along the C–H stretching mode combined with a 10.5 μm pulse along the C–H rocking mode gives a much higher percentage of the higher energy HCl^+ products. It should also be noted that the average amount of energy absorbed from these two laser pulse sequences is very similar (Table 5.2), indicating that the difference in the branching ratio was not a result of differences in the amount of energy deposited into the vibrational modes by the laser pulses. This suggests that a more complex mechanism may be involved in promoting the higher energy HCl^+ channel. We propose that the C–H stretching mode needs to be sufficiently energized before the C-H rocking mode bends the H atom toward Cl forming a H–Cl bond while the C–Cl bond is breaking. This concerted process requires less energy than C–H bond breaking. If this hypothesis is true, then the relative timing of the 3.5 µm and 10.5 µm pulses could matter. This is indeed the case when the delay is one quarter of the pulse duration. Having the 3.5 µm pulse along the C–H stretching mode come first resulted in 72.7% HCl^+ dissociation vs. 38.2% HCl^+ dissociation when the 10.5 µm pulse along the C–H rocking mode comes first. This contrast disappears when the delay between two pulses is extended to half of the pulse duration. The difference in the energy gained from the laser is considerably larger when the delay between the two pulses is one quarter of the pulse duration (ca 20 kcal/mol), compared to a delay of half of the pulse duration (ca 10 kcal/mol).

Table 5.2. Branching ratio and total energy absorption as the result of different laser fields

first pulse	second pulse	delay between two pulses	branching ratio Cl dissociation	branching ratio HCl^+ dissociation	energy absorption (kcal/mol) Cl dissociation	energy absorption (kcal/mol) HCl^+ dissociation
7 µm perpendicular to C–H bond	7 µm perpendicular to C–H bond	None	77.6%	18.8%	73.9±61.9	106.3±46.4
3.5 µm C–H stretching	10.5 µm C–H rocking	None	36.6%	62.4%	74.1±41.3	112.2±30.4
3.5 µm C–H stretching	10.5 µm C–H rocking	½ of the first pulse	55.9%	40.7%	64.7±38.0	106.4±26.9
10.5 µm C–H rocking	3.5 µm C–H stretching	½ of the first pulse	65.2%	33.3%	60.5±36.2	92.9±24.0
3.5 µm C–H stretching	10.5 µm C–H rocking	¼ of the first pulse	25.5%	72.7%	63.7±39.9	115.85±30.9
10.5 µm C–H rocking	3.5 µm C–H stretching	¼ of the first pulse	60.3%	38.2%	69.3±34.9	95.1±21.0

5.4 Continuous wavelet transformation analysis

In order to better understand how the energy is deposited into different vibrational modes over a period of time, a more sophisticated analysis method is needed. Windowed Fourier transformation (or Short-time Fourier transformation) was the first analysis method used in an attempt to resolve the frequency domain information, i.e. how much energy is deposited into atomic motions of different frequency during a small sliding time window, and how does this information evolve over the entire simulation time. This effort was ultimately unsuccessful because the window width needed to span the vibrational frequencies considered, ca. 500–3000 cm^{-1}, results in a time-frequency resolution that is too low. Fortunately, wavelet transformation has the distinct advantage of having an adaptive time-frequency resolution, i.e. a higher time-domain resolution at higher frequencies (at the expense of frequency-domain resolution, constrained by uncertainty principle). Here we apply the continuous wavelet transformation (CWT) as opposed to the more popular discrete wavelet transformation (DWT). The redundancy of information resulting from CWT is beneficial to human interpretation of peaks in a CWT spectrum while DWT was designed to remove such redundancy. CWT was used to analyze the components of the square root mass weighted atomic velocity vector, which is a direct measurement of the molecular kinetic energy. Four important peaks corresponding to vibrational or rotational modes in both the parent molecule $ClCHO^+$ and its dissociation fragments are identified in our CWT analysis (Figure 5.1), namely C–H stretching (CH str) and C–H rocking (CH rock) in $ClCHO^+$ and CHO^+, C–O stretching (CO str) in HCO^+ for Cl dissociation or in CO for HCl^+ dissociation, and HCl^+ rotation in HCl^+ fragment. It should be pointed out that the scalogram plot for each set in Figure 5.1 is the average over transformations performed individually for each trajectory in the set and thus represent the overall behavior of the set. Such averages are only possible due to the additive nature of power spectrum after the continuous wavelet transformation. Since the signal in the scalograms corresponds to the response of the atomic motion to the laser pulse, the enhancement of these peaks indicates two possibilities: a) increased energy deposit into a specific vibrational mode by directly interacting with the laser field; b) a certain vibrational (rotational) mode begins to appear as significant structural change appears, as a result of or as a precursor of dissociation.

We now look at the CWT scalogram plots for six sets of trajectories, i.e. three laser pulse sequences and two dissociation channels. The C–H stretching peaks at ca. 3000 cm^{-1} in all the plots could best be attributed to response to the laser field since it is the highest energy vibrational mode and thus unlikely to be promoted thermally. Moreover, the stronger enhancement of this mode only appears around peak laser intensity (200-400 fs) and when the interfering 10.5 µm pulse along C–H rocking direction (perpendicular to C–H stretching mode) is delayed. The increased energy in the C–H rocking mode at ca. 900 cm^{-1} in all cases corresponds to the time when the 10.5 µm pulse along C–H rocking direction (perpendicular to the C–H bond) reaches its peak intensity. The disappearances of this peak correlates very nicely with the average dissociation time for both the Cl and HCl^+ dissociation channels. For Cl dissociation, this peak shifts to a lower frequency bend in HCO^+. Most interestingly, both the C–H rocking and C–H stretching peaks are noticeably more intense (particularly C–H stretching) when the 3.5 µm pulse comes before the 10.5 µm pulse than for the other two pulse sequences. This indicates that the response of the molecule to the 10.5 µm pulse interacts with the response to the 3.5 µm pulse.

For Cl dissociation, the peak at ca. 2000 cm^{-1} can be assigned to C–O stretching mode in any of the possible fragments (2200–2376 cm^{-1}) except for the parent molecule $ClCHO^+$ (1507 cm^{-1}) since the frequency resolution in this region is ca. 200 cm^{-1}. Although this peak does not seem to correlate with the dissociation time, there is a noticeable signal shifting from ca. 1500 cm^{-1} towards the 2000 cm^{-1} peak at 50–100 fs before the dissociation. Additional, the standard deviation in the dissociation times is ca. 100 fs, thus indicating a significant structural change which resulted in Cl dissociation occurs at ca. 300 fs for all three pulse sequences. This also reinforces the hypothesis that for a simple, single bond dissociation channel like Cl dissociation, the process is not very susceptible to differences in the dual pulse sequence.

For HCl^+ dissociation, the C–O stretching peak at 2000 cm^{-1} always appears right after the dissociation along with the disappearance of C–H rocking peak at ca. 900 cm^{-1} and the appearance of a very broad peak centered around 400 cm^{-1}. Inspection of the trajectories shows that the latter peak can be best assigned to rotation of the HCl^+ fragment. The fact that applying the 3.5 µm pulse first enhances the C-H stretching mode and leads to a higher percentage of HCl^+ dissociation, but does not have a positive effect on the lower energy Cl dissociation, further supports our hypothesis that the C–H stretching mode needs to be activated first followed by the

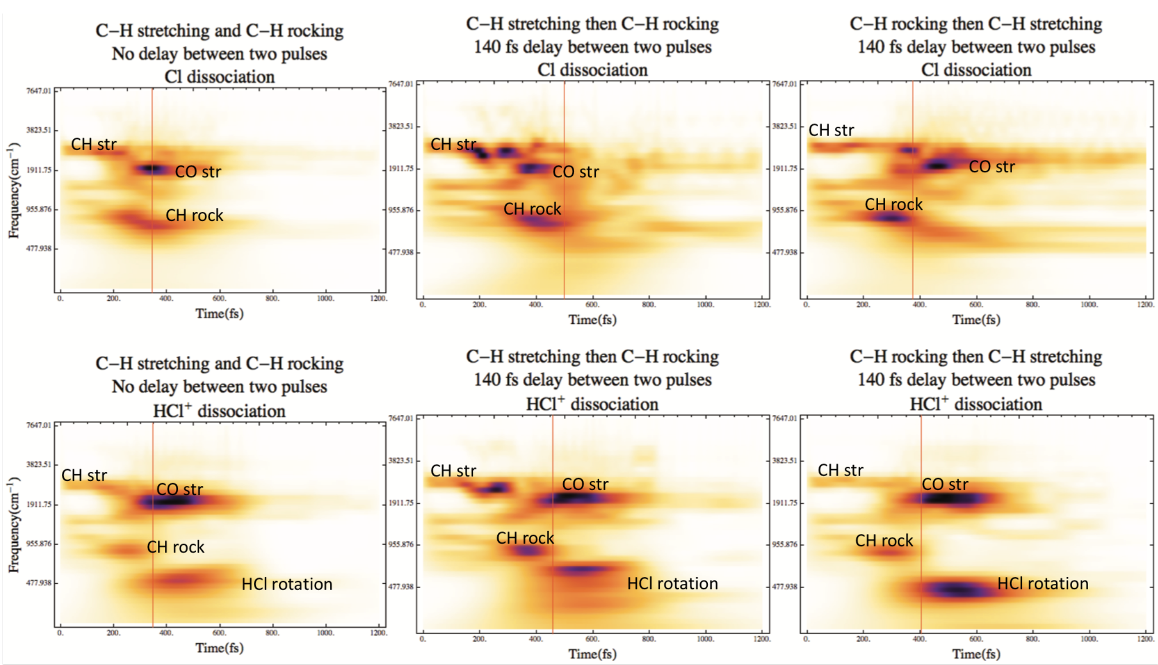

Figure **5.1**. CWT analysis scalograms with proposed peak identifications. Darker color indicates stronger signal. Vertical axis is in logarithm scale. Red vertical lines indicate average dissociation time.

activation of C–H rocking mode to facilitate the more complex movements of atoms required for HCl^+ dissociation.

5.5 Summary

In this chapter, we explored the possibility of employing two different, moderate intensity mid-IR laser pulses to enhance the yield of higher energy reaction channels. We found some interesting correlations between the branching ratios and the choice of pulse wavelength, polarization direction and delay. Simultaneously promoting the C–H stretching mode (3.5 μm pulse along C–H bond) and the C–H rocking mode (10.5 μm pulse perpendicular to C–H bond) gives the greatest number of high energy HCl^+ dissociations, even more than the previously demonstrated optimal single pulse parameters: a 7 μm pulse perpendicular to C–H bond. This effect is also shown to be strongly related to the order of which the two pulses are applied, i.e. applying the 3.5 μm pulse first gives much more HCl^+ dissociation than applying the 10.5 μm pulse first. We then used continuous wavelet transformation to identify key events of molecular vibrational mode activation (or rotational activation, in the case of HCl^+ dissociation) and their correlation with the effect that different pulse sequences have on the branching ratio and more importantly, the dissociation mechanisms.

CHAPTER 6 COMPUTATIONAL SIMULATIONS OF A "MOLECULAR PROPELLER": HYDROGEN CIRCULAR MIGRATION IN PROTONATED ACETYLENE INDUCED BY CIRCULARLY POLARIZED LIGHT

6.1 Introduction

Complex chemical transformation requires extensive rearrangement of nuclear configuration within the molecules, which are often achieved only by stochastic vibrational motions when thermally or electronically activated. Mode-selective chemistry or laser-controlled chemistry aims to achieve higher efficiency than thermal activation by selectively exciting vibration modes coupled closely to reaction coordinates. However, such effort does not always lead to desired nuclear rearrangement because energy deposited in specific vibrational modes is often dissipated within 1 – 2 ps by intramolecular vibrational redistribution (IVR).[94,95] However, if the energy can be deposited fast enough into the appropriate modes, the preferred reaction can occur before IVR becomes significant. Recently, in a computational simulation, we demonstrated that intense, ultrashort mid-infrared laser pulses can overcome IVR to achieve targeted nuclear rearrangement.[4,5,7] Here, we show that ultrafast mid-IR excitation can promote large amplitude nuclear motions, specifically, a propeller-like three-hydrogen migration around the C_2 core in protonated acetylene. Importantly, the sense of the "propeller" rotation can be directed by changing the helicity of the circularly polarized mid-IR pulses (left or right).

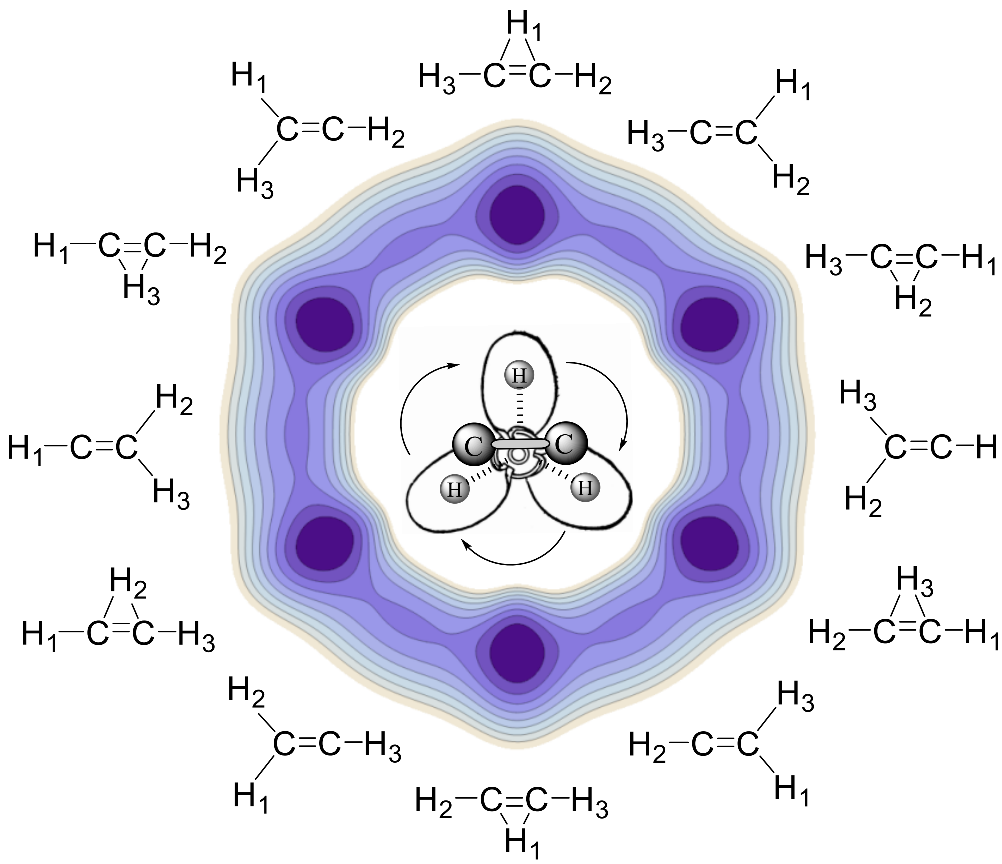

Scheme 6.1. Geometries and a representation of potential energy surface for the interchange between the T-shaped and Y-shaped structures of protonated acetylene resulting in a propeller-like motion of the hydrogens around the C_2 core.

Large amplitude motions of hydrogens have been studied in a number of small molecules such as acetylene, allene and methanol.[108-116] These 1,2 and 1,3 hydrogen migrations can be driven by short, intense 800 nm laser pulses. Isomerization occurs on the ground or excited states of the cations, and is verified by detecting the appropriate fragment ions in coincidence. In allene, H_2CCCH_2, migration is also confirmed by the detection of H_3^+.[108,112,117] Another example of large amplitude hydrogen motion is the roaming reaction channel for the dissociation of CH_2O to CO + H_2.[118-121] For reaction energies just below the C–H bond dissociation energy, a hydrogen atom can "roam" around the HCO fragment before abstracting the other hydrogen to form H_2. In each of these cases, there are large barriers for hydrogen migration on the ground state surface and the molecule must be ionized or strong bonds must be broken before large amplitude motion of the hydrogen can occur. By contrast, the hydrogens in protonated acetylene are very mobile and can circulate around the C_2 core with barriers of only a few kcal/mol. Laser fields in the mid-IR region couple strongly to vibrational motion, and should stimulate large amplitude hydrogen motion on the ground state potential energy surface at energies well below ionization or bond dissociation.

There is a long history of calculations on protonated acetylene showing that the non-classical T shaped structure, with a hydrogen bridging the two carbons, is more stable than the classical Y shaped geometry, with two hydrogens on one carbon and one hydrogen on the other carbon. Early electronic structure calculations include papers by Schaefer and co-workers,[122] Lindh et al.,[123,124] and Curtiss and Pople.[125] Subsequent experimental work confirmed that the non-classical form is the most stable structure.[126-129] Accurate quantum chemical calculations of the potential energy surface place the classical Y shaped structure 3.7 – 4.0 kcal/mol above the non-classical T shaped structure.[130,131] Recent high level calculations of the rovibrational spectrum match the experimental rotational constants to better than 0.1% and the antisymmetric HCCH stretch to within 3.0 cm^{-1}.[132] Large amplitude pseudorotational motion of the hydrogens has been seen under thermal conditions using Car-Parrinello simulations with both classical and path-integral dynamics.[128,133,134] In the present chapter we use Born-Oppenheimer ab initio classical trajectory calculations to simulate the dynamics of protonated acetylene resulting from the interaction with very short, intense mid-IR pulses of linearly and circularly polarized light.

6.2 Method

Calculations were carried out with the development version of the Gaussian series of programs[30] using the M062X[135] density functional with the 6-311+G(3df,2pd)[32,136] basis set. The choice of the functional was based on an extensive survey of ~200 functionals by comparing the energy difference between the classical (Y-shaped) and non-classical (T-shaped) structures of protonated acetylene to CCSD(T) and BD(T) calculations[130] (see Table A1 in the appendix for the functionals and energy comparisons). Classical trajectory calculations were carried out on the ground state Born-Oppenheimer surface for aligned protonated acetylene in the time varying electric field of a laser pulse. After testing various combinations of wavelengths, pulse lengths and field strengths, the laser field was chosen to be a 32 cycle 7 μm cosine squared pulse (747 fs full width). For circularly polarized light, the propagation direction was in the z-direction perpendicular to the plane of the molecule (xy plane) with the electric field rotating in the plane of the molecule with a maximum field strength of 0.03 au. For linearly polarized light, the polarization direction was in the plane of the molecule and the direction was varied from $\theta = 0^\circ$ to 360° in steps of 30° with a maximum field strength of 0.04 au. The molecular dynamics in the laser field were simulated by classical trajectory calculations which intrinsically include effects such as vibrational anharmonicity and IVR.[137,138] Trajectories were calculated with the M062X/6-311+G(3df,2pd) level of theory using the PCvelV integrator[104] with a step size of 0.25 fs and Hessian updating[105,106] for 20 steps before recalculation. Zero-point vibrational energy was added to the initial structures using orthant sampling of the momentum.[107] So that the molecule remains oriented in the laser field in order to maximize the effect of the circularly polarized light and to facilitate the analysis of the components of the angular motion of the hydrogens, no rotational energy was added to the initial structures. Trajectories were classified as either dissociating or non-dissociating based on bond lengths. Migration of hydrogen atoms was quantified by integrating the signed step-wise angular displacement of the H–(CoM)–C1 angle, projected onto xy-plane which is perpendicular to laser field propagation direction, where H is the hydrogen atom of interest, C1 is the first carbon atom, and CoM is the center of mass of the whole molecule. To help in the analysis, the kinetic energy of the hydrogens was separated into a hydrogen circular migration component as illustrated in Scheme 6.1, a C–H bond stretching component and an out-of-plane component. The kinetic energy for C–H stretching was calculated from the x and y components of the velocity parallel to the vector between the hydrogen and the nearest carbon, the kinetic energy for circular migration was calculated from x and y components of the velocity perpendicular to this vector, and the out-of-plane kinetic energy was calculated from the z component of the velocity.

6.3 Results and Discussion

As illustrated in Scheme 6.1, the circular migration of the hydrogens in $C_2H_3^+$ can proceed by a sequential, stepwise interchange between the T-shaped "non-classical" structures and the Y-shaped "classical" structure. High level quantum calculations show that the non-classical structure is favored by 3.7–4.0 kcal/mol.[130,131] However, these levels of theory are too costly for extensive molecular dynamics calculations. A survey of ~200 functionals found that the M062X/6-311+G(3df,2pd) potential energy curve is in very good agreement with accurate calculations carried out at the CCSD(T) and BD(T) levels of theory[130] (see Figure 6.1). The various channels for dissociation of protonated acetylene are shown in Scheme 6.2. Since the lowest dissociation energy is ca 100 kcal/mol, circular migration of the hydrogens can occur much more readily than dissociation.

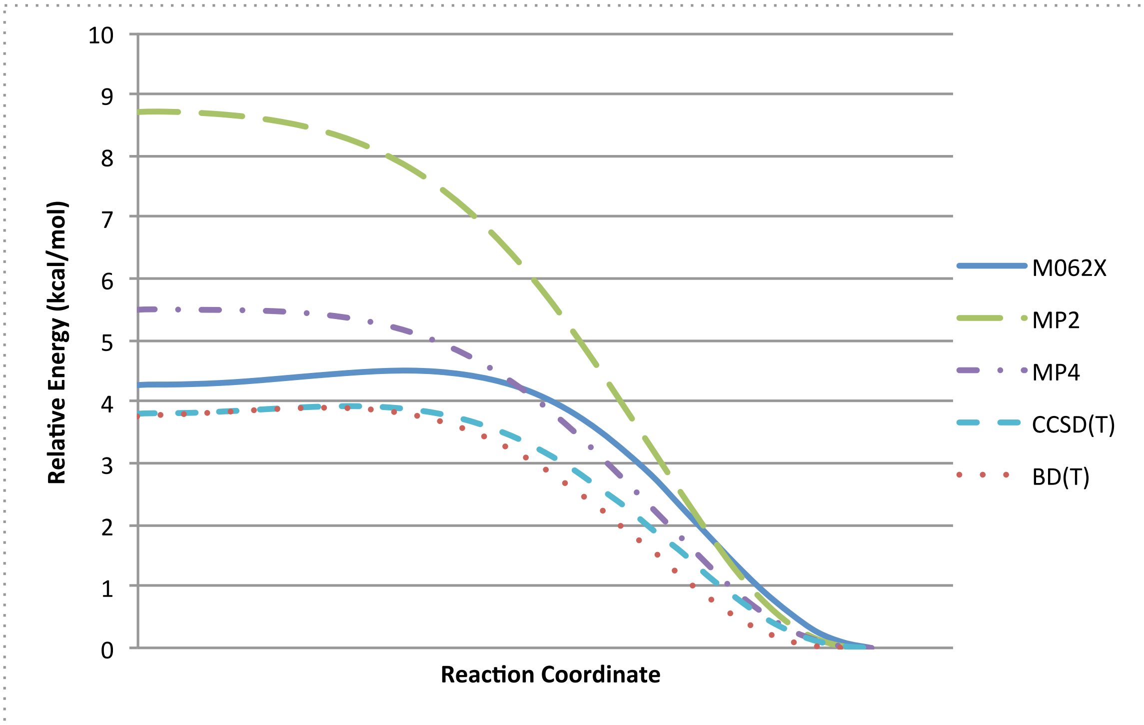

Figure 6.1. Potential energy curve for protonated acetylene computed at the M062X, MP2, MP4, CCSD(T) and BD(T) levels of theory with the 6-311+G(3df,2pd) basis set.

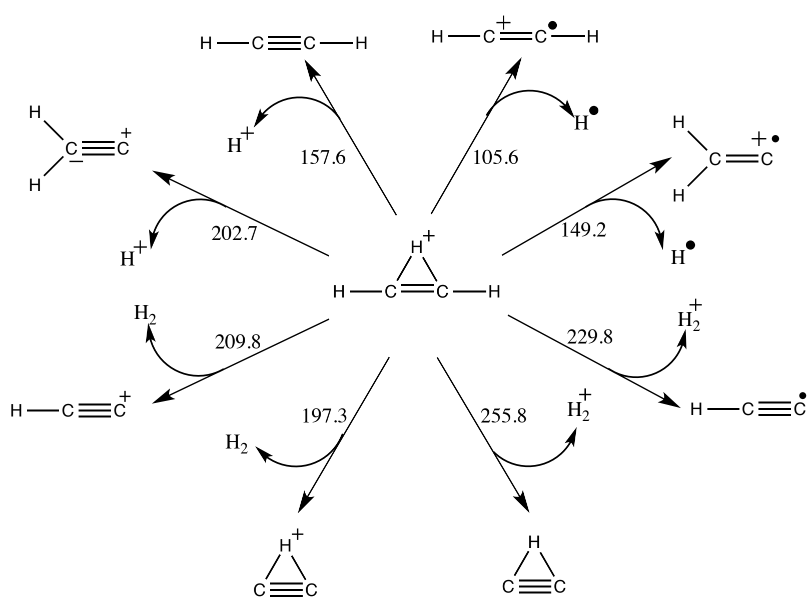

Scheme 6.2. Lowest energy dissociation channels for $C_2H_3^+$ (reaction free energies in kcal/mol at the M062X/6-311+G(3df,2pd) level of theory).

In previous studies[4,5,7,139-141], we found that ultrashort, intense 7 μm laser pulses were very effective at depositing vibration energy in a molecule. These studies also showed that for a given maximum field strength, circularly polarized mid-IR laser pulses deposits ca. 40% more energy than a linearly polarized pulse. In order to deposit comparable amount of energy into the molecule, a peak field strength of 0.03 au was used for the circularly polarized laser field and 0.04 au for the linearly polarized laser field. To determine the effect of wavelength on the response of protonated acetylene to circularly polarized light, a series of simulations was carried out with wavelengths ranging from 2 μm to 10 μm while keeping the pulse length fixed at 32 cycles. For shorter wavelengths, interaction between the laser pulse and the molecule is considerably weaker than at 7 μm. Longer wavelengths deposited increasing amounts of energy and angular momentum. However, as the wavelength increases beyond 7 μm, more trajectories dissociate. Thus 7 μm seems to be the best wavelength for the present simulations.

Table 6.1. Total energy and total angular momentum absorbed as a function of wavelength for circularly polarized light.[a]

Wavelength (μm)	Percent dissociated	Energy (kcal/mol)	Angular momentum (ħ)	
			Magnitude	Z component
2	0%	32.2±2.4	1.8±0.9	0.0±1.8
3	0%	44.6±13.8	2.7±1.6	-1.3±2.3
4	0%	74.4±39.4	8.5±5.6	-5.9±6.0
5	0%	71.9±35.9	9.7±6.1	-6.9±6.3
6	0%	64.4±30.7	8.7±6.6	-6.7±6.8
7	8%	148.6±48.9	31.5±12.2	-28.4±12.3
8	16%	120.8±58.9	28.2±16.3	-25.0±15.9
9	18%	160.5±62.2	45.0±19.9	-40.3±19.3
10	36%	176.0±52.3	58.8±19.7	-50.3±18.5

[a] Left circular cosine squared pulse with 32 cycles, 50 trajectories per wavelength.

The effects of linear and circularly polarized light are compared in Table 6.2. For right and left circularly polarized light, 400 trajectories were calculated for each helicity; for linearly polarized light, the polarization direction was rotated in the plane of the molecule in increments of 30° and 100 trajectories were calculated for each direction, for a total of 1200 trajectories. The average total energy absorbed is nearly the same for linearly and circularly polarized light at these field strengths. Similar to previous studies on $ClCHO^+$,[7] the angular momentum resulting from interaction with circularly polarized light is similar in magnitude to that from linearly polarized light. For linearly polarized light the average z-component of the angular momentum is nearly zero, but for circularly polarized light the z-component strongly favors the direction corresponding to the handedness of the circular polarization. Based on the small difference between the total magnitude and z-component of the total angular momentum vectors, the majority of the total angular momentum is along the z-axis, corresponding to rotation in the molecular plane. To determine whether the total angular momentum is indicative of a propeller-like rotation of the hydrogens requires a more detailed examination of the dynamics.

Table 6.2. Total energy and total angular momentum absorbed for 7μm linear and circularly polarized light.[a]

Polarization	Field Strength (au)	Energy (kcal/mol)	Angular momentum (ħ)	
			Magnitude	Z component
Left Circular [b]	0.03	157.0±62.6	34.0±21.7	-30.3±14.5
Right Circular [c]	0.03	158.5±77.2	33.9±20.9	30.6±18.1
Linear (0 - 360° averaged) [d]	0.04	158.4±77.7	25.0±32.2	-0.6±33.1

[a] Cosine squared shape, 7μm wavelength and 32 cycles, results are averages over non-dissociating trajectories ± one standard deviation. [b] 400 trajectories, ca. 4% dissociated; [c] 400 trajectories, ca. 3% dissociated; [d] 1200 trajectories, ca. 7% dissociated.

To study the rotational motion of the hydrogens with respect to C_2 core, it is helpful to break down the total angular momentum into contributions from individual atoms. As shown in Figure 6.2, the distribution of z-components of atomic angular momenta for the three hydrogen atoms is rather broad by the end of the simulation. The distribution for linearly polarized light is centered around zero, indicating that there is no preference in the direction of rotation. However for circularly polarized light, the distributions are displaced to either side of zero, showing that the interaction with the light results in a net rotation motion of the hydrogens in opposite directions for left and right circularly polarized light. Figure 6.2 also shows the evolution of the distribution of the angular momentum of the hydrogens with time. At the start of the simulations, the system was given zero point vibrational energy but no overall rotational energy so that it could stay aligned in the laser field. Initially, the distribution of the z-component of the angular momentum of the hydrogens is narrow and centered at zero. As time progresses, the laser field interacts with the molecule increasing the motion of the hydrogens. The distribution of the z-component of the angular momentum becomes quite broad. For linearly polarized light, the distribution remains centered around zero, but for circularly polarized light, the distribution is skewed in the positive or negative direction, depending on whether the light is right or left circularly polarized. Thus, the components of the angular momentum indicate that there is a net propeller-like motion of the hydrogens around the C_2 core.

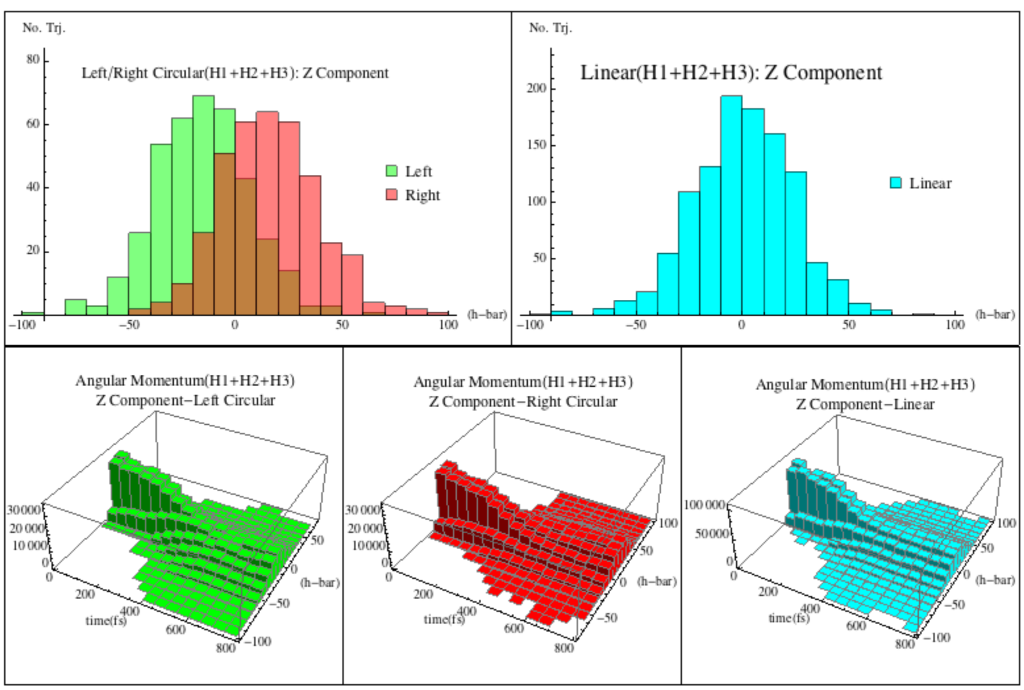

Figure 6.2. Histogram of combined (H1+H2+H3) atomic angular momentum for left and right circularly and linearly (0 - 360° averaged) polarized at the end of simulation (top row) and over simulation time (bottom row).

Another way to probe the driving force behind hydrogen circular migration is to examine the kinetic energy. As shown in Table 6.3, only about 20% of the total kinetic energy is deposited into the motion of the two carbon atoms. Because of the greater mass of carbon, the difference in kinetic energy corresponds to a significantly smaller the average velocity for the carbons than for the three hydrogens. For the hydrogens, the kinetic energy can be divided into components parallel ($T_{\parallel}$) and perpendicular ($T_{\perp}$) to the bonds between the hydrogens and the nearest carbon. The former corresponds approximately to C-H stretching motion and the latter to rotation about the C_2 core. The perpendicular component, $T_{\perp}$, can be further divided into in-plane rotation and motion out of the molecular plane. The in-plane $T_{\perp}$ component of the kinetic energy corresponding to the circular migration of the hydrogen atoms, 16 kcal/mol, is only about 10% of the total energy, but is more than sufficient to overcome the 4 kcal/mol energy difference between the T-shaped and Y-shaped structures. Interestingly, the ratios of the components of the kinetic energy are nearly the same for linearly and circularly polarized light. Thus, the difference in the behavior of the molecule in linearly and circularly polarized light is not due to any difference the amount of kinetic energy deposited in various motions, but is due to the difference in direction of the torque induced by the laser field.

Table 6.3. Atomic kinetic energy decomposition (kcal/mol).

Polarization	Field Strength (au)	T_{total}	H1+H2+H3			C1+C2
			$T_{\perp}$		$T_{\parallel}$	
			In-plane	Out-of-plane		
Left Circular [a]	0.03	72.4±31.9	15.3±19.5	6.1±3.9	33.8±10.5	17.1±7.6
Right Circular	0.03	73.6±40.0	16.8±23.5	6.1±4.1	34.3±12.3	16.4±7.8
Linear (0 - 360° averaged)	0.04	71.7±36.4	16.1±20.3	6.6±5.5	32.5±10.6	16.4±7.8

[a] see footnotes of Table 2 for trajectory details

The most direct measurement of a propeller-like hydrogen motion is simply the cumulative angular displacement of the three hydrogen atoms within the molecular plane, as measured by the change in the angle of the hydrogen with respect to the C_2 core, summed over the time steps. Since the starting geometry was chosen to be the more stable T-shaped structure with H1 as the bridging atom, there should be some difference between the initial motion of bridging hydrogen and the terminal hydrogens. Given sufficient time, all three hydrogen atoms are expected to interchange their locations, and since they are in principle indistinguishable, the sum of their individual angular displacement is a better way to monitor the rotational motion. For circularly polarized light the average displacement per hydrogen in 800 fs is about half of a full cycle, and on average motion the hydrogens move in opposite directions for left and right circularly polarized light (Table 6.4 and Figure A1.). By comparison, the average angular displacement of the hydrogens with linearly polarized light is small. For both linearly and circularly polarized light, the standard deviations are very large, indicating a wide range of magnitudes and directions for the angular displacements.

Table 6.4. Average cumulative angular displacement in the xy plane after 800 fs (in degrees)

Polarization	Field Strength (au)	H1	H2	H3	H1+H2+H3
Left Circular [a]	0.03	183.2±386.0	-208.1±410.2	-141.7±409.5	-533.0±953.5
Right Circular	0.03	158.4±425.1	150.3±408.0	198.0±429.3	506.7±1052.1
Linear (0 - 360° averaged)	0.04	13.2±448.3	-3.4±436.2	29.9±442.5	39.7±1104.6

[a] see footnotes of Table 1 for trajectory details, displacements are averages over non-dissociating trajectories ± one standard deviation

To examine the behavior of protonated acetylene at longer times, two set of 100 trajectories were integrated for 3.2 ps for circularly polarized light (see Figure 6.3). The average of the z-components of the angular momentum for the hydrogens is opposite in sign for right and left circularly polarized light. It starts to increase rapidly near the peak of the pulse, continues to rise during the second half of the laser pulse (375 to 750 fs), and remains nearly constant after the pulse. On average the hydrogens move in the xy plane with a standard deviation ca 35° for the out-of-plane angle (see Figure A2). For the in-plane motion, the cumulative angular displacement of the hydrogens relative to the C_2 core starts to increase near the pulse maximum and continues to increase linearly after pulse, as expected from the z-component of the angular momentum. The standard deviation for the displacements also continues to grow nearly linearly with time after the end of the pulse. This indicates that net circulation of the hydrogens is composed of a range of rotational directions and velocities, and that this motion continues after the pulse. The fact that the z-component of the angular momentum of the hydrogens does not decrease toward zero in the 2.4 ps after the pulse (corresponding, that the angular displacement does not slow down), suggests that the circulatory motion of the hydrogens may be weakly coupled to the other vibrational modes and that IVR is somewhat slower for this motion.

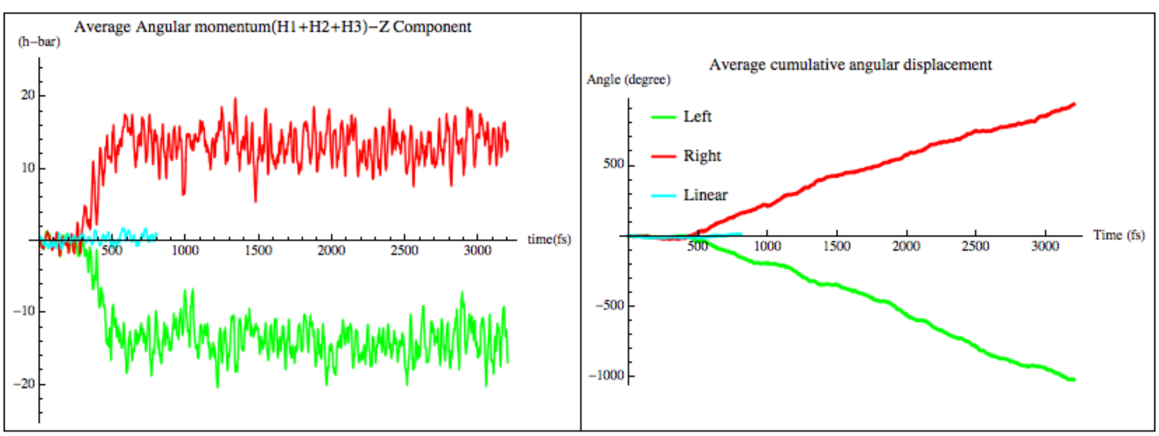

Figure 6.3. Average combined hydrogen atomic angular momentum z component and cumulative average angular displacements as a function of time for non-dissociating trajectories (linear: 1200 trajectories, ca. 7% dissociated, 800 fs simulation time; left circular: 100 trajectories, ca. 15% dissociated, 3200 fs simulation time; right circular: 100 trajectories, ca. 17% dissociated, 3200 fs simulation time).

6.4 Summary

In the present chapter, we have examined the possibility of circularly polarized light inducing propeller-like motion of hydrogen migration in $C_2H_3^+$. Circularly polarized light with a peak field strength of 0.03 au is as effective as linearly polarized light with a peak field strength 0.04 au in depositing kinetic energy and angular momentum for the hydrogens. For circularly polarized light, the sign of the z-component of the average angular momentum of the hydrogens depends on the handedness of the circular polarization. By comparison, the z-component of the average angular momentum is near zero for linearly polarized light. Circularly polarized light produces an appreciable amount of angular displacement of the three hydrogen atoms, corresponding to a propeller-like motion of the hydrogens around the C_2 core. By contrast, the cumulative angular displacement for linearly polarized light was very small. The total energy and kinetic energy absorbed are similar for right and left circularly polarized light, but the angular momentum vectors and cumulative angular displacement have opposite directions depending on the laser polarization handedness. Although the cumulative angular displacement is only about half of a cycle by the end of the pulse, the propeller-like motion of the hydrogens continues for a few ps after the laser pulse.

6.5 *Appendix*

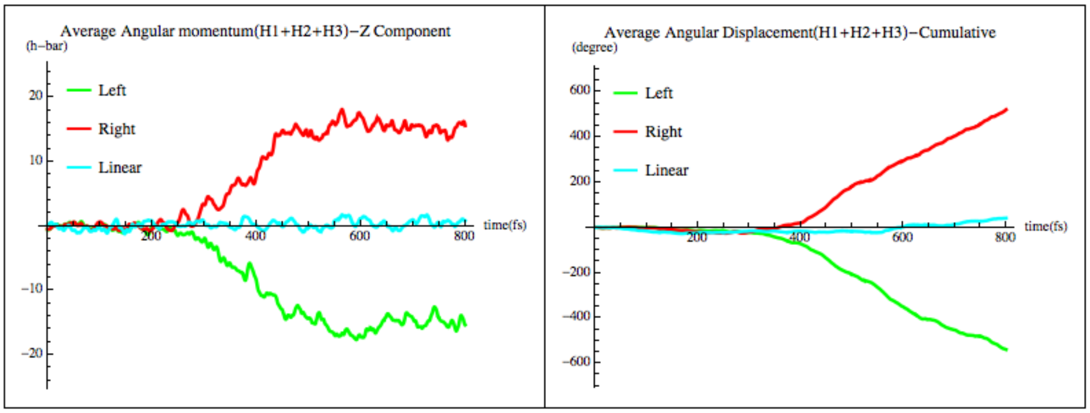

Figure A1. Average combined hydrogen atomic angular momentum z component and cumulative average angular displacement over time for the trajectories in Table 6.4.

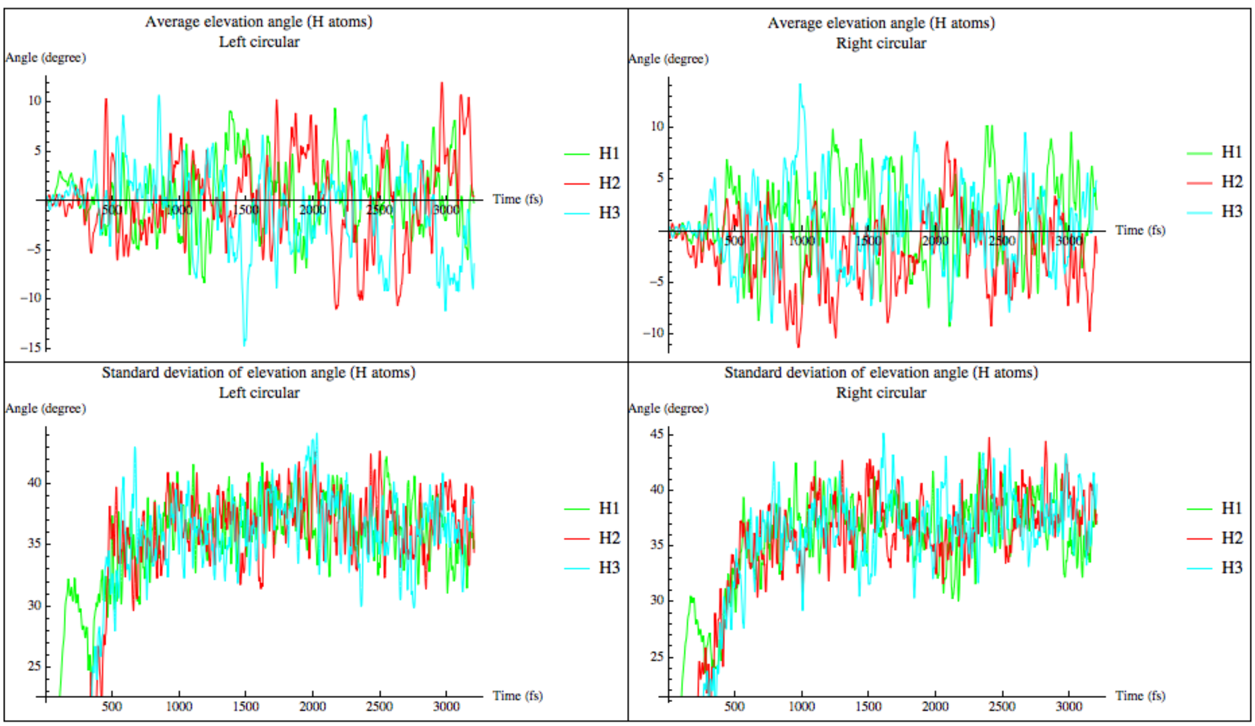

Figure A2. Average out of plane angle for the hydrogens and standard deviations over time.

Table A1. Density functional benchmark on the energy difference between classical and non-classical $C_2H_3^+$ structures

Functional	Energy difference (kcal/mol)	Functional	Energy difference (kcal/mol)	Functional	Energy difference (kcal/mol)	Functional	Energy difference (kcal/mol)
SVWN	4.351696282	mPWP86	1.480663107	TPSSTPSS	0.622875856	PBEhVP86	1.65314699
SVWN5	4.257968167	mPWPW91	1.626805104	TPSSKCIS	0.827012935	PBEhV5LYP	-0.299133692
SLYP	5.16698263	mPWB95	2.415986699	TPSSBRC	-1.127524122	HFS	3.514939669
SPL	4.236749153	mPWPBE	1.807839783	TPSSPKZB	0.355164439	XAlpha	3.971547184
SP86	0.003230134	mPWTPSS	1.974594061	TPSSVP86	0.095895134	HFB	-2.310249934
SPW91	1.011424019	mPWKCIS	2.147863704	TPSSV5LYP	-1.956588051	VSXC	1.252885981
SB95	0.007552312	mPWBRC	0.304243888	BRxVWN	-1.656267123	HCTH	2.293859116
SPBE	3.41393164	mPWPKZB	1.737508556	BRxVWN5	-1.734275472	HCTH93	1.695417726
STPSS	0.014569867	mPWVP86	1.497926593	BRxLYP	-0.51082321	HCTH147	1.521064762
SKCIS	0.032812697	mPWV5LYP	-0.44933601	BRxPL	-1.747450149	HCTH407	2.293859116
SBRC	5.917201685	G96VWN	-1.480195178	BRxP86	1.45133895	tHCTH	0.939522466
SPKZB	0.006351711	G96VWN5	-1.555704936	BRxPW91	1.59719123	M06L	2.394769066
SVP86	0.014980756	G96LYP	-0.348964898	BRxB95	2.425540244	B97D	0.645816801
SV5LYP	5.16698263	G96PL	-1.569337564	BRxPBE	1.782175286	B97D3	0.151277043
XAVWN	4.829271183	G96P86	1.580758997	BRxTPSS	1.948724372	SOGGA11	1.090052341
XAVWN5	4.734137649	G96PW91	1.72497205	BRxKCIS	2.11973105	M11L	0.74828848
XALYP	5.655606478	G96B95	2.524229775	BRxBRC	0.326924043	N12	0.641495062
XAPL	4.711049555	G96PBE	1.906596079	BRxPKZB	1.70810044	MN12L	0.480368293
XAP86	0.041087641	G96TPSS	2.075857483	BRxVP86	1.468197132	B3LYP	0.29162085
XAPW91	0.067358557	G96KCIS	2.253090999	BRxV5LYP	-0.51082321	B3P86	2.024710153
XAB95	0.056855976	G96BRC	1866.539804	PKZBVWN	-1.374671889	B3PW91	2.044226438
XAPBE	0.057430267	G96PKZB	1.836638531	PKZBVWN5	-1.45319661	B1B95	3.349532702
XATPSS	0.059604753	G96VP86	1.597783404	PKZBLYP	-0.223941451	mPW1PW91	2.327908684
XAKCIS	0.010299332	G96V5LYP	-0.348964898	PKZBPL	-1.46612882	mPW1LYP	0.113884264
XABRC	6.59224927	PBEVWN	-1.194892217	PKZBP86	1.775543835	mPW1PBE	2.523238759
XAPKZB	0.068771003	PBEVWN5	-1.274005599	PKZBPW91	1.925061484	mPW3PBE	2.255969858
XAVP86	0.005855795	PBELYP	-0.097112553	PKZBB95	2.785823978	B98	0.517560898
XAV5LYP	5.655606478	PBEPL	-1.288518111	PKZBPBE	2.111517663	B971	0.84462387
BVWN	-1.648959537	PBEP86	1.828321669	PKZBTPSS	2.284612483	B972	1.871330473
BVWN5	-1.725695687	PBEPW91	1.978949685	PKZBKCIS	2.464691537	PBE1PBE	2.818159208
BLYP	-0.522229143	PBEB95	2.754144552	PKZBBRC	0.554336903	B1LYP	0.04883197
BPL	-1.73932411	PBEPBE	2.15863542	PKZBPKZB	2.04101814	O3LYP	1.880607603
BP86	1.41343915	PBETPSS	2.321788208	PKZBVP86	1.792005121	BHandH	3.774589429
BPW91	1.559413855	PBEKCIS	2.492710236	PKZBV5LYP	-0.223941451	BHandHLYP	0.177312832
BB95	2.356852197	PBEBRC	0.655756887	wPBEhVWN	-1.405567689	BMK	1.658017856
BPBE	1.741170036	PBEPKZB	2.088512399	wPBEhVWN5	-1.484662936	M06	1.951007102
BTPSS	1.909514658	PBEVP86	1.846401536	wPBEhLYP	-0.299133692	M06HF	5.041469417

BKCIS	2.085427908	PBEV5LYP	-0.097112553	wPBEhPL	-1.499221194	M062X	4.454601252
BBRC	17319.1491	OVWN	0.594314931	wPBEhP86	1.635427686	tHCTHhyb	0.835295849
BPKZB	1.670673839	OVWN5	0.508883221	wPBEhPW91	1.78647889	APFD	2.501574657
BVP86	1.430596148	OLYP	1.691452283	wPBEhB95	2.571222596	APF	2.500446282
BV5LYP	-0.522229143	OPL	0.492685235	wPBEhPBE	1.967186765	SOGGA11X	2.54480541
PW91VWN	-1.361860474	OP86	3.687484671	wPBEhTPSS	2.132320517	PBEh1PBE	2.656608372
PW91VWN5	-1.439793209	OPW91	3.847213237	wPBEhKCIS	2.306943558	TPSSh	1.03928716
PW91LYP	-0.257628196	OB95	4.660817563	wPBEhBRC	0.464580443	X3LYP	0.397294928
PW91PL	-1.454199046	OPBE	4.029813724	wPBEhPKZB	1.896807158	HSEH1PBE	2.570010574
PW91P86	1.663848614	OTPSS	4.195325107	wPBEhVP86	1.65314699	OHSE2PBE	2.498073693
PW91PW91	1.811179542	OKCIS	4.378376329	wPBEhV5LYP	-0.299133692	OHSE1PBE	2.571814331
PW91B95	2.588014451	OBRC	2.461341989	PBEhVWN	-1.405567689	wB97XD	1.755650484
PW91PBE	1.991068776	OPKZB	3.960240584	PBEhVWN5	-1.484662936	wB97	3.067465271
PW91TPSS	2.155293088	OVP86	3.707091127	PBEhLYP	-0.299133692	wB97X	2.342779313
PW91KCIS	2.325625452	OV5LYP	1.691452283	PBEhPL	-1.499221194	LC-wPBE	4.124275892
PW91BRC	3303.064185	TPSSVWN	-3.186115986	PBEhP86	1.635427686	CAM-B3LYP	1.370880829
PW91PKZB	1.92109987	TPSSVWN5	-3.261525782	PBEhPW91	1.78647889	HISSbPBE	2.761626521
PW91VP86	1.68129301	TPSSLYP	-1.956588051	PBEhB95	2.571222596	M11	3.810753556
PW91V5LYP	-0.257628196	TPSSPL	-3.273181274	PBEhPBE	1.967186765	N12SX	1.390161926
mPWVWN	-1.567369463	TPSSP86	0.080388154	PBEhTPSS	2.132320517		
mPWVWN5	-1.644594877	TPSSPW91	0.227055874	PBEhKCIS	2.306943558		
mPWLYP	-0.44933601	TPSSB95	1.162459222	PBEhBRC	0.464580443		
mPWPL	-1.658569934	TPSSPBE	0.420404043	PBEhPKZB	1.896807221		

CHAPTER 7 UNPHYSICAL CHARGE OSCILLATION PROBLEM WITH BORN-OPPENHEIMER MOLECULAR DYNAMICS IN HIGH INTENSITY LASER FIELD AND A VIABLE WORKAROUND BY USING ATOM-CENTERED DENSITY MATRIX PROPAGATION METHOD

7.1 Introduction

In previous chapters, Born-Oppenheimer Molecular Dynamics (BOMD) has been used to study various chemical processes with intense mid-IR laser pulses. In past studies (refs.), as well as these chapters, BOMD gave relatively reliable descriptions of the problems of interest. In the Born-Oppenheimer approximation, the wavefunction of the system is converged at each time step to provide the force for integrating the classical equations of motion. However, this can result in an artifact manifested for a few trajectories as anomalously large charge oscillations for H atoms (H^+/$H^\bullet$/H^-) that are well-separated (beyond ca. 3 Å) from the rest of the molecule. Consequently, these trajectories absorb anomalously large amounts of energy.

An alternative to the BOMD method for calculating classical trajectories is the Atom-centered Density Matrix Propagation (ADMP) method, developed by H. B. Schlegel et al., where instead of using converged electronic structures, density matrix coefficients are given a fictitious mass and propagated using extended Lagrangian dynamics. It has been demonstrated that ADMP is as accurate as BOMD for field-free systems. Since wavefunction is not converged at each time step, the artifactual charge oscillation problem does not arise in ADMP dynamics.

7.2 Method

Calculations were carried out with the development version of the Gaussian series of programs using the B3LYP density functional with the 6-31+G(d,p) basis set. Classical trajectory calculations were carried out on the ground state surface for aligned $ClCHO^+$ in the time varying electric field of a laser pulse. The laser field was chosen to be a linearly polarized 4 cycle 7 μm cosine squared pulse (93 fs full width) along C–H bond to maximize charge oscillation on H atom with a maximum field strength of 0.09 au. The molecular dynamics in the laser field were simulated by classical trajectory calculations which intrinsically include effects such as vibrational anharmonicity and IVR.[137,138] Born-Oppenheimer Molecular Dynamics (BOMD) trajectories were calculated using the PCvelV integrator[104] with a step size of 0.25 fs and Hessian updating[105,106] for 20 steps before recalculation. Atom-centered Density Matrix Propagation (ADMP) trajectories were calculated with various fictitious electron masses and a step size of either 0.05 fs (for electron mass of 100 au or lower) or 0.1 fs (for electron mass higher than 100 au). Zero-point vibrational energy was added to the initial structures using orthant sampling of the momentum.[107]

7.3 Charge oscillation problem

When applying an intense laser field along highly polarizable bond in a system, vibrational energy increases rapidly and thus resulting a very fast dissociation. Shown in Figure 7.1 is an example of a BOMD trajectory where a 7μm 4-cycle trapezoid-shaped laser pulse with field strength 0.09 au is applied along the C–H bond of $ClCHO^+$ cation. At ca. 50 fs, when laser pulse reaches peak intensity, the C–H bond length starts to increase rapidly accompanied by strong energy oscillations. Around 80 fs, when C–H distance is already far beyond bond-breaking (ca. 3 Å), the charge oscillation on H atom begins to display abnormal behavior - sudden and large change between time steps. After the laser pulse, this problem persists: frequent sudden changes of more than 1 unit of charge between time steps as well as sudden total energy jumps of ca. 100–500 kcal/mol. These changes are not physical because a) H and C atoms are more than 50 Å apart and an electron cannot move so far in so little time; and b) total energy should be conserved after the laser pulse.

Until now the solution to this problem has been to simply discard any trajectories having such unphysical behavior. 10%–40% of the trajectories may have to be discarded because of this problem for laser intensities as high as shown in Figure 7.1. Although the remaining trajectories are enough to maintain statistical significance, the fact that the problem is mostly found in fast C–H bond breaking, biases the branching ratios toward non-H dissociation channels. This is an undesirable complication when analyzing these BOMD trajectories.

7.4 Comparison of ADMP with BOMD

Initial studies with ADMP showed the results were in good agreement with BOMD for dynamics of field-free systems when the fictitious mass and step size were chosen appropriately. Typical parameters are 1000 au for the mass and 0.25 fs for the step size. For strong field simulations, these interrelated parameters need to be tuned carefully. The choice of electron mass determines the rate at which density matrix can response to the oscillating laser field. If the step size is not sufficiently small, the integration numerical error becomes too large for the density matrix propagation.

Because of the chaotic nature of the trajectories, dynamics with BOMD cannot be reproduced exactly by ADMP given the same initial condition. A tiny difference in the molecular behavior early on will grow exponentially, leading to very different outcomes for individual trajectories. Nevertheless, the overall statistical analysis of energy absorption and branching ratios calculated by ADMP still yields a reasonable match with the set of BOMD trajectories that do not have a charge oscillation problem. As shown in Table 7.1, the ADMP trajectories with a fictitious electron mass of 40–100 au absorbed on average 5–10 kcal/mol more energy than the BOMD trajectories. Figure 7.2 shows that the distribution of total energy gained with ADMP becomes quite similar to the BOMD distribution when the fictitious electron mass is reduced to 50–100 au, but has significant high energy contributions for larger fictitious masses.

Table 7.1. Energy gain for ADMP trajectories with different fictitious electron masses compared with a BOMD example set that did not have charge oscillation problem.

method	electron mass (au)	total energy gain (kcal/mol) [b]
BOMD[a]	N/A	39.15±14.96
ADMP[a]	40 [c]	44.70±27.59
	50 [c]	49.51±37.07
	60 [c]	48.51±36.50
	70 [c]	48.59±34.70
	80 [c]	46.64±26.65
	90 [c]	44.84±25.01
	100 [c]	46.12±27.33
	200 [d]	53.70±30.50
	300 [d]	58.05±35.29
	400 [d]	61.22±39.61
	500 [d]	73.40±51.48
	600 [d]	75.67±55.96
	700 [d]	76.26±50.25
	800 [d]	74.57±36.53
	900 [d]	80.87±44.61
	1000 [d]	82.92±46.22

[a] There are 50 trajectories in each set, and the initial sampling parameters were repeated for ADMP sets. [b] Average value plus minus one standard deviation. [c] A step size of 0.05 fs is used to achieve satisfying numerical accuracy in the trajectory integration. [d] A step size of 0.1 fs is used to achieve satisfying numerical accuracy in the trajectory integration.

Having established that ADMP with fictitious electron mass of 50–100 au and a step size of 0.05 to 0.10 fs gives reasonable agreement with BOMD method, we looked at a set of BOMD trajectories that suffered extensively from the charge oscillation problems like the sample trajectory shown in Figure 7.1 and compare them with ADMP trajectories with the same initial sampling parameters. The problem with Mulliken charge oscillation is completely resolved by using ADMP (Figure 7.3). As expected, in the first two laser cycles the charge oscillation is almost identical between BOMD and ADMP. The differences start around 80 fs (Figure 7.1) where C–H

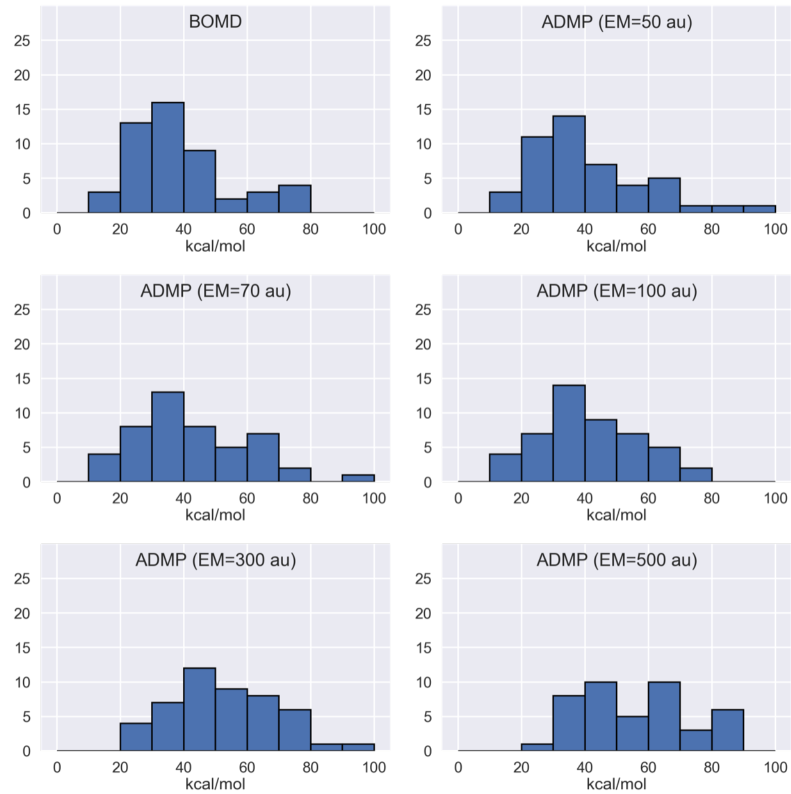

Figure 7.2. Histogram plots of energy gain for trajectories of BOMD and ADMP with different fictitious electron masses.

distance begins to increase rapidly. Throughout the entire simulation, there were no sudden charge jump between extreme charge distributions (e.g. $H^{-}\leftrightarrow H^{+}$). ADMP trajectories gained considerably less energy (ca. 80 kcal/mol) over the laser pulse than BOMD trajectories (Table 7.2). This indicates that part of the anomalously large energy gain was due to the artifactual charge oscillation. Nevertheless, the average energy gains for ADMP trajectories are still quite large. Additional work is needed to determine the other factors r the large energy gains.

Table 7.2. energy gain for trajectories of ADMP method with different fictitious electron masses compared with a BOMD example set that had charge oscillation problem.

method	electron mass (au)	total energy gain (kcal/mol) [b]
BOMD[a]	N/A	503.73±280.06
	50	423.07±272.25
ADMP	70	427.65±283.89
	100	421.89±312.59

[a] There are 50 trajectories in each set, and the initial sampling parameters were repeated for each set. [b] Average value plus minus one standard deviation.

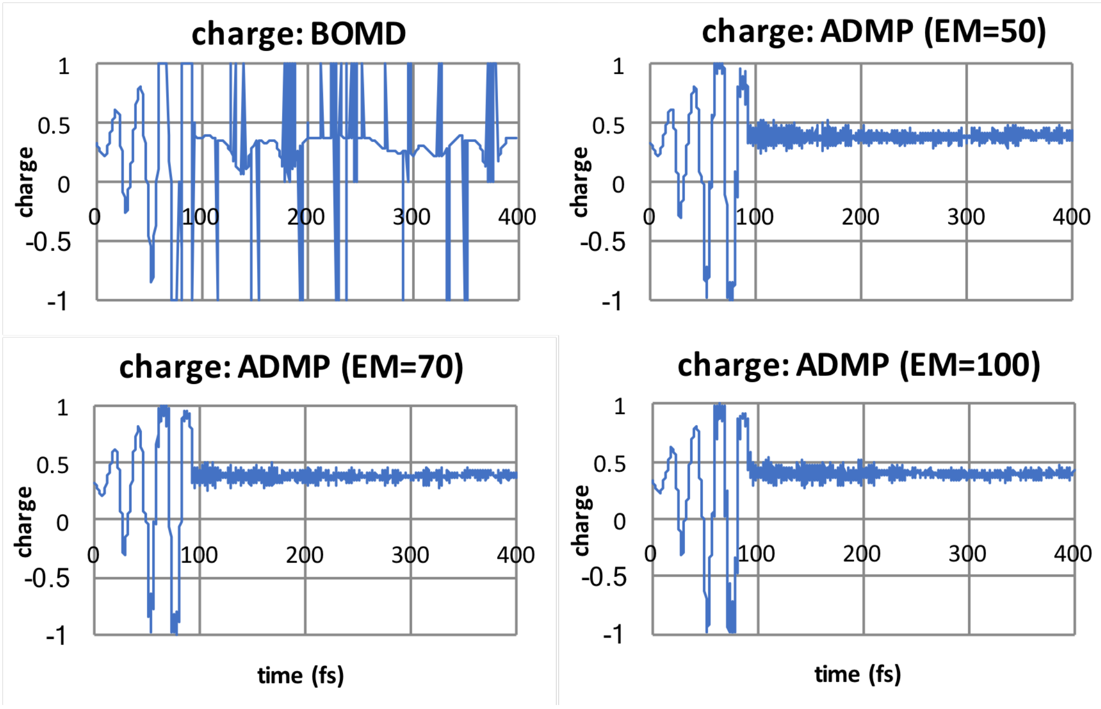

Figure 7.3. Example trajectory comparison of Mulliken charge on H atom for BOMD with ADMP. This is the same trajectory used in Figure 7.1. All the ADMP trajectories investigated behave like the example shown here.

7.5 Conclusion

In this chapter, we illustrated an inherent problem of the BOMD method where the charge on an H atom oscillates too fast because the electronic structure is converged at each step. We found that the charge oscillation problem can be overcome by propagating the density using ADMP dynamics. The parameters for the ADMP method need to be tuned for dynamics in strong laser fields. ADMP with a fictitious electron mass of 100 au and a step size of 0.05 fs can maintain reasonably good agreement with BOMD while solving the extremely fast charge oscillation problem.

CHAPTER 8 INTERPRETATION OF TWO-ELECTRON ANGULAR STREAKING EXPERIMENTS FOR METHANE MOLECULE BY TIME-DEPENDENT CONFIGURATION INTERACTION AND BORN-OPPENHEIMER MOLECULAR DYNAMICS SIMULATIONS

8.1 Introduction

The two-electron angular streaking experiments have been performed on methane molecule by Prof. Wen Li's group. These experiments measured the relative ejection angle between the two electrons that were sequentially ionized from neutral methane molecule. Since the circularly polarized laser pulse was used in the experiment, this angle is correlated with the time delay between the two ionization events. Therefore, the peaks in two-electron ejection angle signals can be traced back to unique events in the dynamics of methane molecule after the first ionization. In this chapter, we attempt to lay down some computational ground work upon which future study could be built. We begin by the simulations of the first and second ionization processes with Time-Dependent Configuration Interaction with a Complex Absorbing Potential method (TDCI-CAP).

8.2 Method

The angular dependence of ionization of was simulated by time dependent configuration interaction calculations with a complex absorbing potential.[98-101]

$$i\frac{\partial}{\partial t}\Psi_{el}(t) = [\hat{\mathbf{H}}_{el} - \hat{\vec{\mu}}\cdot\vec{E}(t) - i\hat{\mathbf{V}}^{absorb}]\Psi_{el}(t) \qquad \Psi_{el}(t) = \sum_{i=0} C_i(t)\left|\Psi_i\right\rangle \qquad (1)$$

where $\hat{\mathbf{H}}_{el}$ is the field-free electronic Hamiltonian. The electron-light interaction is treated in the semi-classical dipole approximation, where $\hat{\vec{\mu}}$ is the dipole operator and $\vec{E}$ is electric field component of the laser pulse. The absorbing potential used to model ionization, $-i\hat{\mathbf{V}}^{absorb}$ is constructed from a set of overlapping spherical potentials around each atom. Each spherical potential has a quadratic rise starting at 3.5 times the van der Waals radius R_{vdw} and a quadratic turn-over to constant value of 10 hartree at approximately R_{vdw} + 7 Å. The time-dependent wavefunction is constructed from the field-free Hartree-Fock ground state and all singly excited configurations. The computations employed the aug-cc-pVTZ basis set[102,103] plus a large set of diffuse functions, for a total of 249 basis functions and 1359 singly excited states. The time-dependent coefficients were propagated using a Trotter factorization of the exponential of the Hamiltonian. A static electric field with various field strength was used for the simulation of the ionization. The ionization yield was taken as the loss of norm of the wavefunction and was plotted as a function of the polarization direction of the pulse. Details of the procedure and validation of the methodology are described in a series of earlier papers[98-101].

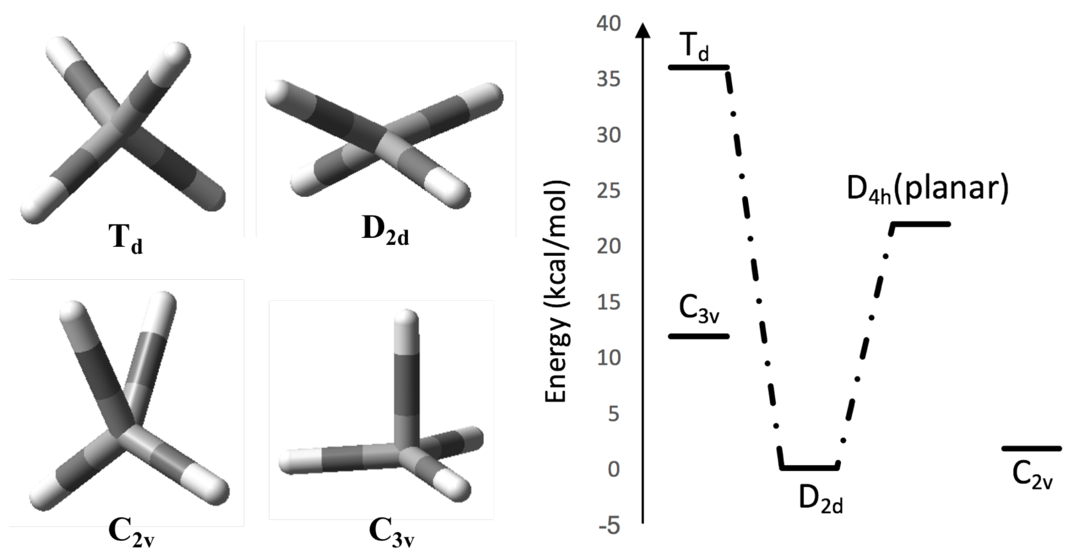

Figure 8.1. Stable/meta-stable model structures and their corresponding relative energy levels for methane cation.

Structural relaxation was simulated by classical trajectory calculations on the ground state Born-Oppenheimer surface for aligned methane cations in the time varying electric field of laser pulse. Trajectories were integrated for a total of 100 fs. The B3LYP/6-31G(d,p) level of theory is a suitable compromise between accuracy of the potential energy surface and efficiency in the trajectory calculations. Molecular dynamics calculations were carried out with the development version of the Gaussian series of programs[30] and the PCvelV integrator[104] with a step size of 0.25 fs and Hessian updating[105,106] for 20 steps before recalculation. The starting structures had no rotational energy; zero-point vibrational energy was added to the initial structures using orthant sampling of the momentum[107]. Classification of the structures into several stable/meta-stable model structures (Figure 8.1) at each time step along each trajectory is performed with an implementation of logistic regression algorithm drawing inspiration from machine learning concepts. In this implementation, the four bond lengths and six bond angles of methane cation for training sets trajectories are used to calculate various standard deviation and average values of smaller subsets according to the patterns of these bond lengths and angles observed for the stable/meta-stable model structures and then feed into the logistic regression model to optimize individual support vector machine (SVM)[142] classifiers for each model structure. These training sets are produced by carrying out the same sampling scheme as used in the BOMD calculations from the model structures, aiming to break the symmetries of these model structures while maintaining geometrical similarities to them. The classifiers are then used to classify the geometries along BOMD trajectories according to the One-vs-All algorithm.[143]

8.3 First and second ionization of methane molecule

Although a circularly polarized laser pulse was used in the angular streaking experiments, due to the extremely short time frame (less than 1 fs), the event of the first ionization most likely takes place within a fraction of one laser cycle, thus it will be more closely modeled by the interaction with an instantaneous static electric field. The first ionization of methane molecule was studied previously by P. Krause et al. using the same TDCI-CAP method but with a seven cycle linearly polarized 800 nm cosine squared pulse. The results showed that for all the peak intensities considered, the ionization angular dependence is a near-isotropic sphere due to the triply degenerate Highest Occupied Molecular Orbitals (HOMOs).

First we need to examine the effect of static field on the HOMOs of both methane molecule and methane cation (Figure 8.2 and Figure 8.3). In the case of methane molecule, aligning the static field in the two crucial directions, i.e. H–C–H angle bisector and C–H bond, gives two entirely different types of orbital splitting. In the former case, the triply degenerate HOMOs split into three non-degenerate orbitals with nearly equal separations; while in the latter case, the triply degenerate HOMOs split into one lower energy non-degenerate orbital and one set of doubly degenerate HOMOs. For methane cation, the splitting patterns with static field aligned along the two directions are in less contrast than the neutral methane case, but the highest energy SOMO(s) is still different for one direction from the other. To further complicate the matter, the ground state of methane cation with the T_d structure of neutral molecule, i.e. vertical ionization without structural relaxation, is triply degenerate due to its high symmetry.

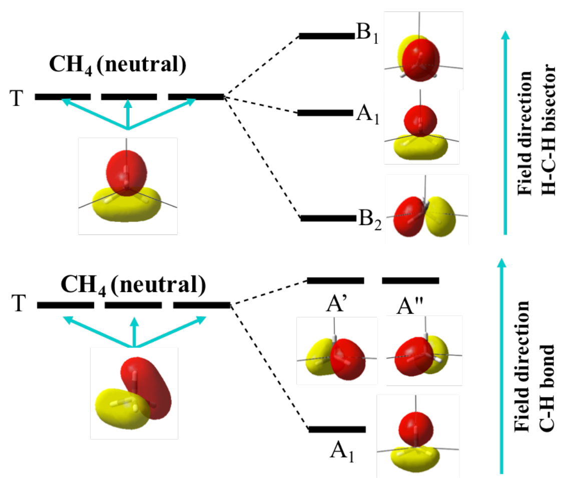

Figure 8.2. HOMO splitting scheme for methane molecule with electric field along H–C–H angle bisector (top) and along C–H bond (bottom). The orbital levels of field-free case are on the left, and the orbital levels of static field case are on the right.

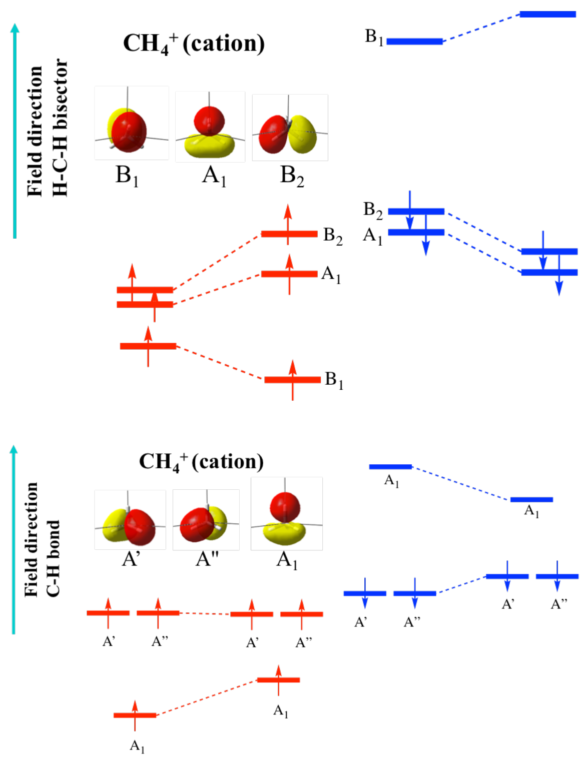

Figure 8.3. HOMO splitting scheme for methane cation with electric field along H–C–H angle bisector (top) and along C–H bond (bottom). The orbital levels of field-free case are in the middle, and the orbital levels of static field case are on the left (alpha orbitals, in red) and right (beta orbitals, in blue). The field-free energy levels in top and bottom panels are different due to a small perturbation applied to the bond length (ca. 0.001 Å) in order to collapse the triply degenerate cation ground states into roughly the same orbital shapes as each of the static field cases.

Therefore, although TDCI-CAP method can account for most of the effects of a static field on a set of degenerate HOMOs for a non-degenerate ground state by interacting degenerate, singly excited determinants with the electric field, it cannot account for the effect of electric field on degenerate ground states since such degeneracy in the ground state makes the problem

Field strength (a.u.)	Ionization rate range (Min-Max)	Norm
0.04	0.0009-0.0010	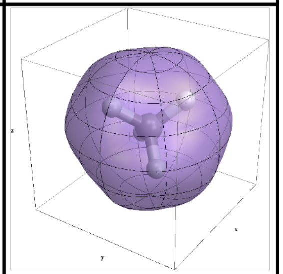
0.06	0.0592-0.0975	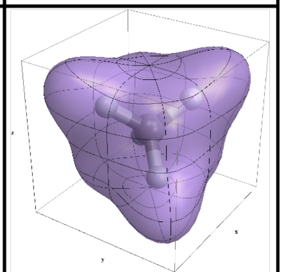
0.07	0.1422-0.4349	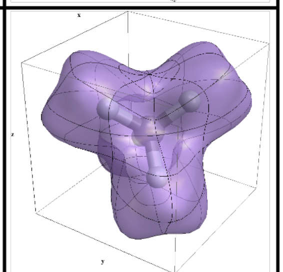
0.08	0.4989-0.8368	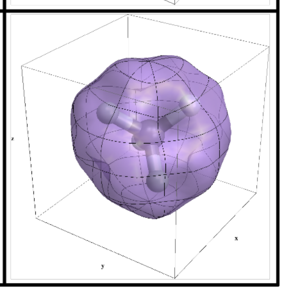

Figure 8.4. Ionization dependence of neutral methane molecule.

Field strength (a.u.)	Ionization rate range (Min-Max)	Norm
0.09	0.0146-0.0720	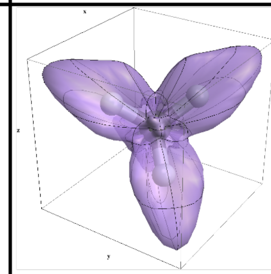
0.10	0.0602-0.2781	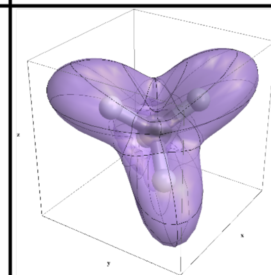
0.11	0.3469-0.6460	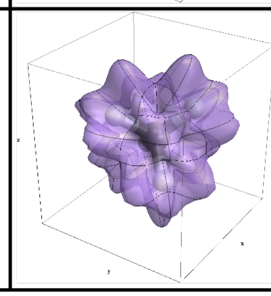

Figure 8.5. Ionization dependence of methane cation with neutral species geometry.

inherently multi-reference, therefore cannot be treated by singly excited CI. Fortunately, the degeneracy in the cation ground state for methane is a result of its high symmetry (T_d), and therefore can be treated (in part) by making use of this high symmetry. To make use of this symmetry, we place the carbon at the center of a cube and the hydrogens at four of the eight vertices of the cube. Ionization rates for methane neutral and cation are calculated only for one face of the cube on a 5×5 grid. Symmetry operations from the T_d point group are then used to generate the data for the other faces of the cube. The results are summarized in Figure 8.4 (neutral methane) and Figure 8.5 (methane cation). For both the neutral molecule and cation, using a static field with modest intensity, i.e. producing 5%–20% ionization, the highest ionization rate is parallel to the four C–H bonds. These results suggest that before any structural relaxation, the relative ejection angle between the two electrons resulting from the first and second ionization should on average be equal to the angle between the C-H bonds (109.5°).

The TDCI-CAP calculation results for relaxed methane cation structures (Figure 8.1), i.e. the C_{2v}, C_{3v} and D_{2d} structures, are less straightforward. As shown in Figure 8.6, the highest

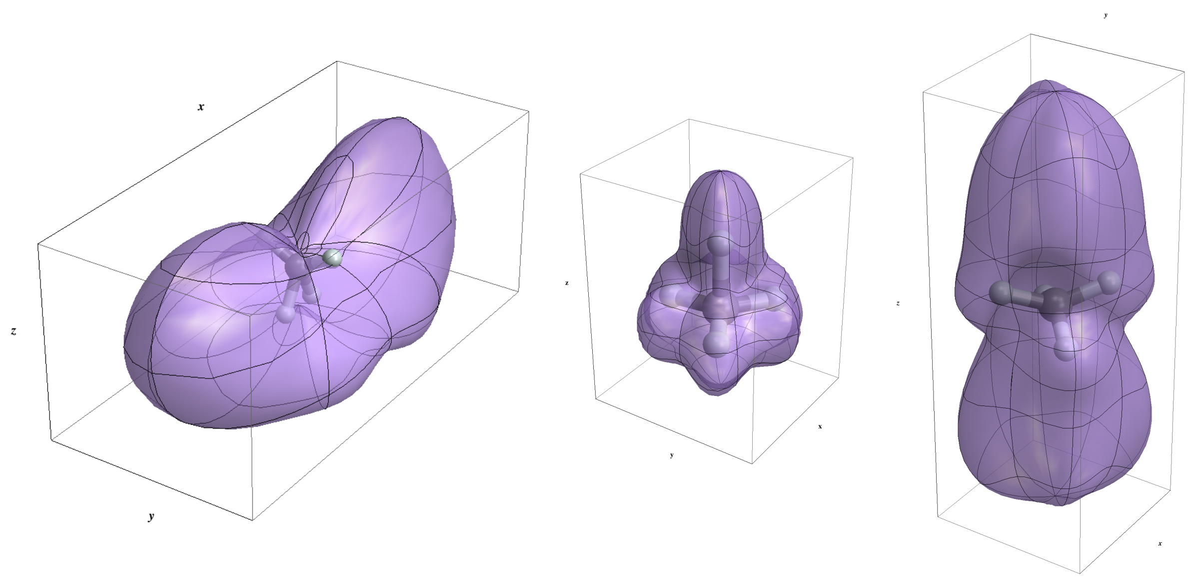

C_{2v} C_{3v} D_{2d}

Figure 8.6. Ionization dependence of methane cation with C_{2v}, C_{3v} and D_{2d} geometries.

ionization rate for a) C_{2v}, b) C_{3v} and c) D_{2d} structures is along the directions: a) nearly anti-parallel to the two C–H bonds that form the smaller bond angle (ca. 60°), b) parallel and anti-parallel to the C–H bonds but mostly parallel to the longer C–H bond, and c) along the shared bisector of the two larger H–C–H bond angles (ca. 140°), respectively. From these results, it is difficult to estimate the most probable relative ejection angle for two electrons from sequential double ionization while having some degree of structural relaxation between the first and second ionization.

8.4 Structural relaxation classification

Although the TDCI-CAP calculations were inconclusive concerning the most probable relative ejection angle for sequential double ionization if methane cation undergoes some structural relaxation, it is still important for understanding the angular streaking experiments to establish a rough time frame for such relaxation. We have used BOMD trajectory calculations to model the relaxation after ionization. The logistic regression model described previously was used to classify geometries along BOMD trajectories into the model structures (C_{2v}, C_{3v} and D_{2d}

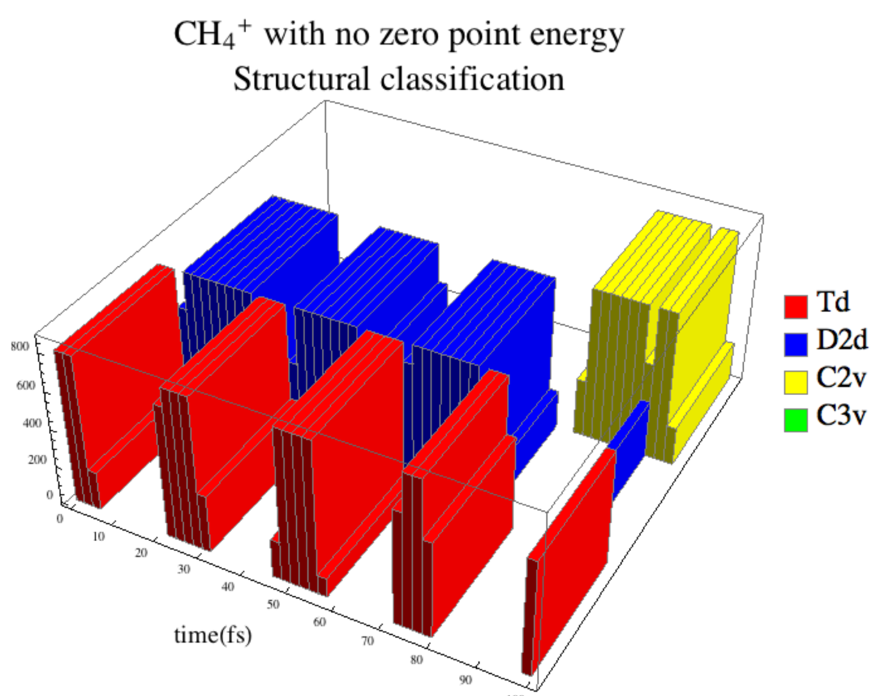

Figure 8.7. Histogram plot of structural classifications along an ideal trajectory without zero-point energy and thus entirely deterministic.

structures plus the starting geometry, T_d).

First, in order to test the validity of the classification scheme, we began with an ideal trajectory starting with the T_d geometry with no zero-point energy added. The trajectory is entirely deterministic and we can visualize every geometry manually. Key events along this trajectory is summarized as following: a) the two opposite H-C-H angles in the T_d structure increase resulting in a planar D_{4h} symmetry structure; b) this motion continue, inverting the structure to produce the mirror image of the original T_d structure; c) these oscillations persist for a few of cycles; d) some small perturbation breaks the oscillation and further distortion leads to a C_{2v} structure at the end of the simulation. All of these events can be traced back to the classifications made by our logistic regression model.

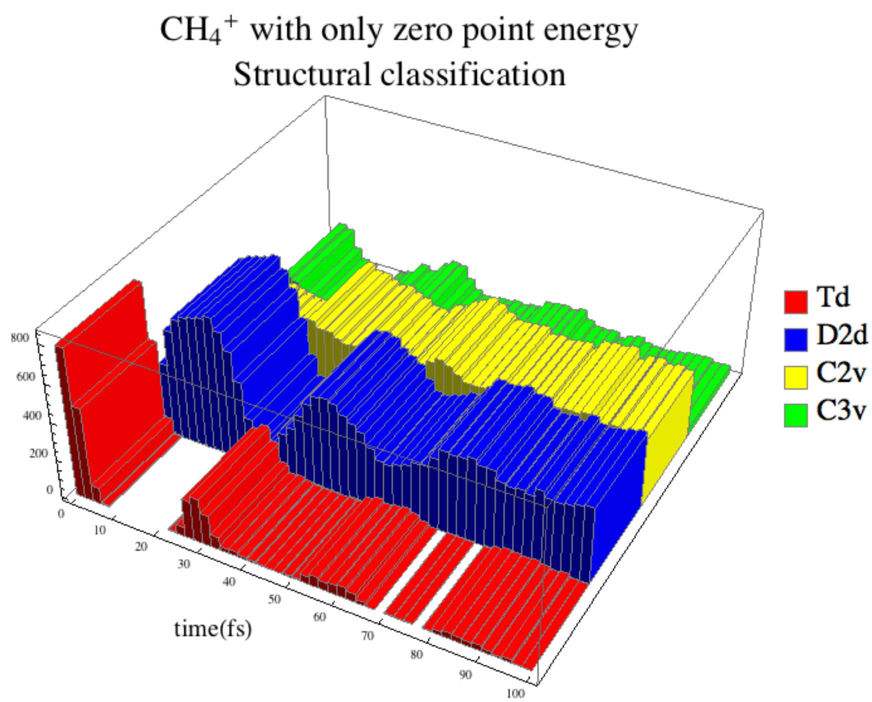

Figure 8.8. Histogram plot of structural classifications along an ideal trajectory without zero-point energy and thus entirely deterministic.

Having validated our classification procedure, we now apply it to a set of BOMD trajectories with zero-point energy distributed to vibrational modes thermally accessible to the methane cation after the vertical ionization from neutral molecule (according to micro-canonical distribution). It takes roughly 3 fs to deplete half the initial population (or 7 fs to deplete the entire initial population) of T_d structures and transition into mostly D_{2d} and some C_{2v} structures.

Afterwards there is a nearly equal distribution between D_{2d} and C_{2v} structures with almost no C_{3v} structures throughout the simulation time. Due to the limitations of BOMD method in a short time window such as the first 7 fs relaxation time frame, this time frame should best serve as a measurement of the upper limit to such relaxation time frame. Entirely similar conclusions regarding the initial relaxation time frame can be drawn from the simulation results with additional thermal energies (11 and 30 kcal/mol).

8.5 Summary

In this chapter, we simulated some key aspects of the two-electron angular streaking experiments for methane molecule in order to obtain a better understanding of the relative ejection angle of the two electrons from the sequential ionization. The TDCI-CAP calculations used a static field to obtain the angular dependence of ionization of methane and methane cation. A symmetry operation based procedure was used to treat the triple-degeneracy of methane cation. The ionization rate is the highest parallel to the C–H bond direction for T_d symmetry structure for both methane neutral and cation. The angular dependence of ionization is less clear for the model structures resulted from structural relaxations. Nonetheless, it is still most reasonable to expect these ionizations to align with the C–H bond direction except for the D_{2d} structure.

With a simple implementation of logistic regression model, one of the basic machine learning models, we have classified geometries along BOMD trajectory simulations of the relaxation process from starting T_d structure and find that it takes approximately 3 fs for having an appreciable amount of starting geometry to relax into a nearly equal distribution of C_{2v} and D_{2d} structures.

REFERENCES

(1) Basu, D.; Mazumder, S.; Shi, X.; Baydoun, H.; Niklas, J.; Poluektov, O.; Schlegel, H. B.; Verani, C. N. *Angew. Chem. Int. Ed. Engl.* **2015**, *54*, 2105.

(2) Basu, D.; Mazumder, S.; Niklas, J.; Baydoun, H.; Wanniarachchi, D.; Shi, X.; Staples, R. J.; Poluektov, O.; Schlegel, H. B.; Verani, C. N. *Chem. Sci.* **2016**, *7*, 3264.

(3) Basu, D.; Mazumder, S.; Shi, X.; Staples, R. J.; Schlegel, H. B.; Verani, C. N. *Angew. Chem.* **2015**, *127*, 7245.

(4) Lee, S. K.; Schlegel, H. B.; Li, W. *J. Phys. Chem. A* **2013**, *117*, 11202.

(5) Lee, S. K.; Suits, A. G.; Schlegel, H. B.; Li, W. *J. Phys. Chem. Lett.* **2012**, *3*, 2541.

(6) Shi, X.; Li, W.; Schlegel, H. B. *J. Chem. Phys.* **2016**, *145*, 084309.

(7) Shi, X.; Thapa, B.; Li, W.; Schlegel, H. B. *J. Phys. Chem. A* **2016**, *120*, 1120.

(8) Crosby, G. A. *Acc. Chem. Res.* **1975**, *8*, 231.

(9) Juris, A.; Balzani, V.; Barigelletti, F.; Campagna, S.; Belser, P.; Zelewsky, A. v. *Coord. Chem. Rev.* **1988**, *84*, 85.

(10) Kalyanasundaram, K. *Photochemistry of polypyridine and porphyrin complexes*; Academic Press: New York, 1992.

(11) Balzani, V.; Credi, A.; Venturi, M. *Coord. Chem. Rev.* **1998**, *171*, 3.

(12) Balzani, V.; Juris, A.; Venturi, M.; Campagna, S.; Serroni, S. *Chem. Rev.* **1996**, *96*, 759.

(13) Ford, P. C. In *Inorganic and Organometallic Photochemistry*; Wrighton, M. S., Ed.; American Chemical Society: Washington, DC, 1978; Vol. 168, p 73.

(14) Malouf, G.; Ford, P. C. *J. Am. Chem. Soc.* **1977**, *99*, 7213.

(15) Wagenknecht, P. S.; Ford, P. C. *Coord. Chem. Rev.* **2011**, *255*, 591.

(16) Endicott, J. F.; Solomon, E. I.; Lever, A. B. P. *Electronic Structure and Spectroscopy of Inorganic Compounds*, 1999; Vol. 2.

(17) Endicott, J. F.; Balzani, V. *Electron Transfer in Chemistry*, 2001; Vol. 1.

(18) Ferraudi, G. J. *Elements of Inorganic Photochemistry*, 1988.

(19) Horvath, O.; Stevenson, K. L. *Charge Transfer Photochemistry of Coordination Complexes*, 1993.

(20) Snir, O.; Weinstock, I. A.; Bakac, A. *Physical Inorganic Chemistry: Reactions, Processes, and Applications*, 2010.

(21) Hewitt, J. T.; Vallett, P. J.; Damrauer, N. H. *J. Phys. Chem. A* **2012**, *116*, 11536.

(22) Hupp, J. T.; Williams, R. T. *Acc. Chem. Res.* **2001**, *34*, 808.

(23) Xie, P.; Chen, Y. J.; Endicott, J. F.; Uddin, M. J.; Seneviratne, D.; McNamara, P. G. *Inorg. Chem.* **2003**, *42*, 5040.

(24) Xie, P.; Chen, Y. J.; Uddin, M. J.; Endicott, J. F. *J. Phys. Chem. A* **2005**, *109*, 4671.

(25) Chen, Y. J.; Xie, P.; Heeg, M. J.; Endicott, J. F. *Inorg. Chem.* **2006**, *45*, 6282.

(26) Chen, Y. J.; Endicott, J. F.; McNamarra, P. G. *J. Phys. Chem. A* **2007**, *111*, 6748.

(27) Allard, M. M.; Odongo, O. S.; Lee, M. M.; Chen, Y. J.; Endicott, J. F.; Schlegel, H. B. *Inorg. Chem.* **2010**, *49*, 6840.

(28) Lord, R. L.; Allard, M. M.; Thomas, R. A.; Odongo, O. S.; Schlegel, H. B.; Chen, Y. J.; Endicott, J. F. *Inorg. Chem.* **2013**, *52*, 1185.

(29) Parr, R. G.; Yang, W. *Density-functional theory of atoms and molecules*, 1989.

(30) Frisch, M. J.; Trucks, G. W.; Schlegel, H. B.; Scuseria, G. E.; Robb, M. A.; Cheeseman, J. R.; Scalmani, G.; Barone, V.; Mennucci, B.; Petersson, G. A.; Nakatsuji, H.; Caricato, M.; Li, X.; Hratchian, H. P.; Izmaylov, A. F.; Bloino, J.; Zheng, G.; Sonnenberg, J. L.; Hada, M.; Ehara, M.; Toyota, K.; Fukuda, R.; Hasegawa, J.; Ishida, M.; Nakajima, T.; Honda, Y.; Kitao, O.; Nakai, H.; Vreven, T.; Montgomery Jr., J. A.; Peralta, J. E.; Ogliaro, F.; Bearpark, M. J.; Heyd, J.; Brothers, E. N.; Kudin, K. N.; Staroverov, V. N.; Kobayashi, R.; Normand, J.; Raghavachari, K.; Rendell, A. P.; Burant, J. C.; Iyengar, S. S.; Tomasi, J.; Cossi, M.; Rega, N.; Millam, N. J.; Klene, M.; Knox, J. E.; Cross, J. B.; Bakken, V.; Adamo, C.; Jaramillo, J.; Gomperts, R.; Stratmann, R. E.; Yazyev, O.; Austin, A. J.; Cammi, R.; Pomelli, C.; Ochterski, J. W.; Martin, R. L.; Morokuma, K.; Zakrzewski, V. G.; Voth, G. A.; Salvador, P.; Dannenberg, J. J.; Dapprich, S.; Daniels, A. D.; Farkas, Ö.; Foresman, J. B.; Ortiz, J. V.; Cioslowski, J.; Fox, D. J.; H.35 ed.; Gaussian, Inc.: Wallingford, CT, USA: 2015.

(31) Becke, A. D. *J. Chem. Phys.* **1993**, *98*, 5648.

(32) Krishnan, R.; Binkley, J. S.; Seeger, R.; Pople, J. A. *J. Chem. Phys.* **1980**, *72*, 650.

(33) Perdew, J. P. *Phys. Rev. B* **1986**, *33*, 8822.

(34) Perdew, J. P.; Burke, K.; Wang, Y. *Phys. Rev.* **1996**, *54*, 16533.

(35) Andrae, D.; Haussermann, U.; Dolg, M.; Stoll, H.; Preuss, H. *Theor.Chim.Acta* **1990**, *77*, 123.

(36) Dunning, T. H.; Hay, P. J.; Schaefer, H. F. *Modern Theoretical Chemistry*, 1976; Vol. 3.

(37) Igelmann, G.; Stoll, H.; Preuss, H. *Mol. Phys.* **1988**, *65*, 1321.

(38) T. H. Dunning, J.; Hay, P. J. In *Modern Theoretical Chemistry*; H. F. Schaefer, I., Ed. New York, 1976; Vol. 3, p 1.

(39) Chang, J. P.; Fung, E. Y.; Curtis, J. C. *Inorg. Chem.* **1986**, *25*, 4233.

(40) Vydrov, O. A.; Heyd, J.; Krukau, A.; Scuseria, G. E. *J. Chem. Phys.* **2006**, *125*, 074106.

(41) Vydrov, O. A.; Scuseria, G. E.; Perdew, J. P. *J. Chem. Phys.* **2007**, *126*, 154109.

(42) Bauernschmitt, R.; Ahlrichs, R. *J. Chem. Phys.* **1996**, *104*, 9047.

(43) Schlegel, H. B.; McDouall, J. J.; Ögretir, C.; Csizmadia, I. G. *Computational Advances in Organic Chemistry*, 1991.

(44) Schlegel, H. B. *J. Comput. Chem.* **1982**, *3*, 214.

(45) Miertuš, S.; Scrocco, E.; Tomasi, J. *Chem. Phys.* **1981**, *55*, 117.

(46) Scalmani, G.; Frisch, M. J. *J. Chem. Phys.* **2010**, *132*, 114110.

(47) Scalmani, G.; Frisch, M. J.; Mennucci, B.; Tomasi, J.; Cammi, R.; Barone, V. *J. Chem. Phys.* **2006**, *124*, 9410.

(48) Tomasi, J.; Mennucci, B.; Cammi, R. *Chem. Rev.* **2005**, *105*, 2999.

(49) Petit, L.; Maldivi, P.; Adamo, C. *J. Chem. Theory Comput.* **2005**, *1*, 953.

(50) Runge, E.; Gross, E. K. U. *Phys. Rev. Lett.* **1984**, 52.

(51) Stratmann, R. E.; Scuseria, G. E.; Frisch, M. J. *J. Chem. Phys.* **1998**, *109*, 8218.

(52) Martin, R. L. *J. Chem. Phys.* **2003**, *118*, 4775.

(53) Dennington, R.; Keith, T.; Millam, J. M.; Semichem, Inc.: Shawnee Mission, KS, 2009; Vol. 5.

(54) Tsai, C. N.; Allard, M. M.; Lord, R. L.; Luo, D. W.; Chen, Y. J.; Schlegel, H. B.; Endicott, J. F. *Inorg. Chem.* **2011**, *50*, 11965.

(55) Isse, A. A.; Gennaro, A. *J. Phys. Chem. B* **2010**, *114*, 7894.

(56) Namazian, M.; Lin, C. Y.; Coote, M. L. *J. Chem. Theory Comput.* **2010**, *6*, 2721.

(57) IUPAC.

(58) Jakubikova, E.; Chen, W.; Dattelbaum, D. M.; Rein, F. N.; Rocha, R. C.; Martin, R. L.; Batista, E. R. *Inorg. Chem.* **2009**, *48*, 10720.

(59) Crosby, G. A. *Acc. Chem. Res.* **1975**, *8*, 231.

(60) Juris, A.; Balzani, V.; Barigelletti, F.; Compagna, S.; Belser, P. L.; von Zelewsky, A. *Coord. Chem. Rev.* **1988**, *84*, 85.

(61) J.A.Turner *Science* **2004**, *305*, 972.

(62) Lewis, N. S.; Nocera, D. G. In *Proc. Natl. Acad. Sci.* USA, 2006; Vol. 103, p 15729

(63) Connolly, P.; Espenson, J. H. *Inorg. Chem.* **1986**, *25*, 2684

(64) Razavet, M.; Artero, V.; Fontecave, M. *Inorg. Chem.* **2005**, *44*, 4786

(65) Xile, H.; Brunschwig, B. S.; Peters, J. C. *J. Am. Chem. Soc.* **2007**, *129*, 8988

(66) Bhattacharjee, A.; Andreiadis, E. S.; Kerlidou, M. C.; Fontecave, M.; Field, M. J.; Artero, V. *Chem. Eur. J.* **2013**, *19*, 15166

(67) Shi, S.; Daniels, L. M.; Espenson, J. H. *Inorg. Chem.* **1991**, *30*, 3407

(68) Weakley, T. J. R.; Marks, J.; Finke, R. G.; Crystallogr, A. *Sect. C* **1994**, *50*, 1690

(69) Bigi, J. P.; Hanna, T. E.; Harman, W. H.; Chang, A.; Chang, C. J. *Chem. Commun.* **2010**, *46*, 958

(70) Stubbert, B. D.; Peters, J. C.; Gray, H. B. *J. Am. Chem. Soc.* **2011**, *133*, 18070

(71) Sun, Y.; Bigi, J. P.; Piro, N. A.; Tang, M. L.; Long, J. R.; Chang, C. J. *J. Am. Chem. Soc.* **2011**, *133*, 9212

(72) Leung, C. F.; Chen, Y. Z.; Yu, H. Q.; Yiu, S. M.; Ko, C. C.; Lau, T. C. *Int. J. Hydrogen Energy* **2011**, *36*, 11640.

(73) Singh, W. M.; Baine, T.; Kudo, S.; Tian, S.; Ma, X. A. N.; Zhou, H.; DeYonker, N. J.; Pham, T. C.; Bollinger, J. C.; Baker, D. L.; Yan, B.; Webster, C. E.; Zhao, X. *Angew. Chem.* **2012**, *124*, 6043.

(74) King, A. E.; Surendranath, Y.; Piro, N. A.; Bigi, J. P.; Long, J. R.; Chang, C. J. *Chem. Sci.* **2013**, *4*, 1578

(75) Nippe, M.; Khnayzer, R. S.; Panetier, J. A.; Zee, D. Z.; Olaiya, B. S.; Head-Gordon, M.; Chang, C. J.; Castellano, F. N.; Long, J. R. *Chem. Sci.* **2013**, *4*, 3934

(76) Zhang, P.; Wang, M.; Gloaguen, F.; Chen, L.; Quentel, F.; Sun, L. *Chem. Commun.* **2013**, *49*, 9455

(77) Singh, W. M.; Mirmohades, M.; Jane, R. T.; White, T. A.; Hammarstrçm, L.; Thapper, A.; Lomoth, R.; Ott, S. *Chem. Commun.* **2013**, *49*, 8638.

(78) Tong, L.; Zong, R.; Thummel, R. P. *J. Am. Chem. Soc.* **2014**, *136*, 4881.

(79) Kawano, K.; Yamauchi, K.; Sakai, K. *Chem. Commun.* **2014**, *50*, 9872

(80) Call, A.; Codolà, Z.; Parés, F. A.-.; Lloret-Fillol, J. *Chem. Eur. J.* **2014**, *20*, 6171

(81) Dolg, M.; Wedig, H.; Preuss, H. *J. Chem. Phys.* **1987**, *86*, 866.

(82) Schaefer, A.; Huber, C.; Ahlrichs, R. *J. Chem. Phys.* **1994**, *100*, 5829.

(83) Seeger, R.; Pople, J. A. *J. Chem. Phys.* **1977**, *66*, 3045.

(84) Schlegel, H. B.; McDouall, J. J. In *Computational Advances in Organic Chemistry*; Ögretir, C., Csizmadia, I. G., Eds. Kluwer Academic, Amsterdam, The Netherlands, 1991.

(85) Artero, V.; Chavarot-Kerlidou, M.; Fontecave, M. *Angew. Chem. Int. Ed.* **2011**, *50*, 7238.

(86) Wang, M.; Chen, L.; Sun, L. *Energy Environ. Sci.* **2012**, *5*, 6763.

(87) Solis, B. H.; Hammes-Schiffer, S. *J. Am. Chem. Soc.* **2011**, *133*, 19036.

(88) Solis, B.; Yu, Y.; Hammes-Schiffer, S. *Inorg. Chem.* **2013**, *52*, 6994.

(89) Muckermann, J. T.; Fujita, E. *Chem. Commun.* **2011**, *47*, 12456.

(90) Solis, B. H.; Schiffer, S. H.-. *Inorg. Chem.* **2011**, *50*, 11252.

(91) Dempsey, J. L.; Winkler, J. R.; Gray, H. B. *J. Am. Chem. Soc.* **2010**, *132*, 16774.

(92) Basu, D.; Mazumder, S.; Shi, X.; Staples, R.; Schlegel, H. B.; Verani, C. N. *Angew. Chem. Int. Ed.* **2015**, *54*, 7139.

(93) Tyler, L. A.; Olmstead, M. M.; Mascharak, P. K. *Inorg. Chem.* **2001**, *40*, 5408

(94) Nesbitt, D. J.; Field, R. W. *J. Phys. Chem.* **1996**, *100*, 12735.

(95) Schulz, P. A.; Su, A. S.; Krajnovich, D. J.; Kwok, H. S.; Shen, Y. R.; Lee, Y. T. *Annu. Rev. Phys. Chem.* **1979**, *30*, 379.

(96) Abu-samha, M.; Madsen, L. B. *Phys. Rev. A: At., Mol., Opt. Phys.* **2011**, *84*, 023411.

(97) Shafir, D.; Soifer, H.; Vozzi, C.; Johnson, A. S.; Hartung, A.; Dube, Z.; Villeneuve, D. M.; Corkum, P. B.; Dudovich, N.; Staudte, A. *Phys. Rev. Lett.* **2013**, *111*, 023005.

(98) Krause, P.; Sonk, J. A.; Schlegel, H. B. *J. Chem. Phys.* **2014**, *140*, 174113.

(99) Krause, P.; Schlegel, H. B. *J. Phys. Chem. A* **2015**, *119*, 10212.

(100) Krause, P.; Schlegel, H. B. *J. Chem. Phys.* **2014**, *141*, 174104.

(101) Krause, P.; Schlegel, H. B. *J. Phys. Chem. Lett.* **2015**, *6*, 2140.

(102) Dunning, T. H. *J. Chem. Phys.* **1989**, *90*, 1007.

(103) Wilson, A. K.; Mourik, T. v.; Dunning, T. H. *Comput. Theor. Chem.* **1996**, *388*, 339.

(104) Schlegel, H. B. *J. Chem. Theory Comput.* **2013**, *9*, 3293.

(105) Bakken, V.; Millam, J. M.; Bernhard Schlegel, H. *J. Chem. Phys.* **1999**, *111*, 8773.

(106) Wu, H.; Rahman, M.; Wang, J.; Louderaj, U.; Hase, W. L.; Zhuang, Y. *J. Chem. Phys.* **2010**, *133*, 074101.

(107) Bunker, D. L. *J. Chem. Phys.* **1973**, *59*, 4621.

(108) Kubel, M.; Siemering, R.; Burger, C.; Kling, N. G.; Li, H.; Alnaser, A. S.; Bergues, B.; Zherebtsov, S.; Azzeer, A. M.; Ben-Itzhak, I.; Moshammer, R.; de Vivie-Riedle, R.; Kling, M. F. *Phys. Rev. Lett.* **2016**, *116*, 193001.

(109) Okino, T.; Watanabe, A.; Xu, H.; Yamanouchi, K. *Phys. Chem. Chem. Phys.* **2012**, *14*, 10640.

(110) Ibrahim, H.; Wales, B.; Beaulieu, S.; Schmidt, B. E.; Thire, N. *Nat. Commun.* **2014**, *5*, 4422.

(111) Jiang, Y. H.; Rudenko, A.; Herrwerth, O.; Foucar, L.; Kurka, M.; Kuhnel, K. U.; Lezius, M.; Kling, M. F.; van Tilborg, J.; Belkacem, A.; Ueda, K.; Dusterer, S.; Treusch, R.; Schroter, C. D.; Moshammer, R.; Ullrich, J. *Phys. Rev. Lett.* **2010**, *105*, 263002.

(112) Xu, H.; Okino, T.; Yamanouchi, K. *Chem. Phys. Lett.* **2009**, *469*, 255.

(113) Osipov, T.; Cocke, C. L.; Prior, M. H.; Landers, A.; Weber, T.; Jagutzki, O.; Schmidt, L.; Schmidt-Bocking, H.; Dorner, R. *Phys. Rev. Lett.* **2003**, *90*, 233002.

(114) Xu, H.; Marceau, C.; Nakai, K.; Okino, T.; Chin, S. L.; Yamanouchi, K. *J. Chem. Phys.* **2010**, *133*, 071103.

(115) Xu, H.; Okino, T.; Kudou, T.; Yamanouchi, K.; Roither, S.; Kitzler, M.; Baltuska, A.; Chin, S. L. *J. Phys. Chem. A* **2012**, *116*, 2686.

(116) Itakura, R.; Liu, P.; Furukawa, Y.; Okino, T.; Yamanouchi, K.; Nakano, H. *J. Chem. Phys.* **2007**, *127*, 104306.

(117) Hoshina, K.; Furukawa, Y.; Okino, T.; Yamanouchi, K. *J. Chem. Phys.* **2008**, *129*, 104302.

(118) Townsend, D.; Lahankar, S. A.; Lee, S. K.; Chambreau, S. D.; Suits, A. G.; Zhang, X.; Rheinecker, J.; Harding, L. B.; Bowman, J. M. *Science* **2004**, *306*, 1158.

(119) Suits, A. G. *Acc. Chem. Res.* **2008**, *41*, 873.

(120) Bowman, J. M.; Shepler, B. C. *Annu. Rev. Phys. Chem.* **2011**, *62*, 531.

(121) Lahankar, S. A.; Chambreau, S. D.; Townsend, D.; Suits, F.; Farnum, J.; Zhang, X.; Bowman, J. M.; Suits, A. G. *J. Chem. Phys.* **2006**, *125*, 44303.

(122) Lee, T. J.; Schaefer, H. F. *J. Chem. Phys.* **1986**, *85*, 3437.

(123) Lindh, R.; Rice, J. E.; Lee, T. J. *J. Chem. Phys.* **1991**, *94*, 8008.

(124) Lindh, R.; Roos, B. O.; Kraemer, W. P. *Chem. Phys. Lett.* **1987**, *139*, 407−416.

(125) Curtiss, L. A.; Pople, J. A. *J. Chem. Phys.* **1988**, *88*, 7405.

(126) Crofton, M. W.; Jagod, M. F.; Rehfuss, B. D.; Oka, T. *J. Chem. Phys.* **1989**, *91*, 5139.

(127) Gabrys, C. M.; D.Uy; Jagod, M.-F.; Oka, T. *J. Phys. Chem.* **1995**, *99*, 15611.

(128) Knoll, L.; Vager, Z.; Marx, D. *Phys. Rev. A: At. Mol. Opt. Phys.* **2003**, *67*.

(129) Vager, Z.; Zajfman, D.; Graber, T.; Kanter, E. P. *Phys. Rev. Lett.* **1993**, *71*, 4319.

(130) Psciuk, B. T.; Benderskii, V. A.; Schlegel, H. B. *Theor. Chem. Acc.* **2007**, *118*, 75.

(131) Sharma, A. R.; Wu, J.; Braams, B. J.; Carter, S.; Schneider, R.; Shepler, B.; Bowman, J. M. *J. Chem. Phys.* **2006**, *125*, 224306.

(132) Fortenberry, R. C.; Huang, X.; Crawford, T. D.; Lee, T. J. *J. Phys. Chem. A* **2014**, *118*, 7034.

(133) Marx, D.; Parrinello, M. *Science* **1996**, *271*, 179.

(134) Tse, J. S.; Klug, D. D.; Laasonen, K. *Phys. Rev. Lett.* **1995**, *74*, 876.

(135) Zhao, Y.; Truhlar, D. G. *Theor. Chem. Acc.* **2007**, *120*, 215.

(136) Frisch, M. J.; Pople, J. A.; Binkley, J. S. *J. Chem. Phys.* **1984**, *80*, 3265.

(137) Llorente, J. M. G.; Pollak, E. *Annu. Rev. Phys. Chem.* **1992**, *43*, 91.

(138) Baer, T.; Hase, W. L. *Unimolecular reaction dynamics: theory and experiments*; Oxford University Press, 1996.

(139) Lee, S. K.; Li, W.; Bernhard Schlegel, H. *Chem. Phys. Lett.* **2012**, *536*, 14.

(140) Thapa, B.; Schlegel, H. B. *J. Phys. Chem. A* **2014**, *118*, 10067.

(141) Thapa, B.; Schlegel, H. B. *Chem. Phys. Lett.* **2014**, *610-611*, 219.

(142) Cortes, C.; Vapnik, V. *Mach. Learn.* **1995**, *20*, 273.

(143) Bishop, C. M. *Pattern Recognition and Machine Learning*; Springer, 2006.

ABSTRACT

COMPUTATIONAL STUDY OF TRANSITION METAL COMPLEXES FOR SOLAR ENERGY CONVERSION AND MOLECULAR INTERACTION WITH STRONG LASER FIELDS

by

XUETAO SHI

May 2018

Advisor: Dr. H. Bernhard Schlegel

Major: Chemistry (Physical)

Degree: Doctor of Philosophy

There are two topics in this dissertation: ground state and excited state modeling of a few series of transition metal complexes that facilitate solar energy conversion, and Born-Oppenheimer Molecular Dynamics (BOMD) simulations of molecular cations interacting with intense mid-infrared laser light.

In Chapter 2 and 3, a few series of transition metal complexes that facilitate solar energy conversion are studied computationally. Metal-to-ligand charge-transfer (MLCT) excited states of several (ruthenium) (monodentate aromatic ligand, MDA) chromophore complexes are modeled by using time-dependent density function theory (TD-DFT). The calculated MLCT states correlate closely with the heretofore unknown emission properties that were observed experimentally. The hydrogen evolution mechanisms of three new series of cobalt based water splitting catalysts are modeled by Density Functional Theory (DFT). The three series include: 1) a

family of cobalt complexes with pentadentate pyridine-rich ligands, 2) a family of three heteroaxial cobalt oxime catalysts, namely [Co^{III}(prdioxH)(^{4tBu}py)(Cl)]PF_6, [Co^{III}(prdioxH)(^{4Pyr}py)(Cl)]PF_6, and [Co^{III}(prdioxH)(^{4Bz}py)(Cl)]PF_6, 3) a pentadentate oxime that has ligand incorporated water upon metal coordination and is water soluble. These calculations provide reasonable interpretations of the experimental observations.

In Chapter 4, 5 and 6, mode selective fragmentation of $ClCHO^+$ and circular migration of hydrogen in protonated acetylene with intense mid-IR laser pulses are simulated by BOMD trajectory calculations. The ionization rate of ClCHO in the molecular plane has been calculated by time-dependent configuration interaction with a complex absorbing potential (TDCI-CAP), and is nearly twice as large as perpendicular to the plane, suggesting a degree of planar alignment can be obtained experimentally for $ClCHO^+$, starting from neutral molecules. The BOMD simulations demonstrate circularly polarized light with the electric field in the plane of the molecule deposits more energy and yields larger branching ratios for higher energy fragmentation channels than linearly polarized light with the same maximum field strength. The trajectories with different pairs of the dual laser pulses give very different branching ratios. The difference in branching ratios is even more pronounced when one of the two pulses started one quarter of the total duration earlier than the other vs. the other way around for the same pulse pair. In protonated acetylene, hydrogen migration around the C2 core occurs by interchange between the Y shaped classical structure and the bridged, T-shaped non-classical structure of the cation, which is 4 kcal/mol lower in energy. The linearly and circularly polarized pulses transfer similar amounts of energy and total angular momentum to $C_2H_3^+$. There is an appreciable amount of angular displacement of the three hydrogens relative to the C2 core for circularly polarized light, but only an insignificant amount for linearly polarized light. This suggests a propeller-like motion of the three hydrogens is induced only by the circularly polarized light.

In Chapter 7, an inherent problem in BOMD is explained and mostly circumvented by using ADMP method. Since BOMD is based on the Born-Oppenheimer approximation, the wavefunction of the system is converged at each time step to calculate the force for integrating the classical equations of motion. This resulted in an artifact manifested for a few trajectories as anomalously large charge oscillations on an H atom ($H^+/H^\bullet/H^-$) when it was well-separated (beyond ca. 3 Å) from the rest of the molecule, thus absorbing an anomalously large amount of energy. ADMP method, an alternative to BOMD method, propagates the density matrix using extended Lagrangian dynamics. Our ADMP calculations in intense laser fields show that the accuracy is similar to BOMD while the charge oscillation problem is eliminated naturally because the electronic wavefunction is propagated rather than converged at each step.

In Chapter 8, in order to interpret the experimental results of two-electron angular streaking for methane molecule, TDCI calculations and BOMD trajectory calculations are carried out with the additional help from a logistic regression machine learning algorithm to analyze geometric changes. The ionization angular dependence of various stable and meta-stable structures of methane cation, as well as neutral methane, is calculated by our TDCI-CAP approach. The ionization is mostly along the C–H bond direction for the neutral methane and monocation in the tetrahedral geometry, while the directions of ionization for other geometries are less straightforward. The relaxation time needed for neutral methane geometry (tetrahedron shape) to collapse into D_{2d} and C_{2v} structures on the cation potential energy surface is estimated to be 3 fs (half of the initial population converted) by classifying geometries along BOMD trajectories with a machine learning algorithm.

AUTOBIOGRAPHICAL STATEMENT

XUETAO SHI

Born October 17, 1988, Xining, Qinghai, P. R. China

Education

Nanjing University, Nanjing, China, B. Sc. (Chemistry), 2011

Wayne State University, Michigan, USA, Ph.D. (Physical Chemistry), 2018

Publications

1. Tsai, C. N.; Tian, Y.-H.; Shi, X.; Lord, R. L.; Schlegel, H. B.; Chen, Y. J.; Endicott, J. F., Experimental and DFT characterization of metal-to-ligand charge-transfer excited states of (rutheniumammine)(monodentate aromatic ligand) chromophores. *Inorg. Chem.* **2013**, *52*, 9774-9790.

2. Basu, D.; Mazumder, S.; Shi, X.; Baydoun, H.; Niklas, J.; Poluektov, O.; Schlegel, H. B.; Verani, C. N., Ligand transformations and efficient proton/water reduction with cobalt catalysts based on pentadentate pyridine-rich environments. *Angew. Chem. Int. Ed.* **2015**, *54*, 2105-10.

3. Basu, D.; Mazumder, S.; Shi, X.; Staples, R. J.; Schlegel, H. B.; Verani, C. N., Distinct proton and water reduction behavior with a cobalt(III) electrocatalyst based on pentadentate oximes. *Angew. Chem. Int. Ed.* **2015**, *54*, 7139-43.

4. Basu, D.; Mazumder, S.; Niklas, J.; Baydoun, H.; Wanniarachchi, D.; Shi, X.; Staples, R. J.; Poluektov, O.; Schlegel, H. B.; Verani, C. N., Evaluation of the coordination preferences and catalytic pathways of heteroaxial cobalt oximes towards hydrogen generation. *Chem. Sci.* **2016**, *7*, 3264-3278.

5. Shi, X.; Li, W.; Schlegel, H. B., Computational simulations of hydrogen circular migration in protonated acetylene induced by circularly polarized light. *J. Chem. Phys.* **2016**, *145*, 084309.

6. Shi, X.; Thapa, B.; Li, W.; Schlegel, H. B., Controlling chemical reactions by short, intense mid-infrared laser pulses: comparison of linear and circularly polarized light in simulations of ClCHO+ fragmentation. *J. Phys. Chem. A* **2016**, *120*, 1120-1126.

7. Peters, W. K.; Couch, D. E.; Mignolet, B.; Shi, X.; Nguyen, Q. L.; Fortenberry, R. C.; Schlegel, H. B.; Remacle, F.; Kapteyn, H. C.; Murnane, M. M.; Li, W., Ultrafast 25-fs relaxation in highly excited states of methyl azide mediated by strong nonadiabatic coupling. *PNAS* **2017**, 114 (52), E11072-E11081.